TEMPERATURE PREDICTION MODEL FOR HORIZONTAL WELL WITH

MULTIPLE FRACTURES IN SHALE RESERVOIR

A Thesis

by

NOZOMU YOSHIDA

Submitted to the Office of Graduate Studies of
Texas A&M University
in partial fulfillment of the requirements for the degree of

MASTER OF SCIENCE

Approved by:

Chair of Committee,	Alfred Daniel Hill
Committee Members,	Ding Zhu
	Yuefeng Sun
Head of Department,	Alfred Daniel Hill

May 2013

Major Subject: Petroleum Engineering

ABSTRACT

Fracture diagnostics is a key technology for well performance prediction of a horizontal well in a shale reservoir. The combination of multiple fracture diagnostic techniques gives reliable results, and temperature data has potential to provide more reliability on the results. In this work, we show an application of a temperature prediction model for a horizontal well with multiple hydraulic fractures in order to investigate the possibility of evaluating reservoir and hydraulic fracture parameters using temperature data. The model consists of wellbore model and reservoir model.

The wellbore model was formulated based on mass, momentum and energy balance. The reservoir flow model was solved by a numerical reservoir simulation, and the reservoir thermal model was formulated by transient energy balance equation considering viscous dissipation heating and temperature variation caused by fluid expansion besides heat conduction and convection. The reservoir flow and reservoir thermal model were coupled with the wellbore model to predict temperature distribution in a horizontal well considering boundary conditions at the contact of reservoir and wellbore. In the reservoir system, primary hydraulic fractures which are transverse to the horizontal well were modeled with thin grid cells explicitly, and the hydraulically-induced fracture network around the horizontal well was modeled as higher permeable zone to unstimulated matrix zone. The reservoir grids between two primary fractures were logarithmically spaced in order to capture transient flow behavior. We applied the model to synthetic examples: horizontal well with identical five fractures and with different five fractures. The results show two fundamental mechanisms: heat conduction between formation and wellbore fluid at non-perforated zone, and wellbore fluid mixing effect at each fracture. The synthetic example with identical fractures shows that fracture locations affect wellbore temperature distribution because of fluid mixing effect between reservoir inflow and wellbore fluid. And also, the synthetic example with different fractures shows that the fracture heterogeneity causes different magnitude of temperature

change due to inflow variation per fracture. In addition, the model was applied to synthetic examples without network fracture region in order to find the effects by the network. It reveals that under constant rate condition, network fracture masks large temperature change due to small pressure change at the contact between fracture and formation, and that under constant BHP condition, network fracture augments temperature change with the increase of flow rate in wellbore and inflow rate from reservoir.

Sensitivity studies were performed on temperature distribution to identify influential parameters out of the reservoir and hydraulic fracture parameters including reservoir porosity, reservoir permeability, fracture half-length, fracture height, fracture permeability, fracture porosity, fracture network parameters, and fracture interference between multiple clusters. In this work, in order to find contributions by a target fracture, temperature change sensitivity is evaluated. Single fracture case reveals that fracture permeability, network fracture parameters and fracture geometries are primary influential parameters on temperature change at the fracture location. And also, multiple fractures case shows that temperature change is augmented with the increase of fracture geometry and is decreased with the increase of fracture permeability. These results show the possibility of using temperature to determine these sensitive parameters, and also the quantified parameter sensitivities provide better understandings of the temperature behavior of horizontal well with multiple fractures.

DEDICATION

To my parents, Noritsugu and Kaoru, my brother, Jun and my sister, Misaki, and my grandmother, Tsuyuko for their supports and encouragements.

ACKNOWLEDGEMENTS

NOMENCLATURE

b_j	=	reciprocal value of formation volume factor of phase j (=o, w or g)
B_j	=	formation volume factor of phase j (=o, w or g)
C_p	=	heat capacity
C_h	=	heat transfer coefficient
D	=	depth, ft
$\mathbf{e}$	=	total energy flux
e	=	total energy
f	=	friction factor, dimensionless
g	=	gravity acceleration, ft/day^2
H	=	enthalpy
k	=	absolute permeability, md
k_{rj}	=	relative permeability of phase j
K	=	thermal conductivity
K_{JT}	=	Joule Thomson coefficient
K_{Tt}	=	total thermal conductivity
N_p	=	number of existing phase, dimensionless
N_{Re}	=	Reynolds number, dimensionless
$N_{Re,w}$	=	wall Reynolds number, dimensionless
p_j	=	pressure of phase j, psia
$\tilde{q}_j$	=	molar production or injection rate of phase j per unit volume, mol/ft^3/day
Q	=	heat transfer between wellbore and reservoir
r_w	=	well radius, ft
r_{eff}	=	effective wellbore radius, ft
R	=	well radius for wellbore model, ft

R_s	=	solution gas/oil ratio, scf/STB
S_j	=	saturation of phase j, dimensionless
t	=	time, day
T	=	temperature, F
u_j	=	flow velocity of phase j for reservoir model, ft/day
v	=	flow velocity for wellbore model, ft/day
U	=	internal energy
U_T	=	overall heat transfer coefficient
y_{ij}	=	mole fraction of component i in phase j

Greek

β	=	thermal expansion coefficient, 1/°F
γ	=	pipe open ratio
ϕ	=	porosity, dimensionless
ρ	=	density, lb/ft^3
θ	=	wellbore inclination, rad
μ	=	viscosity, cp
$\boldsymbol{\tau}$	=	shear stress tensor
τ	=	shear stress
$\boldsymbol{\pi}$	=	total molecular stress tensor

Subscripts

c	=	casing
EPA	=	enhanced permeability area
f	=	fracture
F	=	fracture
f, n	=	fracture network

f, p	=	primary fracture
f, s	=	secondary fracture
i	=	component
I	=	arriving/inflow property
j	=	phase
M	=	matrix
s	=	solid or rock
w	=	wellbore property

TABLE OF CONTENTS

LIST OF FIGURES

LIST OF TABLES

1. INTRODUCTION

1.1   BACKGROUND

Interests in developing unconventional oil and gas reservoirs have grown dramatically in last decades because of its potentially huge amount as an energy resource. Shale reservoir is one kind of the unconventional reservoirs, and it is defined as organic-rich, fine-grained sedimentary rocks containing a minimum of 0.5 wt% total organic carbon (Cardott, 2006). Because shale reservoirs have extremely low permeability, for the economical production, large contact area is required between well and reservoir, and then usually hydraulic fracturing technique is used. Especially, Horizontal wells with multiple hydraulic fractures have an important role in shale gas reservoirs, and the designs of hydraulic fracturing treatment are developed recently.

Originally, the fracturing treatment in shale reservoir was the same with conventional hydraulic fracturing treatment in order to create a large planar fracture with high viscosity injection fluid. However, the case of Barnett shale reservoir in which waterfracs or light-sand low viscosity fracturing fluid was used presented considerable improvement both in the production performance and in the economics. The use of waterfracs leads to very complex fracture network around wellbore with multiple orientations, which is calibrated by fracture mapping technologies. For the performance prediction of a horizontal well with complex fracture network, stimulated reservoir volume is an important parameter. In order to predict well performance by quantifying the stimulated reservoir volume, shale reservoir modeling with complex facture network is conducted by several researchers with analytical, semianalytical and numerical simulation.

With the development of the hydraulic fracturing treatment design and the shale reservoir modeling for well performance prediction, recent advances in fracture diagnostic technologies provide a wealth of information on created hydraulic fractures and hydraulic fracturing process. There are three main groups of commercially available fracture-diagnostic techniques: direct far-field fracture diagnostics (e.g. tiltmeter

mapping, microseismic mapping), direct near-wellbore fracture diagnostics (e.g. production logging, radioactive tracer) and indirect fracture diagnostics (e.g. pressure transient analysis, production data analysis). Each technique has advantages and disadvantages, and then a combination of multiple fracture diagnostic technologies can provide more reliable evaluation of hydraulic fracture performance eliminating much of the uncertainty associated with non-uniqueness.

Temperature data along the wellbore is generally measured during a conventional production logging and, recently, by advanced technology such as distributed temperature sensors, more accurate temperature data is measured in real time. Comparing to the pressure data, temperature data is more reliable because it is measured accurately no matter what the wellbore flow conditions. In addition, because its distinct specifications of geothermal temperature gradient and Joule Thomson effect, the temperature data is used for the well performance diagnostics for vertical, slanted and horizontal wells in the versatile applications such as detection of water or gas entry, casing leaks and quantitative reservoir parameter estimation such as permeability and wellbore damage radius. And also, the distributed temperature sensing technology is applied to qualitative diagnostics of the hydraulic fracturing treatment in vertical and horizontal wells. However, quantitative diagnostics of the wells with multiple hydraulic fractures are still challenging for the created hydraulic factures and fracture network and the effectiveness of the fracturing process.

1.2   LITERATURE REVIEW
1.2.1   DOWNHOLE DATA ACQUISITION
The determination of downhole flow profiles and more importantly what is actually occurring within the nearby reservoir are an important part of reservoir management over the life of a well (Brady et al., 1998). Hill (1990) presented the importance of production logging techniques for well and reservoir diagnosis and provided an overview of several tools of production logging such as temperature log, radioactive

tracer log, spinner flowmeter log, and noise log. He mainly focused on the vertical well and slanted well, and production logging techniques for horizontal well are presented by several literatures.

Brady et al. (1998) used pulse neutron capture logs and time lapse log while drilling for the quantification of the inflow profile along a horizontal well, and gas inflow profile was quantified by the combination of estimated production profile and temperature log. Carnegie et al. (1998) presented the importance to integrate as much as possible the data from all the different sensors such as a full bore directional spinner and flow visualization tools run on a horizontal well production log through the field cases, and also showed that an information on well trajectory is generally a vital component of the data. Chace et al. (2000) presented new multiple sensor production logging tools designed for horizontal and highly deviated multiphase producers, and it successfully determined multiphase holdups, velocity profiling, fluid entry points and production inflow profiling for multiphase flow. Kelder et al. (2005) successfully applied the tool presented by Chace et al. (2000) to short radius horizontal wells with modification of the tool to coiled-tubing-conveyed production logging tool. Mustafa et al. (2005) presented a new tool with the miniaturization of the spinners and the mounting of the sensors along a vertical diameter of the wellbore, and its ability to measure the gas velocity and its relatively short length in comparison with conventional tools enable users to better understand their production flow regimes. Zeybek et al. (2005) and Mukerji et al. (2006) applied the same type of compact new tool presented by Mustafa et al. (2005) to the identification of super-permeable zones or conductive fractures and the direct assessment of their flow contributions; determination of water salinity variations to define injection water entry along the wellbore; the evaluation of production pressure loss; and the diagnostics of the downhole flow regime. Fitz et al. (2006) also applied the array spinner and array holdup measurements in Chayvo field, and they provided interpretations that are more likely to represent actual downhole conditions than can be achieved from conventional production logging tools. With these evolutions of the direct measurement technology, Sask et al. (2007) presented a Video logging technology, and

it can provide insights on complex production problems or discrepancies of interpretation given by different conventional logging tools. Recently, Heddleston (2009) presented an application of the production logging for an unconventional shale gas horizontal well, and it concerned that the amount of the well flow rate through completions should be checked if it is high enough for quality results from the logging. Mccluskey (2012) also presented an application of production logging in Marcellus Shale.

Temperature log is one of the production logging technologies, and it is used in many applications such as location of water or gas entries, detection of casing leaks and fluid movement behind casing and qualitative identification of injection or production zones (Hill, 1990). For vertical well, geothermal temperature profile gives the trend of temperature log, and Joule Thomson effects caused by reservoir inflow and outflow and heat transfer between wellbore fluid and casing lead to anomalies of the temperature profile from the temperature trend. However, for horizontal wells, temperature variation caused by geothermal temperature is almost zero, and then temperature variation mainly depends on the Joule Thomson effects and heat transfer between wellbore and formation. In reality, the horizontal well is not perfectly horizontal. Therefore, the temperature log of a horizontal well is strongly affected by well trajectory and completion design.

Recently, for the real time downhole temperature monitoring, fiber optic distributed temperature sensing technology (DTS) has been used in industry. This technology has an advantage that it enables us to observe a real time temperature profile along a wellbore comparing to conventional temperature log which can only provide us with a snapshot of the temperature profile during the tool placed in the well.

Since the first fiber optic pressure and temperature sensors were installed for Shell in the Sleen field in 1993 (Kragas et al., 2001), this technology is used in the several fields for versatile applications. In several fields, these sensors were installed for accurate measurement of the temperature profile along the horizontal section and to identify a possible increase of temperature due to the water entry (Brown et al., 2000; Carnahan et al., 1999; Foucault et al., 2004). Fryer et al. (2005) applied it for the real

4

time temperature measurement in multi-layered reservoir to identify zone production rate changes. Johnson et al. (2006) and Huebsch et al. (2008) presented a successful application for gas flow rate profiling using the measured DTS data of vertical wells. For horizontal wells also, by considering subtle temperature change in wellbore and reservoir, the DTS was successfully applied to inflow rate profiling (Li, 2010; Li and Zhu, 2010; Yoshioka, 2007; Yoshioka et al., 2009). Julian (2007) presented the application for the detection of downhole leaking in vertical wells. Glasbergen et al. (2009) presented the real time quantification of fluid distribution during a matrix treatment using DTS data for better understanding of the stimulation. Sierra et al. (2008) and Huckabee (2009) applied the DTS data to diagnose the fracture stimulation and evaluate well performance. For shale reservoirs, Gonzalez and Chokshi (2012) presented the DTS application, and recently the DTS technology is used with distributed acoustic sensing techniques for fracture diagnostics in shale reservoirs (Molenaar et al., 2012).

1.2.2 TEMPERATURE MODELING AND INTERPRETATION

One of the earliest works on temperature modeling was proposed by Ramey (1962). Ramey's model predicts temperature distribution for production or injection vertical wells of single phase incompressible liquid or ideal gas flow. The model assumes steady state heat transfer inside a wellbore and transient radial conduction from a reservoir. The semi-analytical temperature solution was formulated as a function of time and depth.

Satter (1965) modified Ramey's model for steam injection in vertical wells with consideration of condensation effects. Sagar et al. (1991) extended Ramey's model to inclined wells and two phase flow considering Joule-Thomson effects caused by pressure change along the wellbore. Hasan and Kabir (1991) presented a rigorous heat transfer model given by the heat conduction in the formation to predict transient formation temperature behavior for all times, and Hasan and Kabir (1994) further developed Ramey's model using rigorous transient formation temperature equation.

5

They introduced heat convection and radiation effects in the wellbore steady state temperature model, and it showed the importance of the convective heat transfer.

Because the models presented above are steady state model, in order to study transient thermal behavior, new temperature models were developed. One of the earliest works on wellbore transient temperature modeling was developed by Miller (1980) which considers the changes in energy of the reservoir fluid while flowing through the wellbore due to both heating of the fluid in the wellbore and heat loss out of the wellbore. In this model, mass balance, momentum balance, energy balance and an equation of state are combined to solve wellbore pressure implicitly, and then the density, velocity and energy are calculated for new time step. Kabir et al. (1996) presented wellbore/reservoir simulator for gas single phase flow, and it was extended to oil single phase flow (Hasan et al., 1997) and two-phase flow (Hasan et al., 1998). Izgec et al. (2007) used a semi-analytical heat transfer model by replacing the finite-differential energy equation used in Kabir et al. model for efficient computation. In these models, the analytical formation temperature model presented by Hasan and Kabir (1991) was used, and the temperature of the reservoir inflow was assumed to be the same with the formation temperature.

Because of the geothermal temperature gradient, these temperature models for vertical or slanted wells were dominated by heat transfer between wellbore fluids and formation. Then, some smaller thermal effects such as fluid thermal expansion and viscous dissipation heating were ignored comparing to the geothermal effect due to the elevation change. For horizontal wells, the situation is different from the case of vertical or slanted wells because the geothermal temperature change is very small or zero sometimes. Many field cases (Brady et al., 1998; Chace et al., 2000; Foucault et al., 2004; Heddleston, 2009) showed temperature variations along the horizontal wells, and in order to explain this phenomenon, the subtle thermal effects in reservoirs and inside wellbore need to be considered in a temperature model for horizontal wells. In addition, the advancement of the DTS technology enables us to measure the temperature in the wellbore with the accuracy and resolution of approximately 0.1 ℃ (Ouyang and

Belanger, 2006) (but they depends on the measurement acquisition time (Julian, 2007)). These were the major motivation for the development of the temperature models in horizontal wells.

The early work proposed by Maubeuge et al. (1994) included these subtle thermal effects of thermal expansion and viscous dissipation heating in their transient reservoir temperature model. However, their wellbore model was not explained clearly in the paper. Ouyang and Belanger (2006) presented wellbore temperature prediction model for vertical, slanted and horizontal wells considering the Joule Thomson effects in the application of DTS data. Yoshioka et al. (2005b) presented a temperature model in horizontal wells considering heat convection, conduction, fluid expansion and gravity effects with the effect of reservoir inflow along the horizontal well. They used the model in the application for the temperature change in the deviated horizontal well, detection of water or gas entry in the horizontal direction and the vertical direction (water coning) by coupling the wellbore model with the analytical or numerical solutions of inflow temperature distribution along the horizontal well (Dawkrajai et al., 2006; Yoshioka et al., 2005a; Yoshioka et al., 2007). All the above models were formulated under steady state condition. For the transient thermal behavior, Sui et al. (2008a) and Duru and Horne (2010) developed the transient temperature model for wellbore with the analytical or semianalytical representation of reservoir temperature model. In addition, Sui (2009) presented that the transient wellbore model can be reduced to steady state condition if the measurement time is long enough such as days. Based on this observation, Li and Zhu (2010) presented transient temperature model with transient numerical reservoir model with steady state wellbore model presented by Yoshioka et al. This model successfully captured the transient behavior of temperature along the horizontal well for the water coning case and water injection case from the adjacent horizontal well (Li et al., 2011). Muradov and Davies (2011) presented a transient analytical temperature model in a horizontal well with single phase liquid production, but they mainly focused on the temperature change caused by transient behavior of reservoir inflow and did not consider the temperature variation along the horizontal well.

In terms of coupling of the reservoir and wellbore model, there are some discussions on the temperature at the contact between wellbore and reservoir which is called arriving temperature. As mentioned, at the zone without reservoir inflow, the arriving temperature is assumed to be geothermal temperature. On the other hand, at the zone with reservoir inflow, it is assumed to be geothermal temperature with the Joule Thomson effect, and the drawdown pressure was used for the calculation of the Joule Thomson effect. Pinzon et al. (2007) claimed that the usage of drawdown pressure overestimates the temperature change, and it was consistent with the calculation method presented by Brady et al. (1998) who used the half of the drawdown pressure. In the work by Yoshioka et al. (2007), they used analytical solution given by the reservoir thermal model for the arriving temperature, and Sui et al. (2008a) and Muradov and Davies (2011) also used the analytical solution at the sand face. Li and Zhu (2010) took the analogous approach with the work done by Peaceman (1983) for pressure, and solved simplified 1D ordinary differential equation of reservoir thermal model in the reservoir grid which contains wellbore to compute the arriving temperature.

These temperature prediction models are used for the quantitative interpretation of downhole conditions using measured temperature data and estimation temperature. This interpretation is conducted through the minimization of error between the estimated temperature distribution and the measured temperature distribution along a wellbore. In this context, the temperature prediction model is called forward model, and the back estimation of the input parameters of forward model through the minimization of the observation-prediction error is called inverse modeling. Yoshioka et al. (2009), Sui et al. (2008b) and Sui et al. (2010) used a gradient based method, Levenberg-Marquardt method, in their inversion process, and they successfully quantitatively estimate permeability distribution along horizontal wells and the multiple properties of the multilayer reservoir such as reservoir permeability, damage permeability and damage radius. Li and Zhu (2010) used a stochastic method, Markov Chain Monte Carlo method, for the estimation of inflow profiles along horizontal wells. Tan et al. (2012) also used the Markov Chain Monte Carlo for the diagnosis of acid placement with their

temperature model which includes the effect by chemical reaction. Recently, Hoang et al. (2012) and Tabatabaei and Zhu (2012) presented the application to an injection fluid profile for the hydraulic fracturing in the vertical well with limited entry and in the horizontal well with multiple stage fracturing.

1.2.3 SHALE RESERVOIR MODELING

Shale reservoir modeling

Because of its extremely low permeability, shale reservoir requires hydraulic fracturing treatment for commercial production. Originally, stimulation treatment of shale reservoir was the same with conventional hydraulic fracturing treatment in order to create a large bi-wing plane fracture with the wellbore at the center of the wings using high viscosity fracturing fluid. Fisher et al. (2005), however, presented the case of Barnett shale reservoir in which they used waterfracs or light-sand fracturing treatment and it considerably improved both production performance and economics in the reservoir. Because of several factors, including the presence of natural fractures, the fracture treatment created very complex fracture networks around the wellbore with multiple orientations, and they calibrated the network structure using fracture mapping technologies such as surface/downhole tiltmapping and microseismic mapping (Fisher et al., 2004; Fisher et al., 2005). In order to predict a performance of wells with the fracture network, several parameters were examined to correlate well performance with the parameter (Fisher et al., 2004; Fisher et al., 2005; Maxwell et al., 2009). Mayerhofer et al. (2010) used stimulated reservoir volume as a correlation parameter for well performance and considered the relationship using measured stimulated reservoir volume in Barnett shale generated from microseismic and production data. The relationship is general and it does not provide any quantification of the actual effective fracture network structure for the gas production, and then they used a numerical reservoir simulator with history matching for the quantification of the effective network

structure. They described the fracture network as a discrete set of high permeability fractures (Cipolla et al., 2010a; Mayerhofer et al., 2006) .

In numerical shale reservoir modeling, several methods were presented and they are grouped into two types: discrete fracture network model and multiple-porosity model. In discrete fracture network model, as aforementioned, the fracture network is expressed as a discrete set of high permeability fractures. Cipolla et al. (2010a) presented a numerical reservoir simulation model using a detailed numerical grid that rigorously represents the network fractures, hydraulic fractures, matrix blocks and unstimulated areas. This model can rigorously express transient behaviors of shale reservoirs, but it requires huge amount of computational efforts. On the other hand, in the multiple-porosity model, the reservoir is represented by several overlapping continua. Originally, a dual porosity approach, one of the multiple porosity models, was proposed by Warren and Root (1963) and Kazemi et al. (1976) in order to express the fluid flow in naturally fractured reservoirs. In the dual porosity model, each reservoir grid contains matrix and fractures, and the flow and heat transfer between the matrix and fractures is controlled by shape factor. Several shape factors of the fluid flow and heat transfer were proposed by several researchers (Coats, 1989; Heel et al., 2008; Kazemi et al., 1976; Warren and Root, 1963). Zhang et al. (2009) applied the dual porosity model for shale gas reservoir with the explicit expression of the primary hydraulic fractures as fine grid cells perpendicular to a horizontal well and fracture network in the vicinity of the hydraulic fractures was characterized by the shape factor and permeability of the fractures. They concluded the treatment provides an accurate response. In addition, Knauss et al. (1985) presented a multiple interacting continua method as a generalization of the dual porosity model. In this method, each grid contains fracture and nested sub-grids of matrix blocks, and fluid flow and heat flow from the fractures into the matrix blocks or from the matrix blocks into the fractures are modeled by means of one dimensional string of nested grid blocks (Moridis et al., 2010). Moridis et al. (2010) applied the multiple interacting continua method for the analysis of flow in tight gas and shale gas reservoir. They defined the subdomain of the fractured shale reservoir as native fractures, primary fractures

(hydraulic fractures), secondary fractures (induced network fractures) and radial fractures which are induced by changes in the geomechanical status of the rock in the vicinity of the wellbore, and the method was used to express the flow between fractures and matrix in these sub domains. These methods can reduce computational efforts comparing to the discrete fracture network model, but typically the analytical solution used in these models cannot capture the very long transient behavior in the matrix blocks exhibited by shale gas reservoirs (Cipolla et al., 2010a). In addition, Yin et al. (2011) used an enhanced permeability area to approximate the enhancement effect by the network fractures as higher permeable matrix zone in the vicinity of the fractures. In this method, the hydraulic fractures were expressed as the higher permeable grids, and the enhanced permeability area exists along the fracture grid to consider the stimulated reservoir volume.

For analytical shale reservoir modeling, several models were also proposed in order to understand the performance of horizontal wells with multiple fractures. Medeiros et al. (2008) used the dual porosity model in the vicinity of the hydraulic fractures with transient semianalytical pressure solutions presented by Medeiros et al. (2010b) for evaluation of productivity and drainage area of a fractured horizontal well. Medeiros et al. (2010a) also presented an application of the semianalytical model with dual porosity region for the production data analysis in shale reservoirs. Ozkan et al. (2011) used an analytical solution given by a tri-linear model with the dual porosity model for the network structure, and they confirmed the importance of the existence of network fractures for well performance and the trade-off between decrease of fracture spacing and decrease of incremental gain for each additional fracture. Meyer et al. (2010) used a simple analytical solution derived on tri-linear flow with single porosity model, and demonstrated the importance of the multiple transverse fracture optimization through the history matching work about the Marcellus and Eagle Ford shale reservoirs.

Ever since the success of the Barnett shale program, operators are inclined to pump similar large volume waterfracs treatments with little or no proppant in their respective shale plays, but such large volume treatments in other shale plays may not be an

11

optimized solution for the specific shale attributes (Ramurthy et al., 2011). So, it is important to understand the characteristics of each shale reservoir, and to consider treatment designs in response to the characteristics. Cipolla et al. (2010b) considered this fracture-treatment-design issue focusing on fracture conductivity requirements for complex fractures and, through reservoir simulation study, they concluded that the network fracture conductivity required to maximize production is proportional to the square root of fracture spacing, indicating that increasing fracture complexity reduces conductivity requirement. Also, they presented as guideline for the treatment design in terms of the formation permeability range that when the permeability is on the order of 0.0001 md, it is beneficial to generate large fracture networks using low viscosity fluids (waterfracs), when the permeability approaches 0.01 md, fracture design is tailored to generate small networks with improved conductivity using medium viscosity (hybrid fracture treatment), and when the permeability is on the order of 1 md, fracture conductivity is optimized using high viscosity fluids (cross-linked fluids). Ramurthy et al. (2011) conducted several tests such as core and log analysis, unpropped-fracture-conductivity test and a diagnostic fracture injection test for several shale reservoirs, and they concluded that the Barnett type waterfracs is not the correct completion method for all shale plays. Especially, Brinell hardness test showed the Barnett shale is completely different from the Eagle Ford, Greenhorn and the Haynesville shale because they are much softer than the Barnett shale (Ramurthy et al., 2011). For the Eagle Ford shale, Stegent et al. (2010) presented that the hybrid fracture treatment outperformed waterfracs treatment in the area of high liquid production, and Ramurthy et al. (2011) mentioned the higher conductivity is need because the potential for embedment is also high.

Completion design in shale reservoirs

Multistage hydraulic fracturing becomes the key technology to complete horizontal wells in shale reservoirs. According to several field cases such as the Haynesville shale

and Eagle Ford shale, more than 10 stages are completed in order to maximize the exposure to formations for the economic production from shale reservoirs (Bazan et al., 2010; Pope et al., 2012; Thompson et al., 2011). Bazan et al. (2010) presented one example of the multistage hydraulic fracturing treatment for the Eagle Ford shale. The Eagle Ford horizontal well was completed with a ten stage proppant fracture stimulation using slickwater, liner gel and 40/80 lightweight ceramic proppant in a 4,000 ft lateral. Composite bridge plugs were used for stage isolation. Each 400 ft stage was perforated with four, two-foot clusters spaced 75 ft apart. In each stage, the first and last perforation intervals were shot at six shots per foot and the middle two intervals were shot at twelve shots per foot. The average treating rate and surface treating pressure were approximately 50 barrels per minute and 8,900 psi, respectively. The proppant volume placed per stage was approximately 250,000 lbm with 11,300 barrels of water used per stage (Bazan et al., 2010).

As presented in the above example, in order optimize completion design, it is required to consider several parameters such as number of stages, number of clusters per stage, number of perforations, stage interval, cluster spacing, selection of proppant and injection fluid, injection fluid volume and cementing design (Ketter et al., 2008; Pope et al., 2012; Thompson et al., 2011). Additionally, because the created fractures/clusters change the stress anisotropy in the reservoir (Cheng, 2012), new treatment procedure to enhance near-wellbore and far-field fracture network complexity was presented considering the existence and magnitude of principal stress anisotropy and designing the optimum spacing between fractures with optimum fracture treatment parameters (East et al., 2011).

Fracture diagnostic techniques
Recent advances in fracture diagnostic technologies provide a wealth of information on created hydraulic fractures and hydraulic fracturing process. There are three main groups of commercially available fracture-diagnostic techniques: direct far-field fracture

diagnostics, direct near-wellbore fracture diagnostics and indirect fracture diagnostics (Cipolla and Wright, 2002).

Direct far-field fracture diagnostics are conducted from offset wellbores or surface during fracture treatments, and generally provide information about far-field fracture growth. A main limitation of these techniques is that they map the total extent of hydraulic fracture growth but provide no information about the effective propped-fracture length or conductivity (Cipolla and Wright, 2002). This method comprises two fracture mapping tools, microseismic mapping and surface and downhole tiltmeter.

Comparing to the far-field fracture diagnostics, direct near-wellbore fracture diagnostics provide information of the treatment wellbore, and its major application is the identification of the fluid/proppant entry or production from each zone in multiple zone completion. A major limitation of this method is that these measurement can provide only what happens to the fracture at the wellbore, and it does not provide any information about the fracture when it is father than about 1 to 2 ft from the wellbore (Cipolla and Wright, 2002). Radioactive tracer and production logging techniques are grouped into this method, and recently, the application of the DTS and distributed acoustic sensing technology is examined for the fracture diagnostics in both of quantitative and qualitative analysis (Hoang et al., 2012; Huckabee, 2009; Molenaar et al., 2012; Sierra et al., 2008; Tabatabaei and Zhu, 2012).

Indirect fracture diagnostics are the most widely used because the data required for the analyses are more readily available. They can provide estimates of the fracture dimensions, effective fracture length, and fracture conductivity based on indirect measurement, such as the pressure response during the propped fracture treatment or the pressure and flow rate during production (Cipolla and Wright, 2002). A major limitation of this method is that the solutions are generally non-unique, but Cipolla et al. (2009) presented a combination of multiple fracture diagnostic technologies with fracture modeling, production data analysis, pressure transient analysis and numerical reservoir modeling, and they concluded that the combination can provide a more reliable

evaluation of hydraulic fracture performance eliminating much of the uncertainty associated with non-unique solutions.

1.3   OBJECTIVES AND APPROACH

Our ultimate goal of this work is to develop a temperature interpretation model for qualitative fracture diagnostics using downhole temperature data. In this thesis, we focus on development of a temperature prediction model for a horizontal well with multiple hydraulic fractures. The model should have the capabilities of taking into account the complex completion designs used in shale reservoirs such as multiple stage stimulation, complex well trajectory and fracture network induced or reactivated by hydraulic fracturing treatment for field application.

In order to express complex downhole situation in shale reservoirs, we choose an approach of numerical simulation for temperature prediction in reservoirs and wellbores. For the prediction of transient, multiphase flow and temperature behavior in horizontal wells, the coupled wellbore-reservoir flow/thermal model developed by Li (2010) was used.

For the expression of induced or reactive complex fracture networks around the created hydraulic factures, we took the same approach presented by Yin et al. (2011). This is one of the single porosity models with the simple approximation of the enhancement effect by network fractures. In this approach, the created hydraulic fractures are explicitly expressed as the fine, high permeable planar grids perpendicular to a horizontal well, and the complex fracture network system is expressed by the high permeable matrix zones taking into account the enhancement by the complex fracture network for the fluid flow in the reservoir.

2 TEMPERATURE INTERPRETATION MODEL

2.1 INTRODUCTION

In this section, a temperature prediction model is established to simulate pressure and temperature behavior along a horizontal well. The model consists of a reservoir model and a wellbore model.

The reservoir model is a transient multiphase 3D model and includes a reservoir flow model and a reservoir thermal model. The reservoir flow model is formulated by the mass balance and Darcy's law to solve the pressure and the saturation distribution of the entire reservoir using the finite difference method. The reservoir thermal model is formulated by transient energy balance equation taking into account various small temperature changes in the reservoir using the finite volume method.

The wellbore model is a steady state multiphase 1D model and also includes the flow part and thermal part. The wellbore flow model is formulated by a mass balance equation and a momentum balance equation to solve the fluid velocity and pressure distribution along the horizontal well. The wellbore thermal model is formulated by energy balance equation to solve the temperature distribution. At each time step, the wellbore fluid velocity, pressure and temperature distributions are updated using the reservoir pressure, temperature and flow rate into the wellbore.

The reservoir and wellbore models described above are coupled together considering the conditions at the contact of them. By coupling these models, the transient pressure, the temperature and the inflow rate distributions is estimated along the horizontal well with an appropriate initial condition and boundary conditions. In the following section, at first the reservoir model and wellbore model are described and the coupled model is described.

2.2 RESERVOIR MODEL

In this section, the transient multiphase 3D reservoir flow model and thermal model is formulated by considering mass, momentum and energy balance equations.

2.2.1 RESERVOIR FLOW MODEL

Consider an arbitrary volume, V, of the porous medium bounded by a surface, A. If there is no dispersion or diffusion, the mass balance on component i in the control volume is expressed as (Tanaka, 2010)

$$\left\{ \begin{array}{c} \text{Rate of change} \\ \text{in amount of} \\ \text{component } i \text{ in } V \end{array} \right\} = \left\{ \begin{array}{c} \text{Net rate of inflow} \\ \text{of component } i \\ \text{into } V \text{ due to} \\ \text{convection} \end{array} \right\} + \left\{ \begin{array}{c} \text{Net rate of inflow} \\ \text{due to sink/source} \\ \text{flow } q \end{array} \right\}$$

.... (2.1)

The total accumulation in the control volume is described as

$$\left\{ \begin{array}{c} \text{Rate of change} \\ \text{in amount of} \\ \text{component } i \text{ in } V \end{array} \right\} = \frac{d}{dt} \phi \sum_{j=1}^{N_p} y_{ij} \rho_j S_j A \Delta x, \quad \text{.......................................} (2.2)$$

where ϕ is porosity, N_p is the number of existing phase, y_{ij} is the mole fraction of component i in phase j, ρ_j and S_j are the molar density and saturation of phase j, respectively.

At any differential element of area, the convective molar flux (moles per unit area / unit time) of component i in the phase j is expressed as

$$\left\{ \begin{array}{c} \text{Molar flux of} \\ \text{component } i \\ \text{in phase } j \end{array} \right\} = y_{ij} \rho_j \mathbf{u}_j. \quad \text{...} (2.3)$$

where $\mathbf{u}_j$ is Darcy flow velocity vector of phase j. Here we assume that the flux vector is normal to the surface, A, and then the net rate of inflow of component i by convection is given by

$$\left\{ \begin{array}{c} \text{Net rate of inflow} \\ \text{of component } i \\ \text{into } V \text{ due to} \\ \text{convection} \end{array} \right\} = -\sum_{j=1}^{N_p} y_{ij} \rho_j \mathbf{u}_j A. \quad \text{...} (2.4)$$

If there is fluid injection or production from a well, the mass change caused by injection/production should be taken into account for the mass balance. Let $\tilde{q}$ be a sink/source fluid mole per unit time and unit volume, the net rate of inflow due to the sink/source flow is described as

$$\left\{ \begin{array}{c} \text{Net rate of inflow} \\ \text{due to sink/source} \\ \text{flow } q \end{array} \right\} = \sum_{j=1}^{N_p} y_{ij}\tilde{q}_j A\Delta x \quad \dots\dots\dots\dots\dots\dots\dots (2.5)$$

where $\tilde{q} < 0$ for production and $\tilde{q} > 0$ for injection.

By substituting Eq. 2.2 through Eq. 2.5 into Eq. 2.1, an integral material balance for component i is expressed as

$$-\sum_{j=1}^{N_p} y_{ij}\rho_j \mathbf{u}_j A + \sum_{j=1}^{N_p} y_{ij}\tilde{q}_j A\Delta x = \frac{d}{dt}\phi\sum_{j=1}^{N_p} y_{ij}\rho_j S_j A\Delta x. \quad \dots\dots\dots (2.6)$$

This is the mole-rate balance of component i in the control volume V. If we assume that the phase velocity vector is constant at each cellblock surface, and since the integral of accumulation and convection becomes zero everywhere, each equation can be divided by the control volume V. Hence, the material balance equation for multi-component, multiphase flow is expressed in the form

$$-\nabla \cdot \sum_{j=1}^{N_p} y_{ij}\rho_j \mathbf{u}_j + \sum_{j=1}^{N_p} y_{ij}\tilde{q}_j = \frac{\partial}{\partial t}\phi\sum_{j=1}^{N_p} y_{ij}\rho_j S_j. \quad \dots\dots\dots\dots\dots (2.7)$$

For each phase, this equation is

$$\frac{\partial}{\partial t}\left(\phi y_{ij}\rho_j S_j\right) = -\nabla \cdot \left(y_{ij}\rho_j \mathbf{u}_j\right) + y_{ij}\tilde{q}_j. \quad \dots\dots\dots\dots\dots (2.8)$$

In this work, the reservoir flow model is assumed to be the black-oil model. This model consists of three fluid components (oil, water and gas) at standard conditions and they are distributed in three distinct phases (oil, water and gas). While oil and water are immiscible, gas may exist as free gas or solution gas (Ertekin et al., 2001). The final form of the mass balance equation is

$$\sum_{j=1}^{N_p}\left(\frac{\partial}{\partial t}\left(\phi R_{ij}b_j S_j\right) + \nabla \cdot \left(R_{ij}b_j \mathbf{u}_j\right) - q_j\right) = 0, \quad \dots\dots\dots\dots\dots (2.9)$$

where $b_j = 1/B_j$, B_j is a formation volume factor of phase j, q_j is the volumetric flow rate at standard conditions per unit reservoir volume and R_{ij} is the solubility of the component i in phase j defined as

$$R_{ij} = \frac{V_{ij}}{V_{jj}}, \quad \text{...}(2.10)$$

for the black-oil model, this is to be

$$R_{ij} = \begin{cases} 1 & i = j \\ R_s & i = \text{gas and } j = \text{oil}, \\ 0 & \text{otherwise} \end{cases} \quad \text{...}(2.11)$$

where R_s is the solution-gas ratio.

Darcy's law gives the flow velocity in the porous media for phase j, and it is given by

$$\mathbf{u}_j = -\frac{k_{rj}\mathbf{k}}{\mu_j}\left(\nabla p_j - \rho_j g \nabla D\right), \quad \text{...}(2.12)$$

where $\mathbf{k}$ is the permeability tensor, and k_{rj}, μ_j, ρ_j and p_j are relative permeability, viscosity, density and pressure of phase j, respectively. Therefore, using Eq. 2.9, 2.10 and 2.11, pressure and saturation in the reservoir are solved numerically for multiphase flow.

In this work, a commercial numerical simulation (ECLIPSE) is used to solve the pressure and the saturation distribution in the reservoir. Also, the gas phase is assumed to exist only as free gas and there is no solution gas ($R_s = 0$).

2.2.2   RESERVOIR THERMAL MODEL

In this work, the reservoir thermal model developed by Li (2010) is used directly. For an arbitrary volume V in a reservoir, the energy conservation equation is expressed as (Lake, 2010)

$$\begin{Bmatrix} \text{Accumulation} \\ \text{rate of energy} \\ \text{in } V \end{Bmatrix} = \begin{Bmatrix} \text{Net rate of} \\ \text{energy transport} \\ \text{into } V \end{Bmatrix} + \begin{Bmatrix} \text{Rate of energy} \\ \text{energy production} \\ \text{in } V \end{Bmatrix}.$$

$$\text{..}(2.13)$$

By neglecting the kinetic energy change, the energy accumulation in the control volume V is expressed as

$$\begin{Bmatrix} \text{Energy} \\ \text{accumulation} \\ \text{in } V \end{Bmatrix} = \left[\phi \sum_{j=1}^{N_p} \rho_j S_j (U_j + gD) + (1 - \phi)\rho_s U_s \right]_t^{t+dt} V, \quad \text{....}(2.14)$$

where the subscript j is denotes the fluid phase, s is the solid rock, U is the internal

energy, D is the depth. The energy transport term consists of the heat convection and the heat conduction expressed as

$$\begin{Bmatrix} \text{Convection of} \\ \text{energy transport} \\ \text{into } V \end{Bmatrix} = \sum_{j=1}^{N_p} \rho_j \mathbf{u}_j (H_j + gD) A, \quad \text{.................................} (2.15)$$

and

$$\begin{Bmatrix} \text{Conduction of} \\ \text{energy transport} \\ \text{into } V \end{Bmatrix} = (-K_{Tt} \nabla T) A \quad \text{.....................................} (2.16)$$

where H is the enthalpy of fluid, K_{Tt} is the total heat conductivity, A is the surface area of the control volume V.

When there is fluid injection or production from a well, a heat transfer between the reservoir and the wellbore is taken into account for the energy balance. Let $\dot{Q}$ be the heat transfer term per unit time and per unit area to express the energy production or injection in the control volume V which is expressed as

$$\dot{Q} = -K_{Tt} \left. \frac{\partial T}{\partial r} \right|_{r=r_w} + \sum_{j=1}^{N_p} \rho_j \mathbf{u}_j C_{p,j} \cdot (T_I - T_w) \quad \text{.....................................} (2.17)$$

where the first term denotes the heat conduction and the second term denotes the heat convection between the wellbore and the formation, and $C_{p,j}$ is the heat capacity of the phase j, T_I is the reservoir temperature at the contact between the reservoir and wellbore and T_w is the wellbore flowing temperature.

Therefore, the energy balance equation on the control volume V without energy production is formulated by substituting the Eq. 2.14 through 2.16 into Eq. 2.13 with zero energy production. Hence, the energy balance is expressed as

$$-\frac{d}{dt} \left[\phi \sum_{j=1}^{N_p} \rho_j S_j (U_j + gD) + (1 - \phi) \rho_s U_s \right]$$

$$= \nabla \cdot \left[\sum_{j=1}^{N_p} \rho_j \mathbf{u}_j (H_j + gD) \right] - \nabla \cdot [K_{Tl} \nabla T]. \quad \text{...........} (2.18)$$

Considering the definition of the enthalpy, thermal expansion coefficient and internal energy, they are given by

$$dH = C_p dT + \frac{1}{\rho}(1 - \beta T)dp \text{..} (2.19)$$

$$\beta = -\frac{1}{\rho}\left(\frac{\partial p}{\partial T}\right)_p = \frac{1}{V}\left(\frac{\partial p}{\partial T}\right)_p, \quad \text{...} (2\text{-}20)$$

and

$$U = H - \frac{p}{\rho}. \quad \text{...} (2.21)$$

Also, we assume that for the formation rock

$$dU_s \approx C_{p,s}dT. \quad \text{...} (2.22)$$

Hence, substituting the Eq. 2.19 through 2.22 into the Eq. 2.18, the energy balance equation is expressed in terms of the reservoir temperature as

$$-\left[\sum_{j=1}^{N_p}(\phi\rho_j S_j C_{p,j}) + (1-\phi)\rho_s C_{p,s}\right]\frac{\partial T}{\partial t} + \sum_{j=1}^{N_p}\left(\phi S_j \beta_j T \frac{\partial p_j}{\partial t}\right)$$

$$= \sum_{j=1}^{N_p}\rho_j \mathbf{u}_j \cdot C_{p,j}\nabla T - \nabla \cdot (K_{Tt}\nabla T) + \sum_{j=1}^{N_p}\mathbf{u}_j \cdot \nabla p_j \quad \text{..............} (2.23)$$

$$-\sum_{j=1}^{N_p}\beta_j T(\mathbf{u}_j \cdot \nabla p_j) + \sum_{j=1}^{N_p}\rho_j \mathbf{u}_j \cdot \nabla(gD)$$

where, in the left hand side, the first term is the accumulation term and the second term is a thermal expansion term related to pressure change with respect to time, and in the right hand side, the first term is the convection term, the second term is the conduction term, the third term is the viscous dissipation heating, the fourth term is the thermal expansion due to the pressure change with respect to space and the last term is the potential energy term.

2.3   WELLBORE MODEL

In this work, the model developed by Yoshioka (2007) is used directly for wellbore model. In this section, the steady state, multiphase and 1D wellbore flow model and thermal model is formulated by considering the mass, momentum and energy balance equations.

2.3.1 WELLBORE FLOW MODEL

Fig. 2.1 shows a differential volume element of a wellbore and it has the reservoir fluid flow which comes into the wellbore through its surface. The fluid velocity in the wellbore and the reservoir inflow velocity are expressed as

$$\mathbf{v} = \begin{pmatrix} v_x \\ v_r \\ v_\varphi \end{pmatrix} = \begin{cases} \begin{pmatrix} v \\ 0 \\ 0 \end{pmatrix} \; in\,wellbore \\ \begin{pmatrix} 0 \\ v_I \\ 0 \end{pmatrix} \; at\,well\,wall\,(r=R) \end{cases} , \quad \dots\dots\dots\dots\dots\dots\dots\dots\dots\dots (2.24)$$

where $\mathbf{v}$ is the velocity vector and the subscript I denotes the inflow properties to the wellbore. In this work, it is assumed that the fluid velocity in the wellbore has only one component in the axial direction (x-direction), and at the contact between the wellbore and the reservoir ($r=R$) the fluid velocity has only one component in the radial direction (r-direction), which means there is no slip at wall of the wellbore. In the following derivation, the axial velocity is expressed by v and the radial velocity is expressed by v_I.
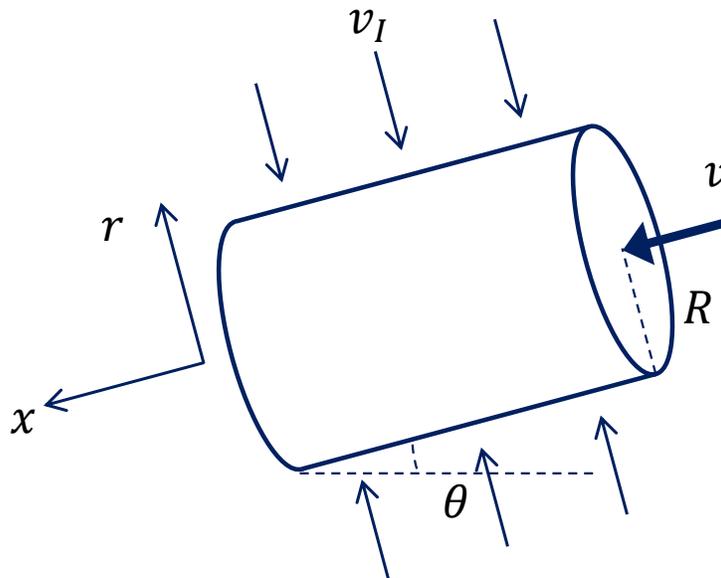
Fig. 2.1 Differential volume element of a wellbore

In order to consider different types of completion such as openhole or perforated liner, a pipe open ratio parameter is introduced which is defined as

$$\gamma = \frac{\text{Open area of Pipe}}{\text{Surface area of Pipe}} \quad \dots\dots\dots\dots\dots\dots\dots\dots\dots\dots\dots\dots\dots\dots\dots\dots (2.25)$$

Fig. 2.2 illustrates a cross section of a wellbore along the axial direction. As it is shown, the reservoir inflow comes into wellbore through the open area. Thus, the open area for the convection from reservoir is expressed as $2\pi R \gamma \Delta x$ when the length of the differential element is Δx.
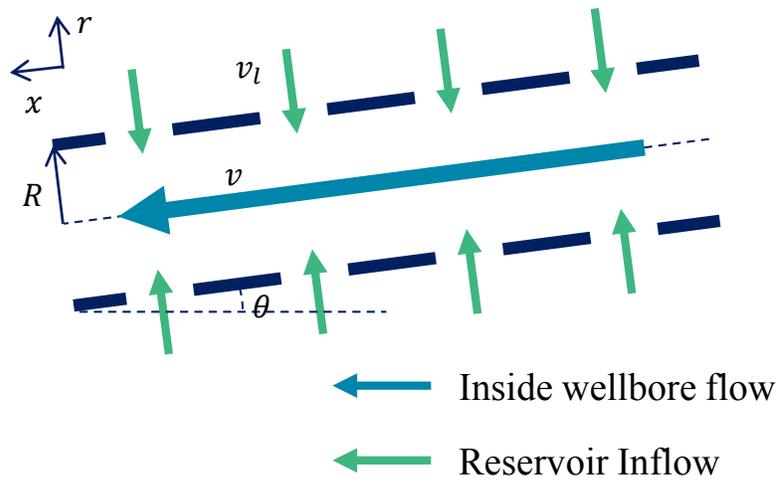
Fig. 2.2 Schematic of cross section of the wellbore

In the following part, at first we derive the conservation equations for single phase flow and it is extended to multiphase flow.

Mass balance

Over a differential volume element of a wellbore, which has an arbitrary volume of V, a mass balance equation is expressed as (Yoshioka, 2007)

23

$$\left\{\begin{array}{c}\text{Rate of}\\\text{increase}\\\text{of mass in V}\end{array}\right\}=\left\{\begin{array}{c}\text{Rate of}\\\text{mass}\\\text{into V}\end{array}\right\}-\left\{\begin{array}{c}\text{Rate of}\\\text{mass}\\\text{out from V}\end{array}\right\}. \quad \text{...........................} (2.26)$$

The rate of increase of mass in the differential volume element is expressed as

$$\left\{\begin{array}{c}\text{Rate of}\\\text{increase}\\\text{of mass in V}\end{array}\right\}=\pi R^2\Delta x\frac{\partial \rho}{\partial t}, \quad \text{..} (2.27)$$

where ρ denotes the density of the fluid inside wellbore. The rates of mass in and out of the differential volume are given as

$$\left\{\begin{array}{c}\text{Rate of}\\\text{mass}\\\text{into V}\end{array}\right\}=2\pi R\gamma\Delta x(\rho v_r)_{r=R}+\pi R^2(\rho v_x)_x, \quad \text{...................................} (2.28)$$

and

$$\left\{\begin{array}{c}\text{Rate of}\\\text{mass}\\\text{out from V}\end{array}\right\}=\pi R^2(\rho v_x)_{x+\Delta x}. \quad \text{..} (2.29)$$

Substituting the Eq. 2.27, 2.28 and 2.29 into Eq. 2.26 gives

$$\pi R^2\Delta x\frac{\partial \rho}{\partial t}=2\pi R\gamma\Delta x(\rho v_r)_{r=R}+\pi R^2[(\rho v_x)_x-(\rho v_x)_{x+\Delta x}]. \quad \text{..............} (2.30)$$

Dividing Eq. 2.28 by $\pi R^2\Delta x$ and using the subscript of the reservoir inflow properties, it becomes

$$\frac{\partial \rho}{\partial t}=\frac{2\pi\gamma}{R}\rho_I v_I+\frac{[(\rho v_x)_x-(\rho v_x)_{x+\Delta x}]}{\Delta x}. \quad \text{.......................................} (2.31)$$

Taking $\Delta x \rightarrow 0$, this is rearranged into

$$\frac{\partial \rho}{\partial t}=\frac{2\gamma}{R}\rho_I v_I-\frac{\partial(\rho v_x)}{\partial x}. \quad \text{...} (2.32)$$

Finally, the mass balance equation for the steady-state condition is expressed in the form

$$\frac{d(\rho v_x)}{dx}=\frac{2\gamma}{R}\rho_I v_I. \quad \text{...} (2.33)$$

For multiphase conditions, the mass balance for phase j (=oil, water or gas) is given as

$$\frac{d(\rho_j v_j y_j)}{dx}=\frac{2\gamma}{R}\rho_{j,I}v_{j,I}y_{j,I}, \quad \text{...} (2.34)$$

where y_j is a volume fraction of phase j.

Momentum balance

Over a differential volume element of a wellbore, a momentum balance equation is expressed as (Yoshioka, 2007)

$$\left\{\begin{matrix} \text{Rate of} \\ \text{increase of} \\ \text{momentum} \end{matrix}\right\} = \left\{\begin{matrix} \text{Rate of} \\ \text{momentum} \\ \text{in} \end{matrix}\right\} - \left\{\begin{matrix} \text{Rate of} \\ \text{momentum} \\ \text{out} \end{matrix}\right\} + \left\{\begin{matrix} \text{External} \\ \text{force on} \\ \text{the fluid} \end{matrix}\right\}. \quad \text{......... (2.35)}$$

The rate of increase of momentum over the differential volume element in the axial direction is expressed as

$$\left\{\begin{matrix} \text{Rate of} \\ \text{increase of} \\ \text{momentum} \end{matrix}\right\} = \pi R^2 \Delta x \frac{\partial(\rho v_x)}{\partial t}. \quad \text{.. (2.36)}$$

The rate of momentum in and out are given as

$$\left\{\begin{matrix} \text{Rate of} \\ \text{momentum} \\ \text{in} \end{matrix}\right\} = 2\pi R \Delta x (\rho v_r v_x - \tau_{rx})_{r=R} + \pi R^2 (\rho v_x v_x + p - \tau_{xx})_x,$$

$$\text{... (2.37)}$$

and

$$\left\{\begin{matrix} \text{Rate of} \\ \text{momentum} \\ \text{out} \end{matrix}\right\} = \pi R^2 (\rho v_x v_x + p - \tau_{xx})_{x+\Delta x}, \quad \text{...................................... (2.38)}$$

where the first term in the Eq. 2.37 is the momentum in through the contact between the wellbore and reservoir, and the second term in the Eq. 2.37 and the Eq. 2.38 denotes the momentum in and out in the axial direction. The fluid is assumed to be Newtonian fluid and there is no slip at the wellbore-reservoir contact. Then, the shear stress and the axial velocity at the contact are given in the following form, respectively:

$$\tau_{xx} = \frac{4}{3}\mu \frac{\partial v_x}{\partial x}, \quad \text{.. (2.39)}$$

and

$$v_x|_{r=R} = 0. \quad \text{.. (2.40)}$$

In addition, the wall stress is given by introducing a fanning friction factor as

$$\tau_{rx}|_{r=R} = \frac{\rho f v_x^2}{2}, \quad \text{.. (2.41)}$$

where f denotes the friction factor. By substituting Eq. 2.39, 2.40 and 2.41, the Eq. 2.37 and 2.38 are rearranged into

$$\left\{\begin{array}{c} \text{Rate of} \\ \text{momentum} \\ \text{in} \end{array}\right\} = -2\pi R \Delta x \frac{\rho f v_x^2}{2} + \pi R^2 \left(\rho v_x v_x + p - \frac{4}{3}\mu \frac{\partial v_x}{\partial x}\right)_x, \quad \dots\dots\dots (2.42)$$

$$\left\{\begin{array}{c} \text{Rate of} \\ \text{momentum} \\ \text{out} \end{array}\right\} = \pi R^2 \left(\rho v_x v_x + p - \frac{4}{3}\mu \frac{\partial v_x}{\partial x}\right)_{x+\Delta x}. \quad \dots\dots\dots\dots\dots (2.43)$$

The external force on the fluid is given by

$$\left\{\begin{array}{c} \text{External} \\ \text{force on} \\ \text{the fluid} \end{array}\right\} = \pi R^2 \Delta x \rho g (\sin\theta). \quad \dots\dots\dots\dots\dots\dots\dots\dots (2.44)$$

Substituting Eq. 2.36, 2.42, 2.43 and 2.44 into Eq. 2.35 , dividing it by $\pi R^2 \Delta x$ and taking $\Delta x \to 0$, we obtain

$$\frac{\partial(\rho v_x)}{\partial t} = -\frac{\rho f v_x^2}{R} - \frac{\partial}{\partial x}\left[\rho v_x v_x + p - \frac{4}{3}\mu \frac{\partial v_x}{\partial x}\right] - \rho g(\sin\theta). \quad \dots\dots\dots (2.45)$$

When we assume the second derivative of the velocity is negligible and consider the steady-state condition, finally, the momentum balance equation for pressure distribution in the wellbore is expressed as

$$\frac{dp}{dx} = -\frac{\rho f v_x^2}{R} - \frac{d(\rho v_x v_x)}{dx} - \rho g(\sin\theta). \quad \dots\dots\dots\dots\dots\dots (2.46)$$

In Eq. 2.41, we introduce the friction factor. Ouyang et al. (1998) proposed a wall friction factor correlations for wellbore flow considering the reservoir inflow/outflow effect. The friction factor is estimated using the friction factor without radial influx and wall Reynolds number. For laminar flow, the friction factor is independent of completion type and is estimated by

$$f = f_{o,l}\left[1 + 0.04304\left(N_{Re,w}\right)^{0.6142}\right],$$

$$\dots\dots\dots\dots\dots\dots\dots\dots\dots\dots\dots\dots\dots\dots\dots\dots\dots\dots\dots\dots (2.47)$$

where $f_{o,l}$ is the friction factor of laminar flow without radial influx which is estimated as (Economides et al., 1994)

$$f_{o,l} = \frac{16}{N_{Re}}. \quad \dots\dots\dots\dots\dots\dots\dots\dots\dots\dots\dots\dots\dots\dots\dots\dots (2.48)$$

For turbulence flow, the friction factor for open-hole completion is given as

$$f = f_{o,t}\left(1 - 29.03\left(\frac{N_{Re,w}}{N_{Re}}\right)^{0.8003}\right), \quad \text{...} (2.49)$$

and for perforated well, it is

$$f = f_{o,t}\left(1 - 0.0153 N_{Re,w}{}^{0.3978}\right), \quad \text{...} (2.50)$$

where N_{Re} and $N_{Re,w}$ are the Reynolds number and the wall Reynolds number, respectively. These are given by

$$N_{Re} = \frac{2R\rho v}{\mu}, \quad \text{...} (2.51)$$

and

$$N_{Re,w} = \frac{2R\rho_I v_I}{\mu_I}. \quad \text{...} (2.52)$$

And $f_{o,t}$ is the friction factor for turbulence flow without radial influx, and it is estimated using the following Chen's correlation (Chen, 1979)

$$f_{o,t} = \left[-4\log\left\{\frac{\varepsilon}{3.7065} - \frac{5.0452}{N_{Re}}\log\left[\frac{\varepsilon^{1.1098}}{2.8257} + \left(\frac{7.149}{N_{Re}}\right)^{0.8991}\right]\right\}\right]^{-2}, \quad \text{............} (2.53)$$

where ε is the relative pipe roughness.

For multiphase conditions, the pressure profile and hold up along the well are estimated using three different approaches: a homogeneous, a drift flux, and a mechanistic model. Though a mechanistic model is the most realistic and it has the capability to the complicated situation, it sometimes encounters problems in convergence between flow regime transitions. Here, we use a homogeneous model, which is the simplest model for the multiphase flow.

For multiphase flow, the momentum balance is given using the homogenous model by

$$\frac{dp}{dx} = -\frac{\rho_m f v_m^2}{R} - \frac{d(\rho_m v_m v_m)}{dx} - \rho_m g(\sin\theta). \quad \text{...} (2.54)$$

For liquid-gas two-phase flow, the mixture properties are given by

$$\rho_m = \rho_l y_l + \rho_g y_g, \quad \text{..} (2.55)$$

$$\mu_m = \mu_l y_l + \mu_g y_g, \quad \text{..} (2.56)$$

and

$$v_m = v_{TP} = \frac{\rho_l}{\rho_m} v_{sl} + \frac{\rho_g}{\rho_m} v_{sg}, \quad \text{...} \quad (2.57)$$

where ρ_m is mixture density, ρ_l and ρ_g are the densities of liquid and gas, μ_m is the mixture viscosity, v_{TP} is the two phase velocity, v_{sl} and v_{sg} are the superficial velocities of liquid and gas. The dimensionless numbers for wall friction factor estimation are calculated using the mixture properties as

$$N_{Re} = \frac{\rho_m v_{TP} D}{\mu_m}, \quad \text{...} \quad (2.58)$$

and

$$N_{Re,w} = \frac{\rho_{m,I} v_{TP,I} D}{\mu_{m,I}}. \quad \text{..} \quad (2.59)$$

2.3.2 WELLBORE THERMAL MODEL

Over the differential volume element of a wellbore shown in Fig. 2.1, an energy conservation is expressed as

$$\begin{Bmatrix} \text{Rate of} \\ \text{increase of} \\ \text{energy} \end{Bmatrix} = \begin{Bmatrix} \text{Rate of} \\ \text{energy} \\ \text{in} \end{Bmatrix} - \begin{Bmatrix} \text{Rate of} \\ \text{energy} \\ \text{out} \end{Bmatrix} + \begin{Bmatrix} \text{Rate of work} \\ \text{done on system} \\ \text{by external force} \end{Bmatrix} + \begin{Bmatrix} \text{rate of} \\ \text{energy} \\ \text{production} \end{Bmatrix}$$

$$\text{...} \quad (2.60)$$

To express the total energy flux, we introduce the combined energy flux vector $\mathbf{e}$ as (Bird et al., 2002)

$$\mathbf{e} = \left(\frac{1}{2}\rho v^2 + \rho U\right) \mathbf{v} + [\boldsymbol{\pi} \cdot \mathbf{v}] + \mathbf{q}, \quad \text{...} \quad (2.61)$$

where this is the sum of the convective energy flux, the rate of doing work (per unit area) by molecular mechanisms, and the rate of transporting heat (per unit area) by molecular mechanisms. The total molecular stress tensor $\boldsymbol{\pi}$ is split into two components, and $\boldsymbol{\pi}$ is expressed as $\boldsymbol{\pi} = p\boldsymbol{\delta} + \boldsymbol{\tau}$ where p denotes the normal stress and $\boldsymbol{\tau}$ denotes the shear stress, so that $[\boldsymbol{\pi} \cdot \mathbf{v}] = p\mathbf{v} + [\boldsymbol{\tau} \cdot \mathbf{v}]$. According to the definition, enthalpy H is expressed as Eq. 2.21. Then Eq. 2.61 is written in the form

$$\mathbf{e} = \left(\frac{1}{2}\rho v^2 + \rho H\right) \mathbf{v} + [\boldsymbol{\tau} \cdot \mathbf{v}] + \mathbf{q}. \quad \text{...} \quad (2.62)$$

The rate of increase of energy over the differential volume element $\pi R^2 \Delta x$ is

$$\left\{\begin{array}{c} \text{Rate of} \\ \text{increase of} \\ \text{energy} \end{array}\right\} = \pi R^2 \Delta x \frac{\partial}{\partial t}\left(\frac{1}{2}\rho v^2 + \rho U\right), \quad \text{...............................} (2.63)$$

where $\frac{1}{2}\rho v^2$ is the kinetic energy per unit volume and ρU is the internal energy per unit volume. Next, the rate of energy in is

$$\left\{\begin{array}{c} \text{Rate of} \\ \text{energy} \\ \text{in} \end{array}\right\} = 2\pi R \Delta x (e_r)_{r=R} + \pi R^2 (e_x)_x, \quad \text{...............................} (2.64)$$

where e_r and e_x are the combined energy flux in the radial direction and the axial direction, respectively. And, the rate of energy out is

$$\left\{\begin{array}{c} \text{Rate of} \\ \text{energy} \\ \text{out} \end{array}\right\} = \pi R^2 (e_x)_{x+\Delta x}. \quad \text{...............................} (2.65)$$

Because the rate of work done over the differential volume element $(\pi R^2 \Delta x)$ by external force arises from gravity force, it is expressed as

$$\left\{\begin{array}{c} \text{Rate of work} \\ \text{done on system} \\ \text{by external force} \end{array}\right\} = -\pi R^2 \Delta x \rho v g (\sin\theta). \quad \text{...............................} (2.66)$$

Because the energy production in the system is assumed to be zero, substituting the Eq. 2.63, 2.64, 2.65 and 2.66 into Eq. 2.60 and taking $\Delta x \to 0$, we obtain

$$\frac{\partial}{\partial t}\left(\frac{1}{2}\rho v^2 + \rho U\right) = \frac{2}{R}(e_r)_{r=R} - \frac{\partial}{\partial x}e_x - \rho v g(\sin\theta), \quad \text{...............................} (2.67)$$

where the radial combined energy flux at the wall is expressed as

$$(e_r)_{r=R} = \left(\frac{1}{2}\rho_I v_I{}^2 + \rho_I H_I\right)v_I + q_I - (\tau_{rx}v_x)_{r=R} - (\tau_{rr}v_r)_{r=R},$$

$$\text{...............................} (2.68)$$

and also the combined energy flux in the axial direction is expressed as

$$e_x = \left(\frac{1}{2}\rho_x v_x{}^2 + \rho_x H\right)v_x + q_x - \tau_{xr}v_r - \tau_{xx}v_x. \quad \text{...............................} (2.69)$$

Using Eq. 2.40 and

$$\tau_{rr} = \frac{2}{3}\mu\frac{\partial v_r}{\partial r}\Big|_{r=R} - \frac{2}{3}\mu\frac{v_I}{R} - \frac{2}{3}\mu\frac{\partial v_x}{\partial x}\Big|_{r=R} = -\frac{2}{3}\mu\frac{v_I}{R}, \quad \text{...............................} (2.70)$$

Eq. 2.68 becomes

$$(e_r)_{r=R} = \left(\frac{1}{2}\rho_I v_I{}^2 + \rho_I H_I\right) v_I + q_I + \frac{2}{3}\mu\frac{v_I{}^2}{R}, \quad\text{..........................}(2.71)$$

and also using 2.39 and 2.40, Eq. 2.69 becomes

$$e_x = \left(\frac{1}{2}\rho_x v_x{}^2 + \rho_x H\right) v_x + q_x - \frac{4}{3}\mu\frac{\partial v_x}{\partial x}v_x. \quad\text{..........................}(2.72)$$

The heat conduction between fluids is assumed to be negligible, and then over the covered area of the pipe only the heat conduction occurs and over the open area of the pipe only the heat convection occurs. Fig. 2.3 shows the schematic of the energy transport through a perforated pipe.
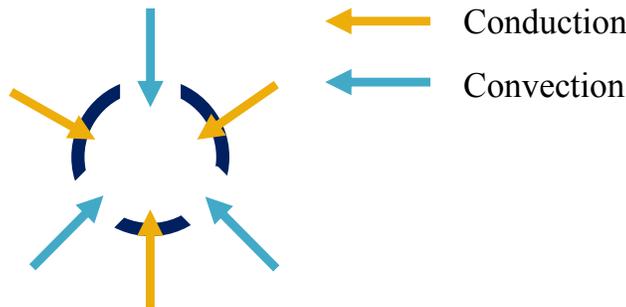

Fig. 2.3 Schematic of energy transport through a perforated pipe

Hence, using the pipe open ratio Eq. 2.71 is written in the form

$$(e_r)_{r=R} = \gamma\left(\frac{1}{2}\rho_I v_I{}^2 + \rho_I H_I + \frac{2}{3}\mu\frac{v_I}{R}\right)v_I + (1-\gamma)q_I, \quad\text{..................}(2.73)$$

and the Eq. 2.72 can also be written in the form ($q_x = 0$)

$$e_x = \left(\frac{1}{2}\rho_x v_x{}^2 + \rho_x H\right)v_x - \frac{4}{3}\mu\frac{\partial v_x}{\partial x}v_x. \quad\text{...............................}(2.74)$$

Substituting Eq. 2.73 and 2.74 into Eq. 2.67 and rearranging it gives

$$\frac{\partial}{\partial t}(\rho U) = \frac{2\gamma}{R}\rho_I H_I v_I + \frac{2(1-\gamma)}{R}q_I - \frac{\partial}{\partial x}(\rho_x H v_x) - \rho v g(\sin\theta) + E_{KE} + E_{VS}$$

$$\text{...}(2.75)$$

where E_{KE} is the kinetic energy term, and E_{VS} is the viscous shear term, and these are expressed as

$$E_{KE} = \frac{2\gamma}{R}\left(\frac{1}{2}\rho_I v_I{}^2\right) - \frac{\partial}{\partial x}\left[\left(\frac{1}{2}\rho v_x{}^2\right)v_x\right], \quad\text{...(2.76)}$$

and

$$E_{VS} = \frac{4}{3}\frac{\gamma}{R}\left[\mu\frac{v_I}{R}\right]v_I + \frac{4}{3}\frac{\partial}{\partial x}\left[\mu\frac{\partial v_x}{\partial x}v_x\right]. \quad\text{...(2.77)}$$

Expanding the LHS and the third term in Eq. 2.75, we obtain

$$\frac{\partial}{\partial t}(\rho U) = \rho\frac{\partial U}{\partial t} + U\frac{\partial \rho}{\partial t}, \quad\text{...(2.78)}$$

and

$$\frac{\partial}{\partial x}(\rho_x H v_x) = H\frac{\partial(\rho_x v_x)}{\partial x} + \rho_x v_x\frac{\partial H}{\partial x}. \quad\text{.......................................(2.79)}$$

Using Eq. 2.21 and the mass balance equation 2.33, Eq. 2.78 is written in the form

$$\frac{\partial}{\partial t}(\rho U) = \rho\frac{\partial H}{\partial t} - \frac{\partial p}{\partial t} + \frac{2\gamma}{R}\rho_I H v_I - H\frac{\partial(\rho v_x)}{\partial x}. \quad\text{..(2.80)}$$

Substituting Eq. 2.79 and 2.80 into Eq. 2.75 and rearranging it, we obtain

$$\rho\frac{\partial H}{\partial t} - \frac{\partial p}{\partial t} = \frac{2\gamma}{R}\rho_I v_I(H_I - H) + \frac{2(1-\gamma)}{R}q_I - \rho_x v_x\frac{\partial H}{\partial x} - \rho v g(\sin\theta) + E_{KE} + E_{VS}.$$

$$\text{..(2.81)}$$

According to Eq. 2.19, the first term in the LHS of Eq. 2.81 and the third term in the RHS of Eq. 2.81 are expressed as

$$\frac{\partial H}{\partial t} = C_p\frac{\partial T}{\partial t} + \frac{1}{\rho}(1 - \beta T)\frac{\partial p}{\partial t}, \quad\text{..(2.82)}$$

and

$$\frac{\partial H}{\partial x} = C_p\frac{\partial T}{\partial x} + \frac{1}{\rho}(1 - \beta T)\frac{\partial p}{\partial x}. \quad\text{..(2.83)}$$

In order to get the enthalpy difference, we take the integral of Eq. 2.19 and it becomes

$$H_I - H = \int_T^{T_I} C_p dT + \int_p^{p_I} \frac{1}{\rho}(1 - \beta T)dp. \quad\text{...(2.84)}$$

The heat capacity and $\frac{1}{\rho}(1 - \beta T)$ are assumed to be constant, and then we obtain

$$H_I - H = C_p(T_I - T) + \frac{1}{\rho}(1 - \beta T)(p_I - p). \quad\text{...(2.85)}$$

Let the inflow pressure be the same with the wellbore pressure, the enthalpy difference is expressed as

$$H_I - H = C_p(T_I - T). \quad\text{...(2.86)}$$

Substituting Eq. 2.82, 2.83 and 2.86 into Eq. 2.81, finally, the transient energy balance equation is expressed in the form (Sui, 2009)

$$\rho C_p \frac{\partial T}{\partial t} - \beta T \frac{\partial p}{\partial t} = \frac{2\gamma}{R} \rho_I v_I C_p (T_I - T) + \frac{2(1-\gamma)}{R} q_I - \rho_x v_x C_p \frac{\partial T}{\partial x}$$

$$-v_x(1 - \beta T)\frac{\partial p}{\partial x} - \rho v g(\sin\theta) + E_{KE} + E_{VS}. \quad \text{...}(2.87)$$

Here, the Joule –Thomson effect coefficient is defined as

$$K_{JT} = \frac{\beta T - 1}{\rho C_p}. \quad \text{..}(2.88)$$

And, the heat conduction between the formation and wellbore is expressed as

$$q_I = U_T(T_I - T), \quad \text{...}(2.89)$$

where U_T is the overall heat transfer coefficient. For the completion of the casing and cementing, it is defined as

$$U_T = \left[R\left(\frac{\ln\frac{r_{c,OD}}{R}}{K_{casing}} + \frac{\ln\frac{r_w}{r_{c,OD}}}{K_{cement}} + \frac{1}{C_h}\right)\right]^{-1}, \quad \text{..}(2.90)$$

where C_h is the heat transfer coefficient, K_{casing} and K_{cement} are the constant thermal conductivity of the casing and cement, respectively. When we assume that the convective heat transfer is negligible inside wellbore, Eq. 2.90 is written in

$$U_T = \left[R\left(\frac{\ln\frac{r_{c,OD}}{R}}{K_{casing}} + \frac{\ln\frac{r_w}{r_{c,OD}}}{K_{cement}}\right)\right]^{-1}. \quad \text{..}(2.91)$$

Fig. 2.4 shows the geometry near the wellbore for the case of casing and cementing. Using Eq. 2.88 and 2.89, Eq. 2.87 is written as

$$\rho C_p \frac{\partial T}{\partial t} - \beta T \frac{\partial p}{\partial t} = \frac{2}{R}(\gamma \rho_I v_I C_p + (1-\gamma)U_T)(T_I - T) - \rho_x v_x C_p \frac{\partial T}{\partial x}$$

$$+\rho v_x C_p K_{JT} \frac{\partial p}{\partial x} - \rho v g(\sin\theta) + E_{KE} + E_{VS}. \quad \text{......}(2.92)$$

For steady-state condition, this becomes

$$\rho_x v_x C_p \frac{dT}{dx} = \frac{2}{R}(\gamma \rho_I v_I C_p + (1-\gamma)U_T)(T_I - T) + \rho v_x C_p K_{JT} \frac{dp}{dx}$$

$$-\rho v g(\sin\theta) + E_{KE} + E_{VS}. \quad \text{................................}(2.93)$$

Yoshioka (2007) performed sensitivity studies and conclude the kinetic energy and viscous shear are less important to the temperature profile. Finally, the steady state energy balance equation is expressed in the form
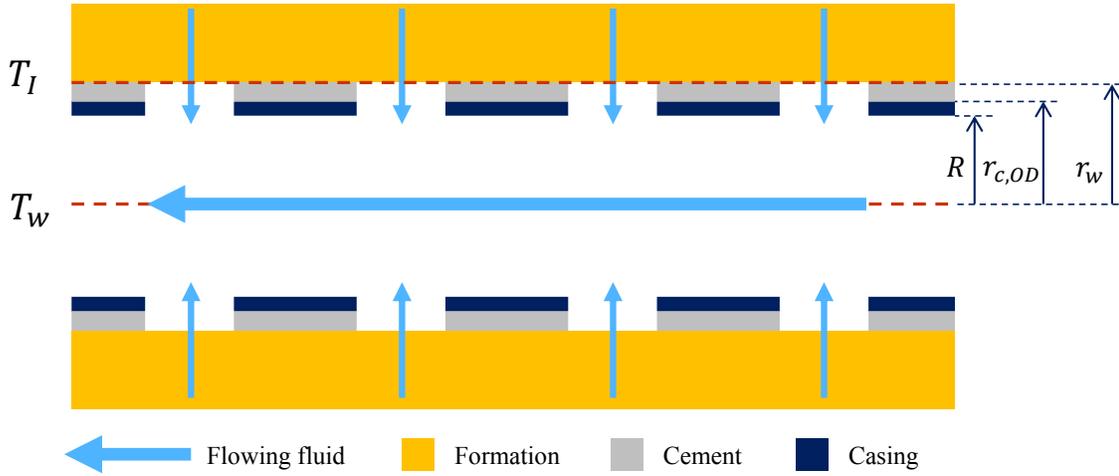
Fig. 2.4 Geometry near the wellbore

$$\rho_x v_x C_p \frac{dT}{dx} = \frac{2}{R} \left(\gamma \rho_I v_I C_p + (1-\gamma) U_T \right)(T_I - T) + \rho v_x C_p K_{JT} \frac{dp}{dx} - \rho v g (\sin \theta).$$

$$\text{...(2.94)}$$

For multiphase flow, the energy balance for phase j is

$$\rho_j v_j y_j C_{p,j} \frac{dT_j}{dx} = \frac{2}{R} \left(\gamma \rho_{j,I} v_{j,I} y_{j,I} C_{p,j} + (1-\gamma) U_T \right)(T_{j,I} - T_j)$$

$$+ \rho_j v_j y_j C_{p,j} K_{JT,j} \frac{dp_j}{dx} - \rho_j v_j y_j g (\sin \theta). \quad \text{......} \quad (2.95)$$

Summation of the equation for the existing phases (N_p) gives

$$\sum_j^{N_p} \rho_j v_j y_j C_{p,j} \frac{dT_j}{dx} = \sum_j^{N_p} \rho_j v_j y_j C_{p,j} K_{JT,j} \frac{dp_j}{dx} + \frac{2}{R} \gamma \sum_j^{N_p} \rho_{j,I} v_{j,I} y_{j,I} C_{p,j}$$

$$+ (1-\gamma) U_T \sum_j^{N_p} \left(T_{j,I} - T_j \right) - \sum_j^{N_p} \rho_j v_j y_j g (\sin \theta). \quad \text{......} (2.96)$$

When we assume that each phase has the same pressure and temperature, Eq. 2.96 becomes

$$\frac{dT}{dx} \sum_j^{N_p} \rho_j v_j y_j C_{p,j} = \frac{dp}{dx} \sum_j^{N_p} \rho_j v_j y_j C_{p,j} K_{JT,j} + \frac{2}{R} \gamma \sum_j^{N_p} \rho_{j,I} v_{j,I} y_{j,I} C_{p,j}$$

$$+ (1-\gamma) U_T (T_I - T) - \sum_j^{N_p} \rho_j v_j y_j g (\sin \theta). \quad \text{...............} (2.97)$$

Let total properties be

$$\sum_j^{N_p} \rho_j v_j y_j = (\rho v)_T, \quad \text{...(2.98)}$$

33

$$\sum_j^{Np} \rho_j v_j y_j C_{p,j} = \left(\rho v C_p\right)_T, \quad \dots\dots\dots\dots\dots\dots\dots\dots\dots\dots\dots\dots\dots\dots\dots\dots\dots (2.99)$$

and

$$\sum_j^{Np} \rho_j v_j y_j C_{p,j} K_{JT,j} = \left(\rho v C_p K_{JT}\right)_T. \quad \dots\dots\dots\dots\dots\dots\dots\dots\dots\dots\dots\dots\dots (2.100)$$

Finally, the steady state energy balance equation for multiphase flow is expressed in the form:

$$\frac{dT}{dx} = \frac{\left(\rho v C_p K_{JT}\right)_T}{\left(\rho v C_p\right)_T}\frac{dp}{dx} + \frac{2}{R}\frac{\gamma\left(\rho v C_p\right)_{T,I}+(1-\gamma)U_T}{\left(\rho v C_p\right)_T}(T_I - T) - \frac{\left(\rho v\right)_T}{\left(\rho v C_p\right)_T}g(\sin\theta).$$

$$\dots\dots\dots\dots\dots\dots\dots\dots\dots\dots\dots\dots\dots\dots\dots\dots\dots\dots\dots\dots\dots\dots (2.101)$$

2.4 INTEGRATED MODEL FOR TEMPERATURE AT RESERVOIR AND WELLBORE CONTACT

In order to solve temperature distribution inside wellbore using Eq. 2.101, the arriving temperature T_I is computed. Though it is estimated directly when the analytical solution for reservoir flow and thermal model are used (Hasan and Kabir, 1994; Sui et al., 2008a; Yoshioka et al., 2007), in this work, T_I is estimated based on the computed reservoir temperature using Eq. 2.23. We use the arriving temperature model presented by Li and Zhu (2010). In the following derivation, the axial direction of the wellbore is assumed to be the x-direction.

The following assumptions have been made to solve T_I: (Li, 2010)

1) Reservoir grid temperature and pressure are located at the effective radius, r_{eff}, which follows the definition of Peaceman's model: (Peaceman, 1983)

$$r_{eff} = 0.28\frac{\left[(k_z/k_y)^{0.5}(\Delta y)^2+(k_y/k_z)^{0.5}(\Delta y)^2\right]^{0.5}}{(k_z/k_y)^{0.25}+(k_y/k_z)^{0.25}}. \quad \dots\dots\dots\dots\dots\dots\dots\dots (2.102)$$

2) The permeability is isotropic and homogeneous in the wellbore grid which is given by

$$k_e = \sqrt{k_y \cdot k_x}. \quad \dots\dots\dots\dots\dots\dots\dots\dots\dots\dots\dots\dots\dots\dots\dots\dots\dots\dots\dots\dots (2.103)$$

3) Fluid flow from the effective radius to the wellbore is radial flow.

4) In one time step, both the pressure and temperature are assumed to be steady state in the wellbore grid.

5) Due to the small distance between wellbore and wellbore grid boundary, the fluid properties and saturation are treated as constant.

6) Effects of capillary pressure and gravity are ignored.

7) Fluid velocity near wellbore follows Darcy's law.

Fig. 2.5 shows the geometry of the integrated model, and it presents the names and the locations of the pressure and temperature in the reservoir grid which contains the wellbore.
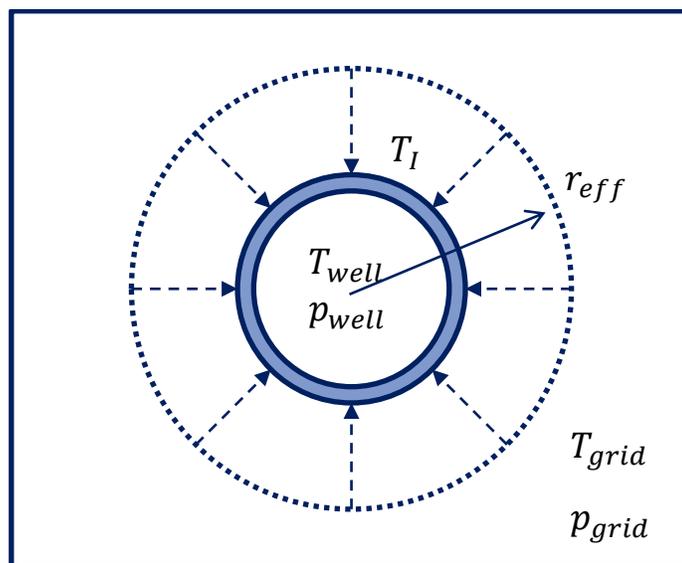
Fig. 2.5 Integrated model geometry, and pressures and temperatures in the reservoir grid which contains the wellbore

Under these assumptions, the pressure distribution from the effective wellbore radius to wellbore is given by

$$\frac{d^2p}{dr^2} + \frac{1}{r}\frac{dp}{dr} = 0, \quad\text{..}(2.104)$$

and the boundary conditions are

$$p = p_{grid} \qquad\qquad \text{at } r = r_{eff} \quad\text{.....................................}(2.105)$$

$$p = p_I \qquad\qquad\quad \text{at } r = r_w. \quad\text{.....................................}(2.106)$$

The solution is

$$p = a\ln\frac{r}{r_w} + p_I \quad\text{..}(2.107)$$

where

$$a = \frac{p_{grid}-p_I}{\ln(r_{eff}/r_w)}. \quad\text{...}(2.108)$$

The reservoir temperature equation is simplified into the 1-D form as

$$\sum_{j=1}^{N_p}(\rho_j u_{r,j} C_{p,j})\frac{dT}{dr} - \sum_{j=1}^{N_p}(\beta_j u_{r,j})T\frac{dp}{dr} - K_{Tt}\frac{1}{r}\frac{d}{dr}\left(r\frac{dT}{dr}\right) + \sum_{j=1}^{N_p} u_{r,j}\frac{dp}{dr} = 0,$$

$$\text{...}(2.109)$$

and the boundary conditions for the temperature equation are:

$$T = T_{grid}, \qquad\qquad \text{at } r = r_{eff} \quad\text{.....................................}(2.110)$$

$$K_{Tt}\frac{dT}{dr}\bigg|_{r=r_w} = U_T\big(T|_{r=r_w} - T_w\big), \text{ at } r = r_w \quad\text{...........................}(2.111)$$

Darcy's law gives the fluid velocity for each phase as

$$u_{rj} = -k_e\frac{k_{rj}}{\mu_j}\frac{dp}{dr} = -k_e\frac{k_{rj}}{\mu_j}\frac{a}{r}. \quad\text{..}(2.112)$$

Substituting Eq. 2.107, 2.108 and 2.112 into Eq. 2.109, and rearranging it, a second order ordinary differential equation for temperature is expressed as

$$\sum_{j=1}^{N_p}\left(\rho_j C_{p,j}\frac{k_e k_{rj}}{\mu_j}a\right)\frac{1}{r}\frac{dT}{dr} - \sum_{j=1}^{N_p}\left(\beta_j\frac{k_e k_{rj}}{\mu_j}a^2\right)\frac{T}{r^2}$$

$$+K_{Tt}\frac{1}{r}\frac{d}{dr}\left(r\frac{dT}{dr}\right) + \sum_{j=1}^{N_p}\left(\frac{k_e k_{rj}}{\mu_j}a^2\right)\frac{1}{r^2} = 0. \quad\text{..............}(2.113)$$

Because the fluid properties and saturations are assumed to be constant in one time step, Eq. 2.111 becomes simplified into

$$K_{Tt}r^2\frac{d^2T}{dr^2} + C_1 r\frac{dT}{dr} - C_2 T + C_3 = 0, \quad\text{.....................................}(2.114)$$

where

$$C_1 = \sum_{j=1}^{N_p} \left(\rho_j C_{p,j} \frac{k_e k_{rj}}{\mu_j} a \right) + K_{Tt}, \quad \text{...} \quad (2.115)$$

$$C_2 = \sum_{j=1}^{N_p} \left(\beta_j \frac{k_e k_{rj}}{\mu_j} a^2 \right), \quad \text{...} \quad (2.116)$$

and

$$C_3 = \sum_{j=1}^{N_p} \left(\frac{k_e k_{rj}}{\mu_j} a^2 \right). \quad \text{...} \quad (2.117)$$

Then, the solution for the second-order ordinary differential equation is

$$T = c_1 r^{n_1} + c_2 r^{n_2} + b, \quad \text{...} \quad (2.118)$$

where

$$n_1 = -\frac{\omega}{2} + \frac{1}{2} \sqrt{\omega^2 + 4 \frac{k_e a^2}{K_{Tt}} \left(\sum_{j=1}^{N_p} \frac{k_{rj}}{\mu_j} \beta_j \right)}, \quad \text{.................................} \quad (2.119)$$

$$n_2 = -\frac{\omega}{2} - \frac{1}{2} \sqrt{\omega^2 + 4 \frac{k_e a^2}{K_{Tt}} \left(\sum_{j=1}^{N_p} \frac{k_{rj}}{\mu_j} \beta_j \right)}, \quad \text{.................................} \quad (2.120)$$

$$c_1 = \frac{\left(\frac{n_2}{r_w} - \frac{U_T}{K_{Tt}} \right) r_w^{n_2} (T_{grid} - b) - \frac{U_T}{K_{Tt}} r_{eff}^{n_2} (b - T_w)}{\left(\frac{n_2}{r_w} - \frac{U_T}{K_{Tt}} \right) r_{eff}^{n_1} r_w^{n_2} - \left(\frac{n_1}{r_w} - \frac{U_T}{K_{Tt}} \right) r_w^{n_1} r_{eff}^{n_2}}, \quad \text{.....................} \quad (2.121)$$

$$c_2 = \frac{\left(\frac{n_1}{r_w} - \frac{U_T}{K_{Tt}} \right) r_w^{n_1} (b - T_{grid}) + \frac{U_T}{K_{Tt}} r_{eff}^{n_1} (b - T_w)}{\left(\frac{n_2}{r_w} - \frac{U_T}{K_{Tt}} \right) r_{eff}^{n_1} r_w^{n_2} - \left(\frac{n_1}{r_w} - \frac{U_T}{K_{Tt}} \right) r_w^{n_1} r_{eff}^{n_2}}, \quad \text{.....................} \quad (2.122)$$

$$\omega = \left(\sum_{j=1}^{N_p} \rho_j C_{p,j} \frac{k_{rj}}{\mu_j} \right) \frac{k_e a}{K_{Tt}}, \quad \text{...} \quad (2.123)$$

and

$$b = \frac{\sum_{j=1}^{N_p} \frac{k_{rj}}{\mu_j}}{\sum_{j=1}^{N_p} \frac{k_{rj}}{\mu_j} \beta_j}. \quad \text{...} \quad (2.124)$$

Therefore, the arriving temperature is computed by substituting $r = r_w$ into Eq. 2.118.

According to these equations, the reservoir wellbore grid temperature, arriving temperature and wellbore temperature are coupled together. Given reservoir gird temperature, inflow temperature and wellbore temperature is estimated iteratively. The detail solution procedure for the simulation is discussed in the next section.

2.5   SOLUTION PROCEDURE

In this study, because the reservoir temperature change is assumed to be very small, it does not affect fluid properties, which means reservoir pressure and saturation computation is independent to reservoir temperature computation. Then, the reservoir fluid properties is estimated using the correlations for the non-isothermal fluid properties, and during the simulation only the pressure change and saturation change are taken into account for the computation of fluid properties. Fig. 2.6 shows the detail procedure of the simulation in this work.

At each time step, the model calculates reservoir pressure and saturation distributions. Then, the wellbore pressure distribution is solved using wellbore pressure model. Using the solved reservoir pressure and saturation distribution, reservoir temperature distribution is solved. Since the reservoir thermal model contains the sink/source term which includes the wellbore and arriving temperature, those values at previous time step is used, at first. Next, we estimate arriving temperature using the calculated reservoir temperature distribution and the wellbore temperature at previous time step, and also estimate the wellbore temperature using the estimated arriving temperature. Then, we update the arriving temperature and wellbore temperature iteratively until the wellbore temperature converged. To obtain more accurate temperature results, run the reservoir thermal model again using the updated inflow and wellbore temperature for sink/source term, and update inflow temperature and wellbore temperature again until the wellbore temperature converged. After the well temperature converged globally in these steps, we move to next time step.
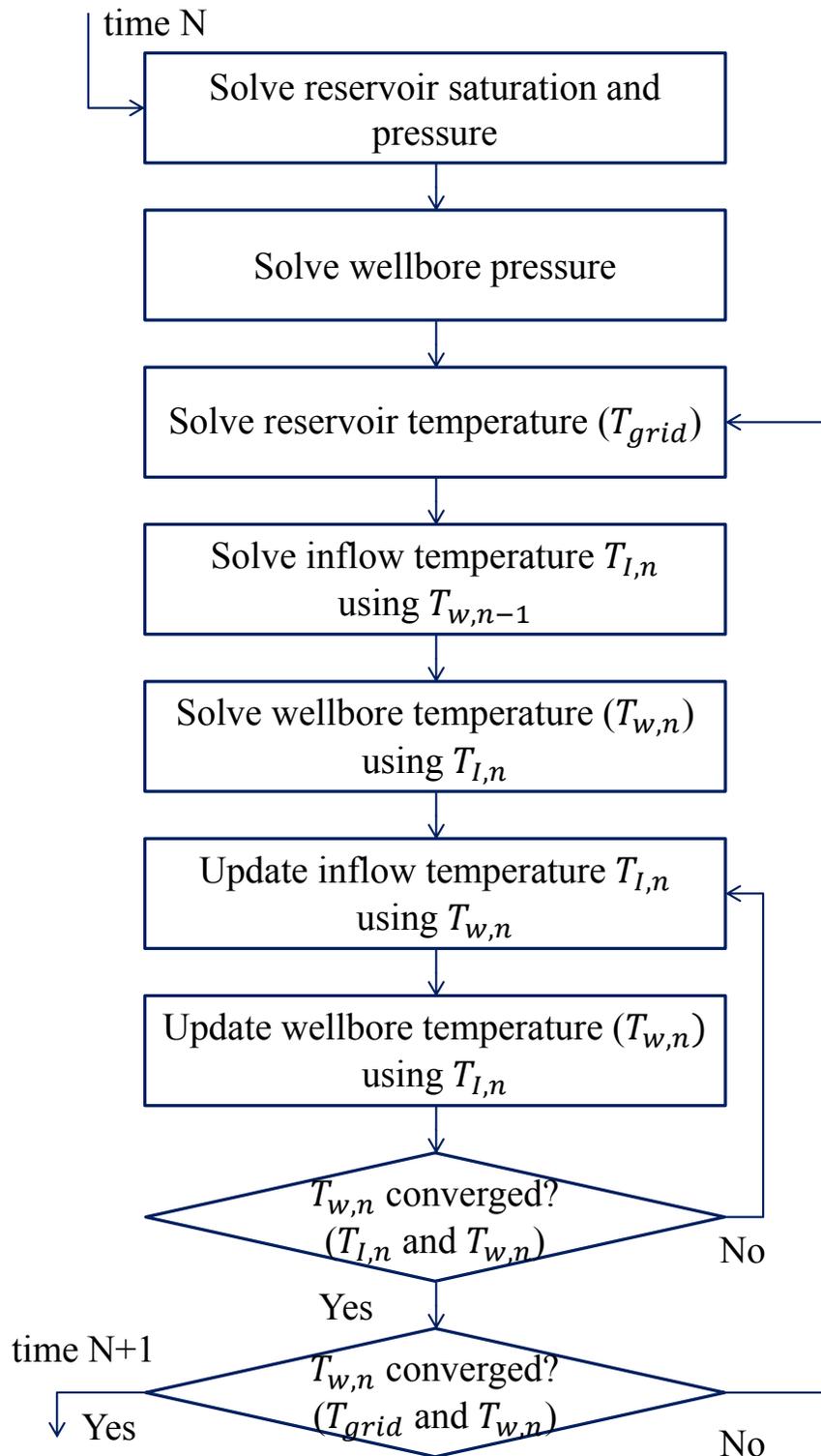
Fig. 2.6 Solution procedure

3 TEMPERATURE PREDICTION MODEL IN SHALE RESERVOIR

3.1 INTRODUCTION

In this section, a reservoir and wellbore model is set up for multiple transverse hydraulic fractured horizontal well in a shale reservoir. At first, a general approach for the modeling of shale gas reservoir is described in order to incorporate completion designs of multiple transverse hydraulic fractures and modeling methods of a complex network structure near wellbore. Then, some synthetic examples are shown to find fundamental mechanisms of temperature behavior in the wellbore. Fracture heterogeneities, network fracture effects and boundary condition effects are also examined through these examples.

3.2 MODELING FOR SHALE RESERVOIR

In shale reservoir modeling, it is important to consider the way to express the complex completion designs and complex network structures induced or reactivated by multiple stage hydraulic fracturing treatment when the Barnett type of fracturing fluid (waterfracs) is used in the treatment. **Fig. 3.1** shows the variation of structures created by hydraulic fracturing treatment, and the case of usage of the waterfracs leads to the extremely complex structure while the usage of conventional high viscosity fracturing fluid leads to a simple bi-wing fractures. The stimulated reservoir volume as the effective drainage volume is estimated based on the created network structures, and it is used for prediction of well performance (Mayerhofer et al., 2010). Therefore, the simulation model for the stimulated reservoir volume is required, and several methods were proposed for the expression of the fracture network structures. These are grouped into two methods: discrete fracture network model and multiple-porosity model.
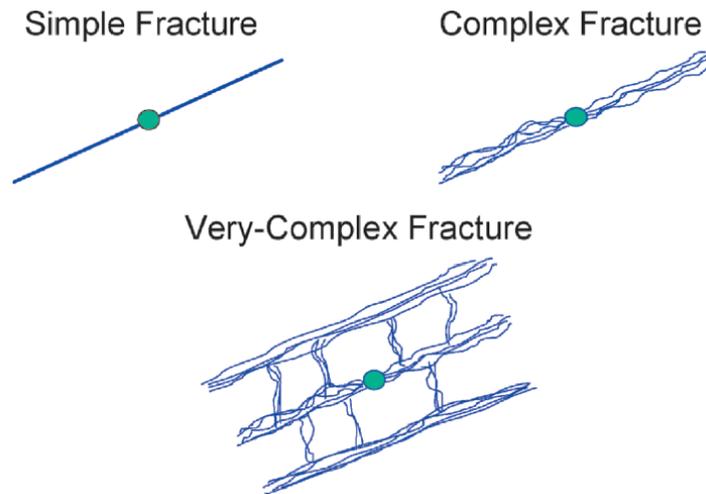
Fig. 3.1 Variation of fracture structures created by hydraulic fracturing treatment (Fisher et al., 2005)

In the discrete fracture network model, the fracture network is expressed as a discrete set of high permeability fractures. Cipolla et al. (2010a) presented a numerical reservoir simulation model using a detailed numerical grid that rigorously represents the network fractures, hydraulic fracture, matrix block and unstimulated areas. **Fig. 3.2** shows the detailed reservoir simulation grid design using the discrete fracture network model, and the example comparison of the pressure field after three moth production in shale and tight gas reservoir with planar fractures and network fractures. This model can rigorously express the transient behavior of the shale reservoir, but it requires huge amount of computational efforts. On the other hand, in the multiple-porosity model, the reservoir is represented by several overlapping continua. Originally, a dual porosity approach, one of the multiple porosity models, is used for the expression of naturally fractured reservoir. In dual porosity model, each reservoir grid contains matrix and fracture, and the flow and heat transfer between the matrix and fracture is controlled by shape factor, and this is the upscaling of the properties such as fracture permeability and porosity from the discrete fracture network model to the dual porosity system taking into account the complex fracture system and connectivity (Zhang et al., 2009) (**Fig. 3.3a**).

Then, in the application of the dual porosity model, the hydraulic fractures were expressed as discrete planar fractures and the fracture network was expressed dual porosity region in the vicinity of the planar hydraulic fractures (**Fig. 3.3b**). Multiple-porosity methods can reduce computational efforts comparing to the discrete fracture network model, but typically the analytical solution used in these models cannot capture the very long transient behavior in the matrix blocks exhibited by shale gas reservoir (Cipolla et al., 2010a).

In this work, we took the same approach with Yin et al. (2011) who used an enhanced permeability area to approximate the enhancement effect by the network fracture as the higher permeable matrix zone in the vicinity of the fractures. In this method, the hydraulic fractures were expressed as the higher permeable grids, and the enhanced permeability area exists along the fracture grid to consider the stimulated reservoir volume (**Fig. 3.4**). This approach approximated the matrix-fracture system to the enhanced permeable matrix zone, and then certain amount of errors should exist, but it reduces the computational efforts because of its single porosity, coarse grid system comparing to the discrete fracture network model and also makes us free from the several parameters such as shape factor used in multiple-porosity system.

In detail on the grid design, the hydraulic fractures are expressed by thin grids explicitly and the induced network fractures are expressed as the enhanced permeability area in the vicinity of the created planar hydraulic fractures. Here, we assume that the matrix has the homogeneous and isotropic permeability.

Fig. 3.5 shows the example schematics of the reservoir/wellbore geometries which has three hydraulic fractures/clusters along the horizontal well (**Fig. 3.5a**). After the work by Cipolla et al. (2010b), complex network structures are approximated by planar hydraulic fractures and network fractures perpendicular to hydraulic fractures (**Fig 3.5b**). Because this is assumed to be very tight formation, the drainage area is limited to the near wellbore zone stimulated by hydraulic fractures and induced networks. **Fig. 3.6** shows the simulation gridding of the network structure using the enhanced permeability area, which is used to express the stimulated reservoir volume by higher permeability

zone. The hydraulic fractures are expressed as the explicit grid (red line), the stimulated reservoir volume is expressed as enhanced permeability area (blue region), and outside of the stimulated reservoir volume there is the region of matrix permeability (gray region).
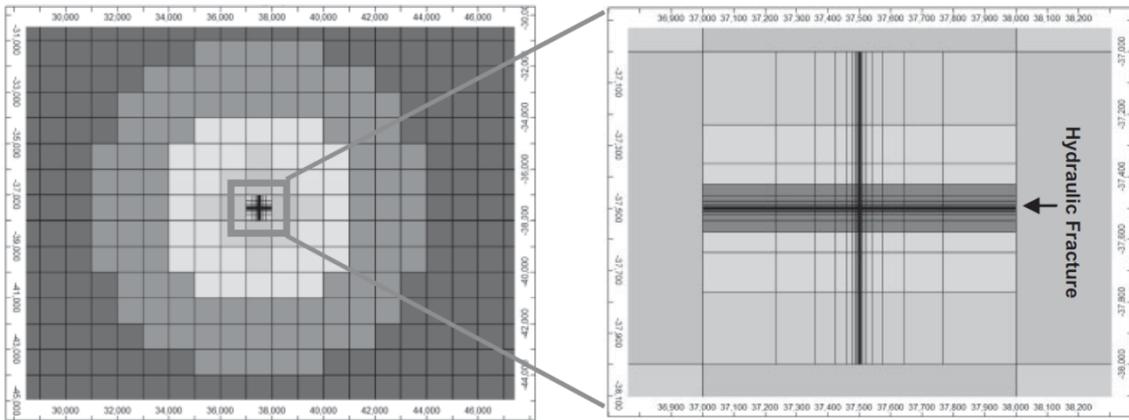
a) **Detailed numerical gridding design proposed by Cipolla et al. (2010a)**
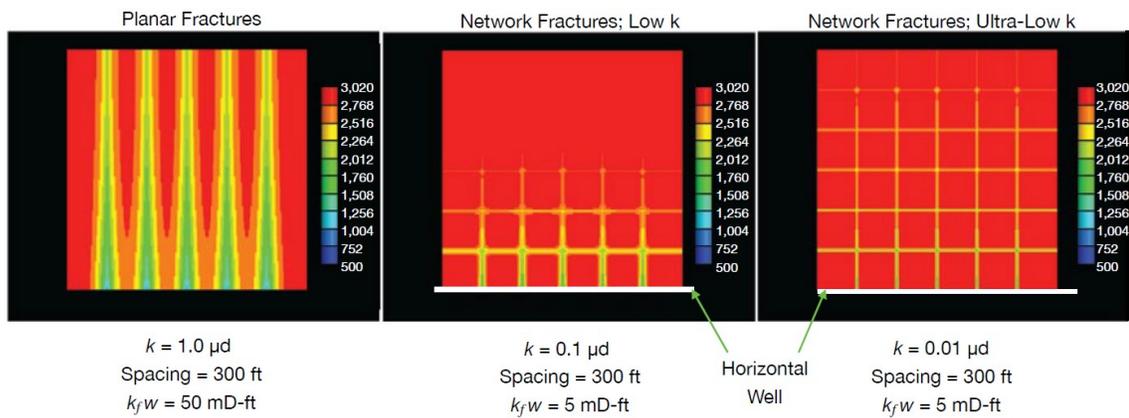
b) **Example comparison of the pressure field after three moth production with planar fractures and network fractures (Warpinski et al., 2009)**

Fig. 3.2 Grid design and example calculation of discrete fracture network model
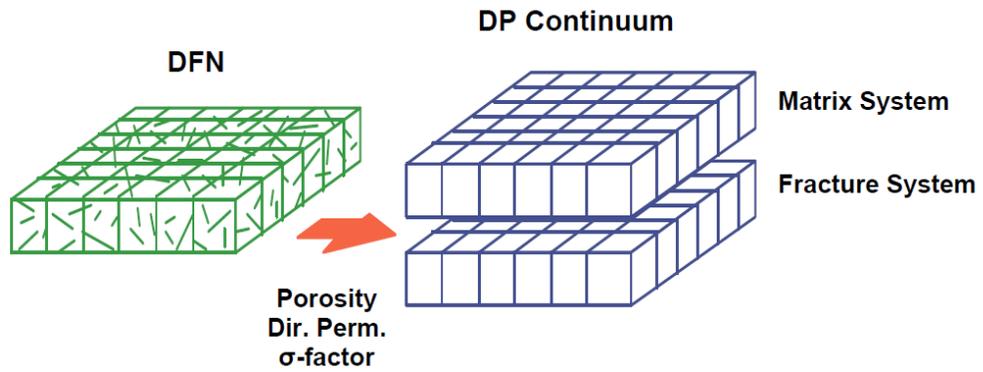
a) Upscaling of properties from the discrete fracture network model to dual porosity system (Zhang et al., 2009)

Dual-porosity regions   Hydraulic fractures
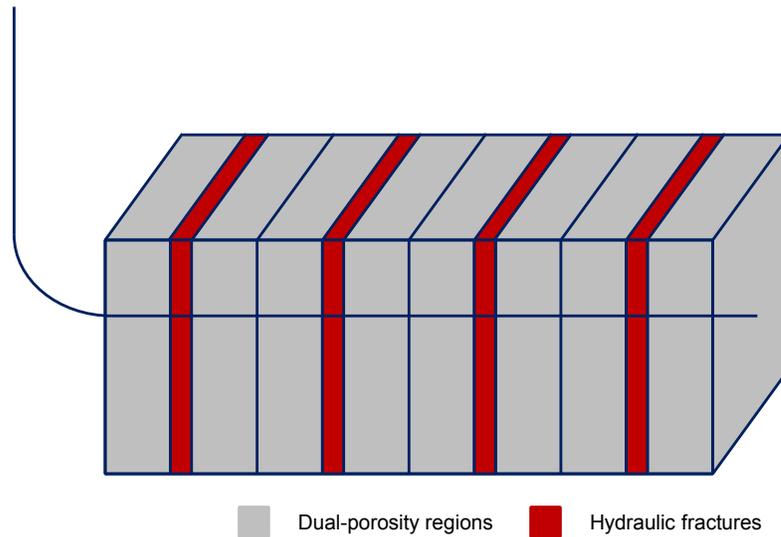
b) Application of dual porosity model for multiple transverse hydraulic fractured well (after Medeiros et al. (2008))

Fig. 3.3 Example of dual-porosity model for multiple transverse fractured horizontal well
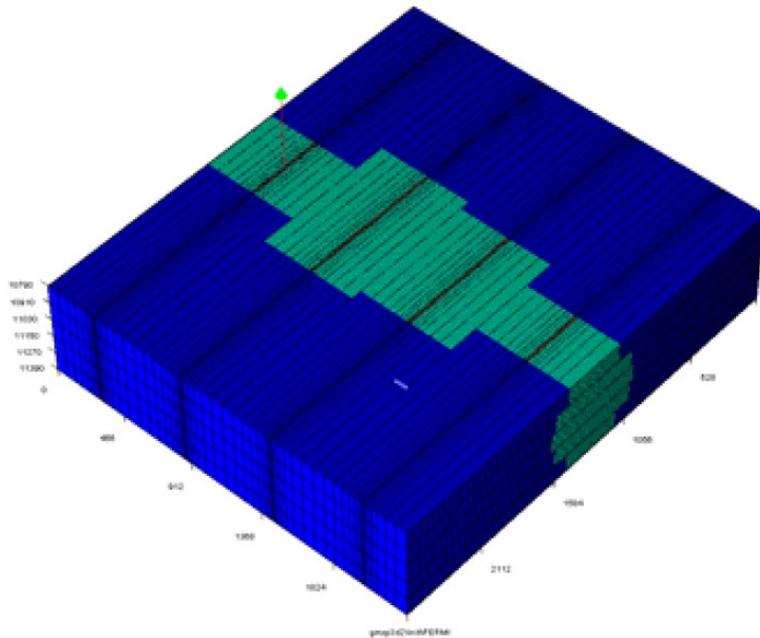
Fig. 3.4 Example of enhanced permeability area model for multiple transverse fractured horizontal well (Yin et al., 2011)

In the schematic, all of the fractures are assumed to have same fracture half-length and fracture permeability, but, in reality, these are different at each location and depend also on the stimulation treatment. These differences of the geometrical properties such as fracture half-length, fracture height, fracture permeability and its porosity are expressed as the grid size or the parameter values assigned to each reservoir grid in the simulation. These treatments are seen in the next section which gives some synthetic examples for the temperature estimation inside horizontal well.
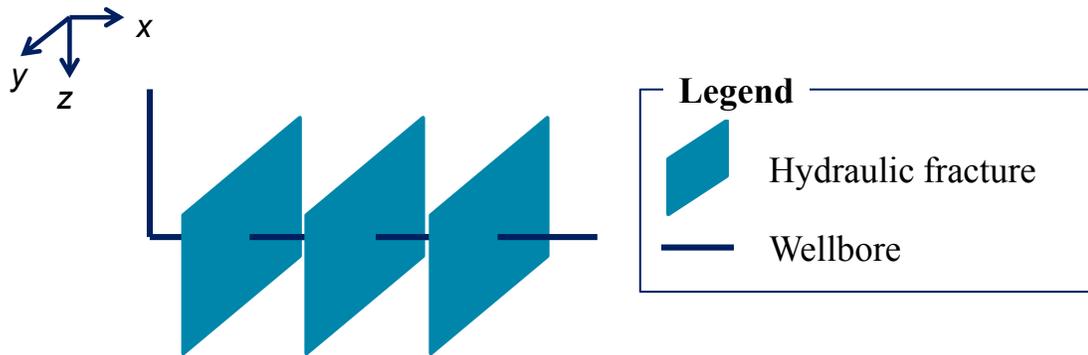
a) Example geometry of horizontal well with three fractures/clusters
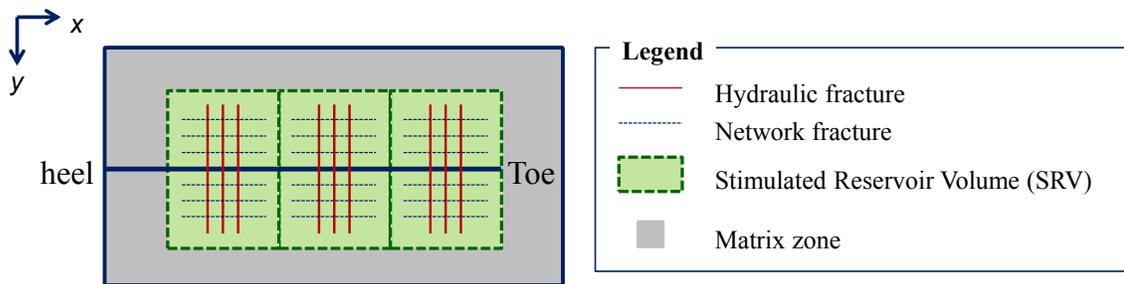
b) Cross-section along the horizontal well

Fig. 3.5 Schematics of reservoir/wellbore geometries (example)
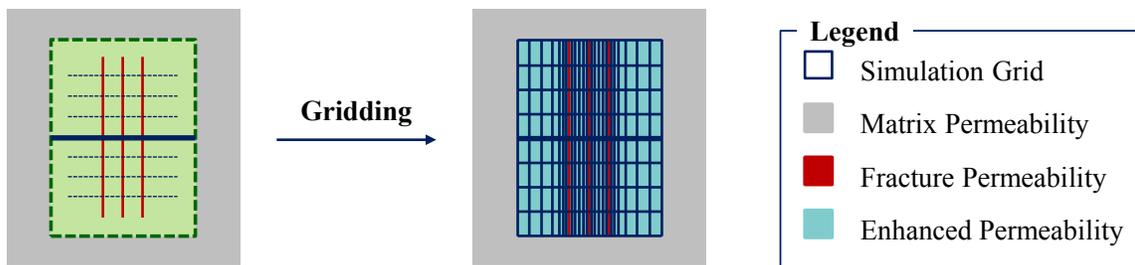
Fig. 3.6 Simulation gridding using enhanced permeability area

3.3 SYNTHETIC STUDIES

In this section, based on the modeling design described in previous section and the temperature model presented in previous chapter, synthetic examples are presented to see the temperature behavior of a well with multiple transverse hydraulic fractures in ultra-tight gas reservoir. In order to examine the effect by the fracture parameters, we resent two cases: homogeneous fractures and heterogeneous fractures. In homogeneous fractures case, each fracture has the same fracture parameters such as fracture conductivity and fracture half-length. On the other hand, in heterogeneous fractures case, each fracture has the different values on each parameter.

3.3.1 INPUT DATA

In order to obtain wellbore temperature distribution, reservoir temperatures and arriving temperatures are computed using reservoir flow/thermal simulation. In this subsection, wellbore and reservoir geometrical properties, fluid/thermal properties and rock properties are specified for the simulation.

Reservoir geometrical properties

The reservoir shape is assumed to be the "box-shaped" rectangular, and the other reservoir parameters are set according to the work done by Meyer et al. (2010). The reservoir geometrical properties are summarized in **Table 3-1**. Here, the drainage area and the reservoir thickness presented by literatures (Bazan et al., 2010; Guo et al., 2012; Meyer et al., 2010) are used, and the reservoir length and width are estimated based on these values.

TABLE 3-1 RESERVOIR GEOMETRICAL PROPERTIES		
Parameter	Description	Value [unit]
-	Reservoir Shape	Rectangular
L	Reservoir Length	5500 [ft]
h	Reservoir Thickness	300 [ft]
-	Drainage Area	80 [acre]
w	Reservoir width	635 [ft]

Wellbore geometrical properties & completion designs

Wellbore geometrical properties are given based on several literatures such as Bazan et al. (2010) and Yoshioka et al. (2007). The overall heat transfer coefficient is assumed to be constant and is estimated by Eq. 2.91. These properties are summarized in **Table 3-2**.

TABLE 3-2 WELLBORE GEOMETRICAL PROPERTIES		
Parameter	Description	Value [unit]
L	Lateral length	5000 [ft]
d_w	Wellbore diameter (OD)	8.75 [inch]
$d_{c,OD}$	Casing Diameter (OD)	5.5 [inch]
$d_{c,ID}$	Casing Diameter (ID)	4.670 [inch]
ε	Wellbore roughness	0.01
K_{casing}	Thermal conductivity (casing)	6.933 [Btu/hr-ft-F]
K_{cement}	Thermal conductivity (cement)	4.021 [Btu/hr-ft-F]
U	Overall heat transfer coefficient	32.902 [BTU/hr-ft^2-F]

Fluid properties

In order to determine the fluid properties, temperature and pressure in the reservoir should be specified. In **Table 3-3**, the initial reservoir pressure, reservoir temperature and geothermal temperature gradient used in these examples are summarized.

48

TABLE 3-3 PRESSURE AND TEMPERATURE DATA		
Parameter	Description	Value [unit]
p_{res}	Initial reservoir pressure	5,000 [psia]
$T_{R,ini}$	Initial reservoir temperature	237 [F]
T_G	Geothermal Temperature Gradient	0.0202 [F/ft]

The fluid and thermal properties of gas is summarized in **Fig. 3.7**. These properties are estimated using non-isothermal fluid and thermal property correlations presented in Appendix C.

Rock properties

Rock properties are approximated based on the data presented by relevant literatures (Bazan et al., 2010; Lake, 2010; Li and Zhu, 2010). The rock properties used in this work are summarized in the **Table 3-4**.

TABLE 3-4 ROCK PROPERTIES		
Parameter	Description	Value [unit]
ρ_R	Matrix Density	148.58 [lbf/ft^3]
ϕ	Matrix porosity (HC porosity)	5.0 [%]
k_T	Thermal Conductivity	2.0 [Btu/hr-ft-F]
c_{pR}	Rock Heat Capacity	0.202 [Btu/lbm F]
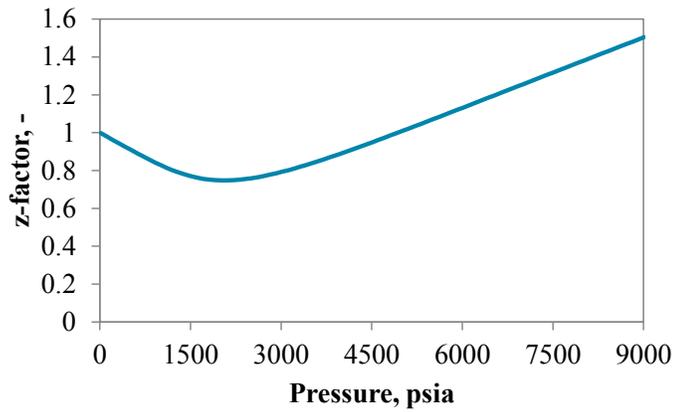
Z-factor
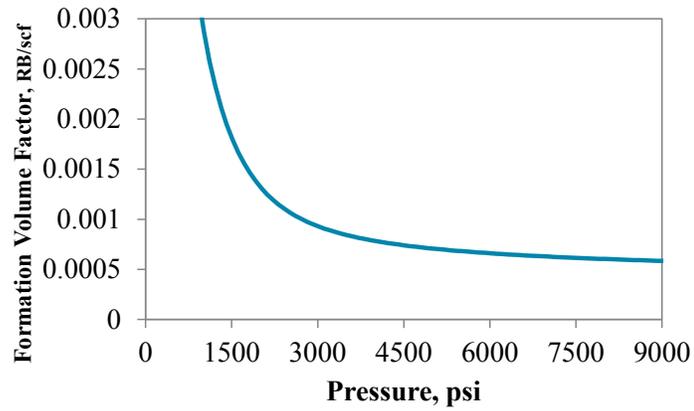
Gas formation volume factor
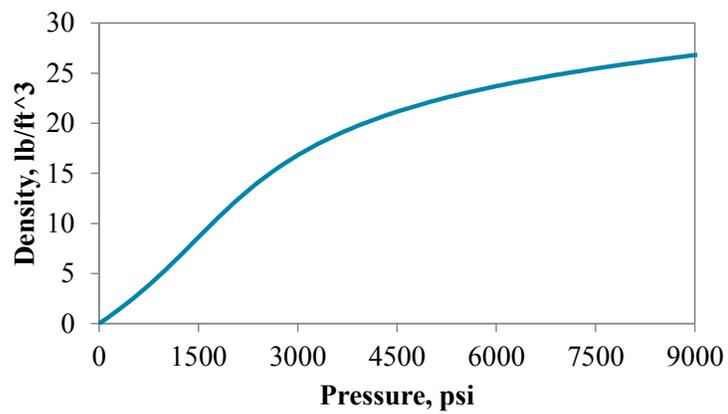
Gas density

a) Gas properties (z-factor, formation volume factor and density)
Fig. 3.7 Gas properties
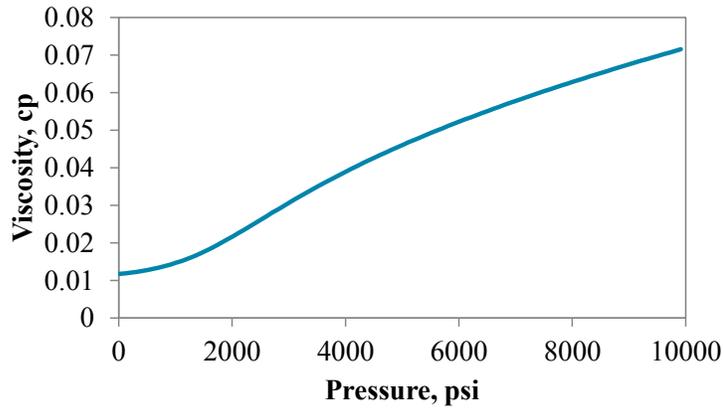
Gas viscosity
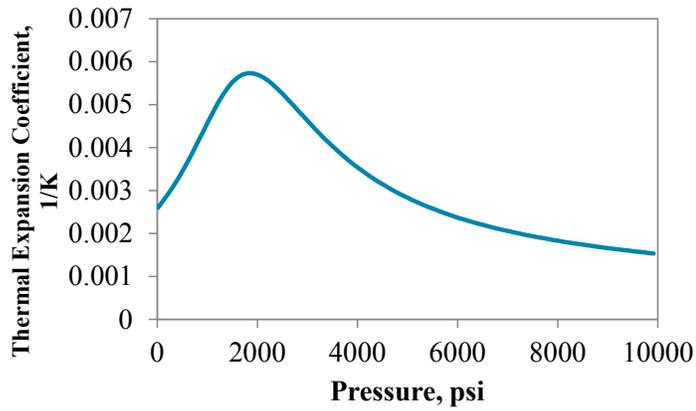
Gas thermal expansion coefficient
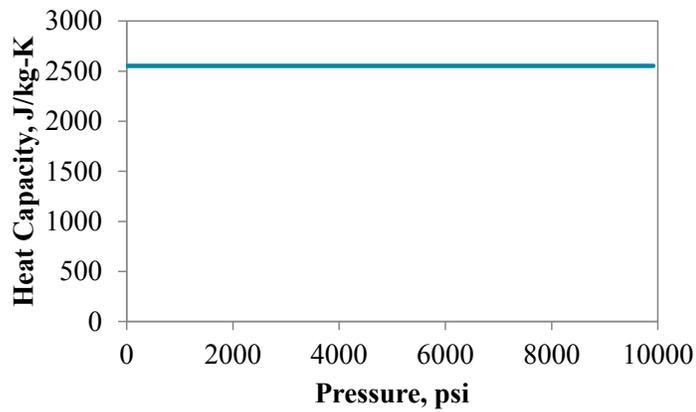
Gas heat capacity

b) Gas properties (viscosity, thermal expansion coefficient, heat capacity)
Fig. 3.7 Continued

51

3.3.2 SYNTHETIC EXAMPLES

In this subsection, we examine temperature behavior along the horizontal well with multiple transverse hydraulic fractures using two synthetic examples. We recall that these are homogeneous fractures (each fracture has the same fracture properties) case and heterogeneous fractures case (each fracture has the different fracture properties). For each case, it is assumed that there are five transverse fractures along the perfectly horizontal well. The flowing fluid is single phase gas and the well is producing at constant surface production rate (1.6 MMscf/day) for 30 days. The base fracture properties are summarized in the **Table 3-5**. For the homogeneous fractures case, these values are used for each fracture properties. On the other hand, for heterogeneous fractures case, these properties are multiplied by a specified multiplier for each fracture to express the heterogeneity. In this work, we used 0.56, 1.15, 1.00, 1.54 and 0.23 as the multipliers corresponding to the fractures location from heel to toe. **Fig. 3.8** shows the schematics of reservoir geometry and cross-sections of homogeneous case and heterogeneous cases.

| TABLE 3-5 BASE FRACTURE PARAMETERS	
Parameter	Value [unit]
Matrix Permeability	1.50×10^{-4} [md]
Enhanced Permeability	0.060 [md]
Fracture permeability	400 [md]
Matrix Porosity	0.08 [-]
Enhanced Porosity	0.081 [-]
Fracture Porosity	0.32 [-]
Fracture Half Length	150 [ft]
Fracture Height	260 [ft]
Fracture Conductivity	40 [ft-md]

Reservoir geometry

Fig. 3.8 Schematics of reservoir and fracture geometries for synthetic examples

CASE1: Homogeneous fractures

At first, we run the simulation for the homogeneous fractures case using the given parameters, and results are shown in **Fig. 3.9 through Fig. 3.11**. These figures are the wellbore and arriving temperatures, the wellbore and wellbore grid pressures and inflow distribution along the horizontal well, respectively. According to Eq. 2.101, wellbore temperature depends on the three components: Joule Thomson effect inside wellbore due to the pressure change, heat transfer between wellbore and formation and potential effect. Because the well trajectory is assumed to be perfectly horizontal, we ignore the effect of potential term. According to Fig. 3.10, the Joule Thomson effect inside wellbore is very small because the pressure change inside wellbore is subtle. Then, the temperature difference between wellbore and reservoir inflow has the dominant role for the wellbore temperature behavior. The arriving temperature shows clear temperature decrease at the fracture location (perforated zone) because it is not affected by the fluid mixing effect between the reservoir inflow and wellbore flowing fluid. From Fig. 3.11, as the flowing fluid inside wellbore increases, the temperature change caused by reservoir inflow is getting smaller even if the reservoir inflow is the same at each fracture location because of the mixing effect.
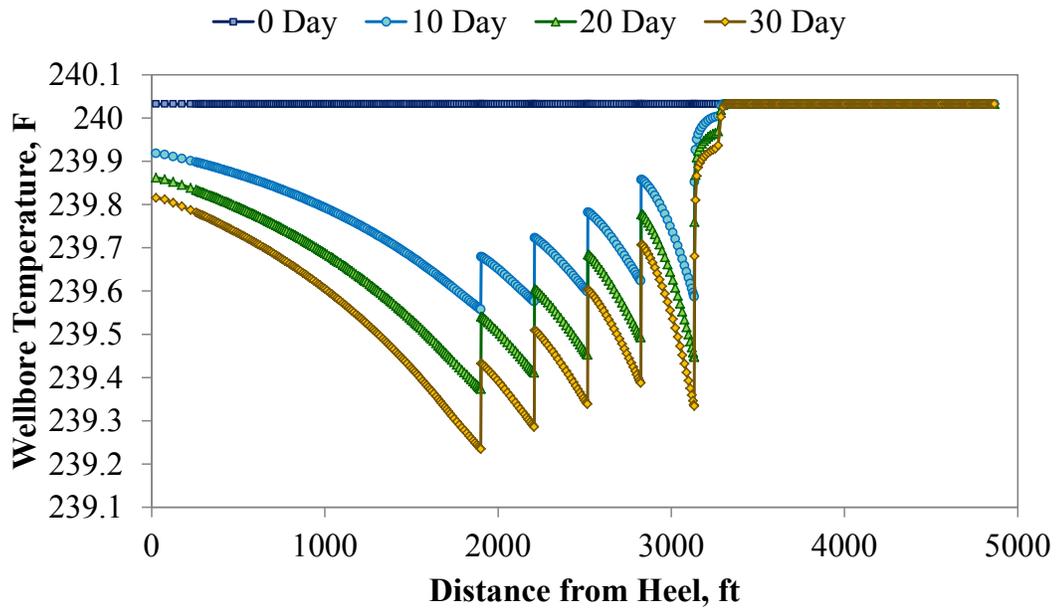
Inside wellbore
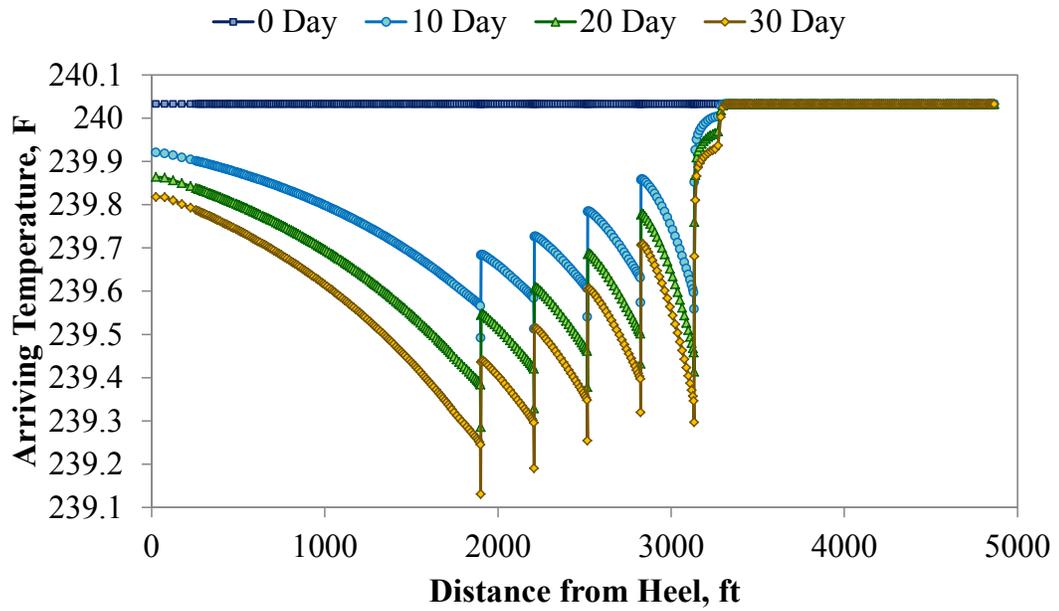
Arriving temperture (just outside of wellbore)

**Fig. 3.9 Temperature distribution (homogeneous fractures with network)**
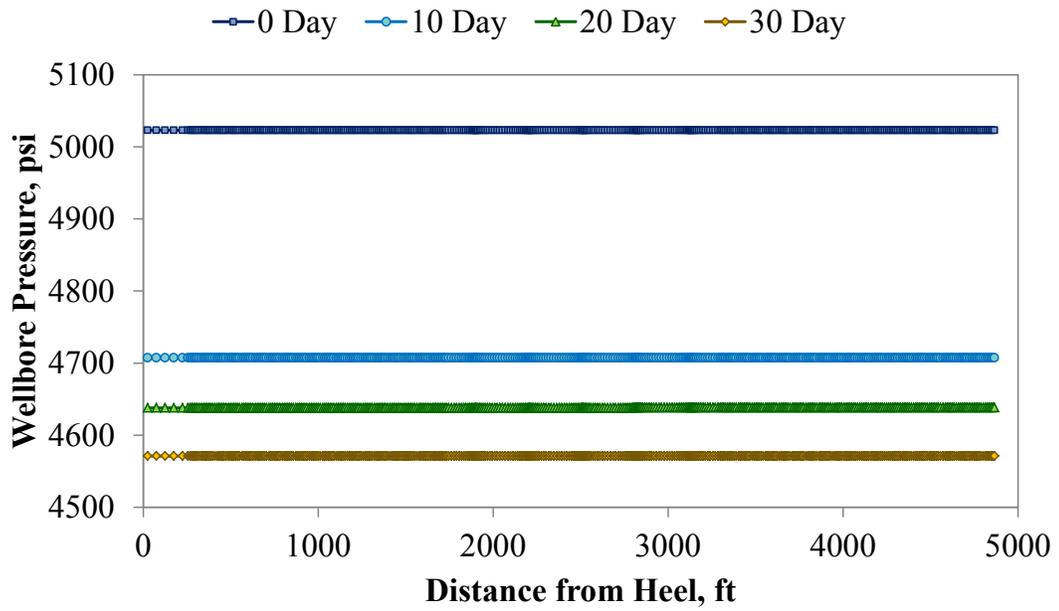
Inside wellbore
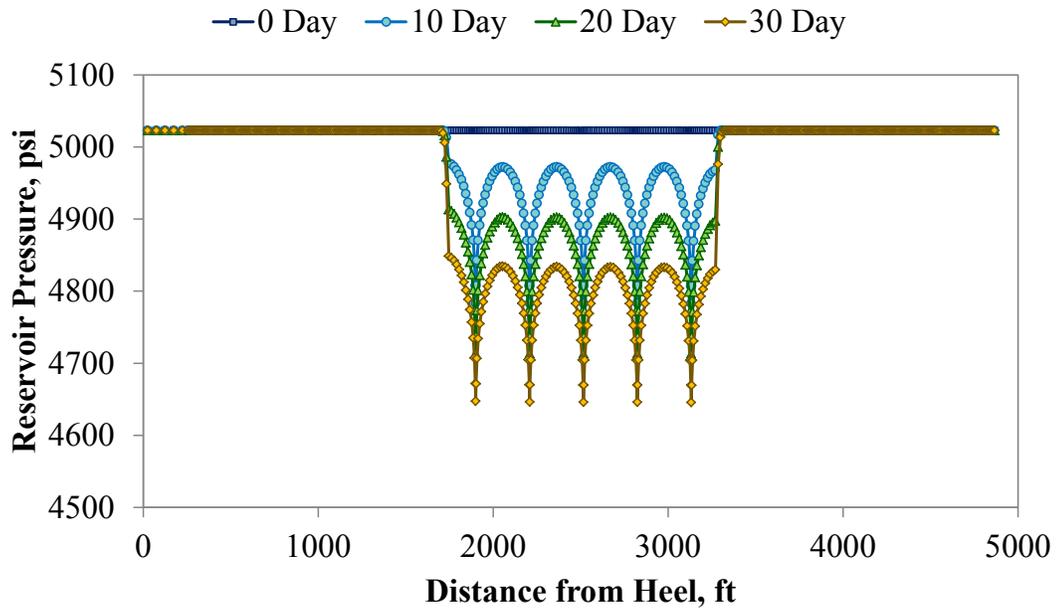
Reservoir grid which containts wellbore

Fig. 3.10 Pressure distribution (homogeneous fractures with network)
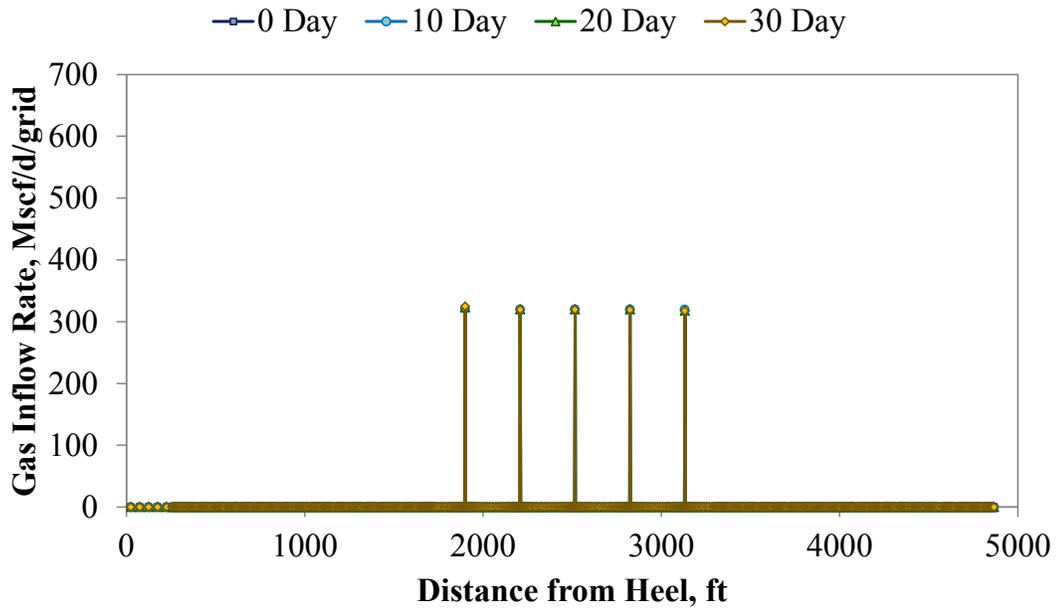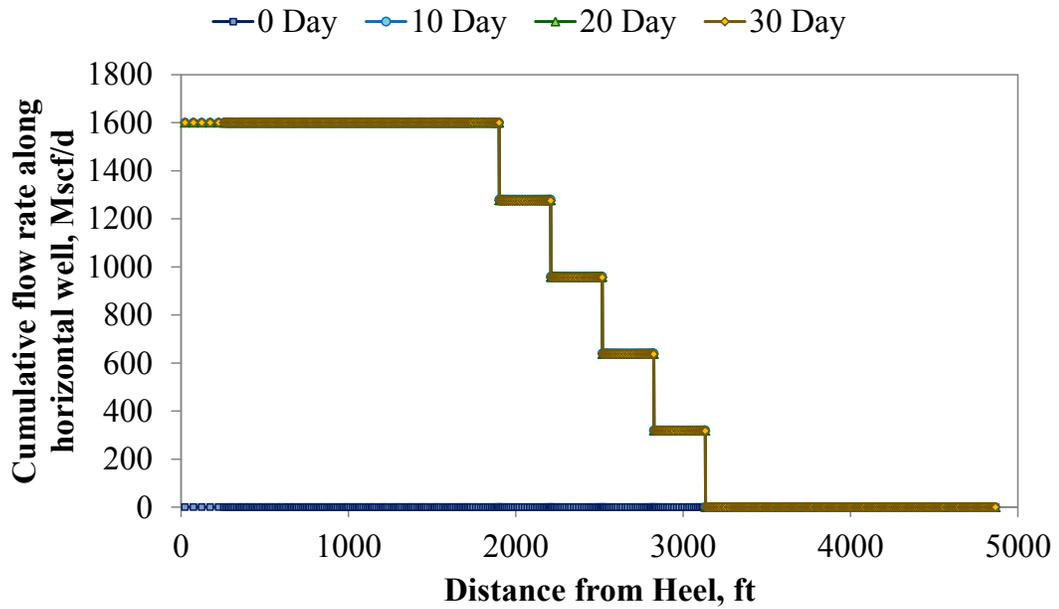
Inflow rate

Cumulative flow rate

Fig. 3.11 Inflow/cumulative flow rate distribution

**(homogeneous fractures with network)**

57

In this synthetic example, because of the gas expansion effect near the wellbore, especially inside fracture, the temperature of reservoir inflow is cooler than that of the wellbore inside flow. It causes the wellbore temperature decrease at the fracture location. On the other hand, at the non-perforated zone of the well, because of no reservoir inflow, the wellbore fluid cooled at fracture location is heated up by higher temperature formation. This process is repeated from the first perforation to the last perforation, and in the non-perforated zone near the heel, the wellbore temperature is heated up by formation.

In addition to this cooling-heating cycle, we can see that the network fracture affects the temperature behavior inside wellbore. Because the change of reservoir pressure in the enhanced permeability region is larger than that in the matrix region, gas expansion cooling effect occurs in this region also. **Fig. 3.12** shows the pressure and temperature distribution near the wellbore after 30 days production. In this case, the reservoir temperature decreases corresponding to the pressure drop in the enhanced permeability region, and this trend should be different when fluid property and reservoir condition (e.g. temperature and pressure) is different.

Comparing the reservoir temperature distribution to the reservoir pressure distribution, we can see the reservoir temperature changes along the horizontal well. This is caused by the heat transfer between the wellbore and the reservoir grid which contains the wellbore segment, which is controlled by the sink/source term in the reservoir thermal model. In this case, because the wellbore temperature is less than the reservoir grid temperature, the reservoir temperature along the horizontal well becomes lower.
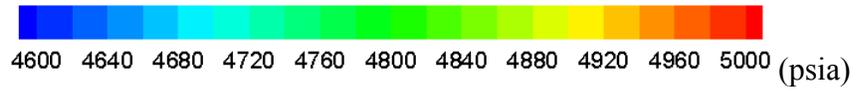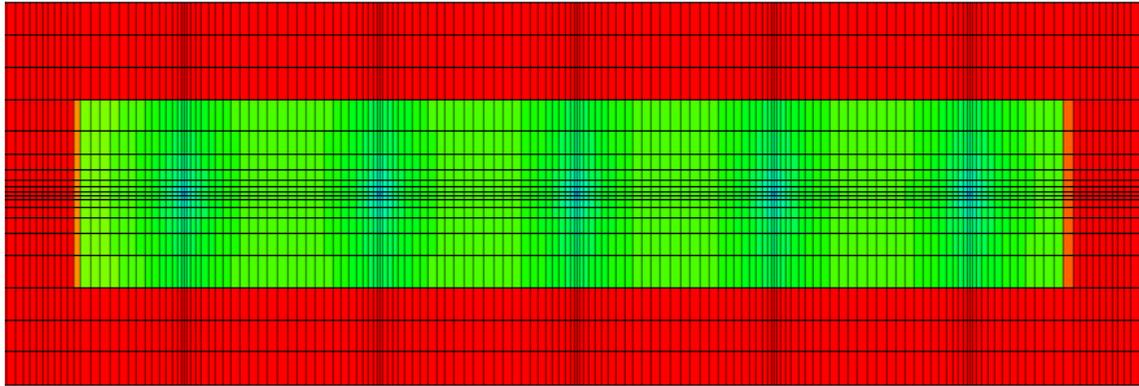
Reservoir pressure field (Cross-section along the horizontal well) – 30 days
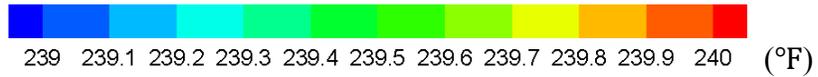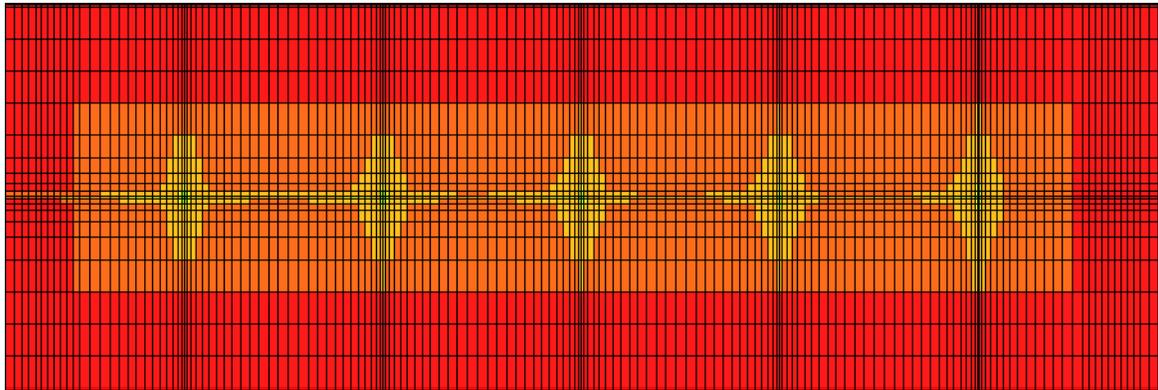
Reservoir temperature field (Cross-section along the horizontal well) – 30 days

Fig. 3.12 Pressure and temperature distirubiton in the enhanced permeability area

CASE2: Heterogeneous fractures

Next, we run the simulation for the heterogeneous fractures case using the given parameters and multipliers. The results are shown in **Fig. 3.13 through Fig. 3.15** which are the wellbore and arriving temperature, the wellbore and wellbore grid pressure and inflow distribution along the horizontal well, respectively. As we saw in the homogeneous case, heterogeneous case gives the same trend of the cooling-heating cycles in the wellbore and reservoir inflow temperature behavior. However, because of the heterogeneity of fractures, the temperature trend looks different from that given by homogenous fractures case.

According to Fig. 3.15, the fracture heterogeneity corresponds to the inflow distribution along the horizontal well. The higher inflow rate is corresponding to the larger temperature change from the reservoir arriving temperature distribution shown in Fig. 3.13. In principle, the wellbore temperature change near the toe should be larger than that near the heel because the temperature mixing effect is smaller due to the smaller amount of flowing fluid inside wellbore. For this case, however, the temperature change near the toe is not so large because the poor fracture parameter leads to the subtle temperature change due to the much smaller amount of reservoir inflow at the location.

Fig. 3.16 shows the reservoir pressure and temperature distribution near the horizontal well in order to see the stimulated reservoir volume and temperature behavior in the region. The pressure front reaches the very low permeability formation in 30 days and we can see the effective drainage area, SRV, clearly. The temperature distribution has the same kind of trend with the pressure distribution.
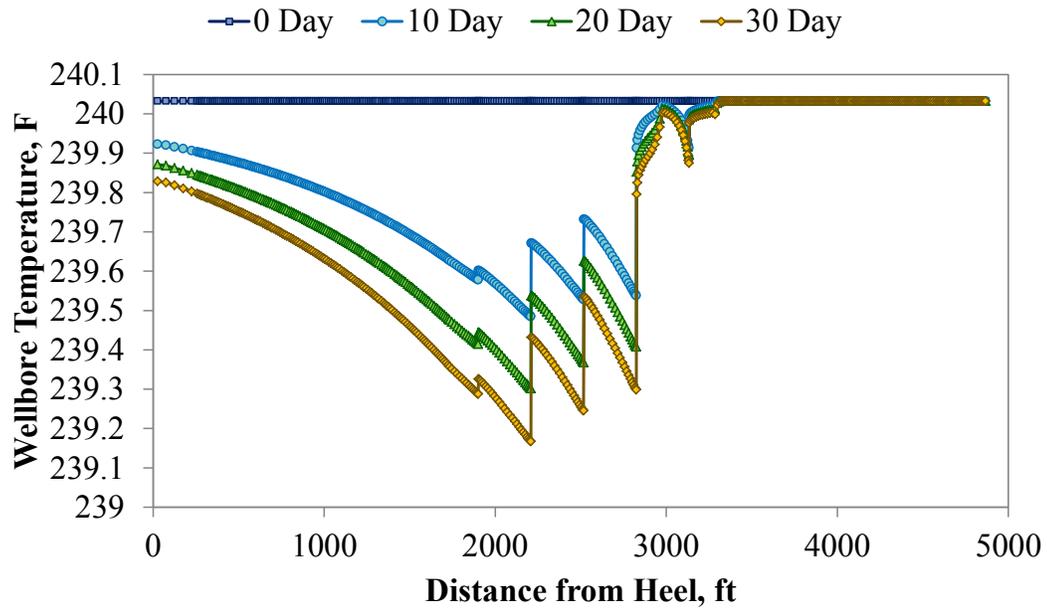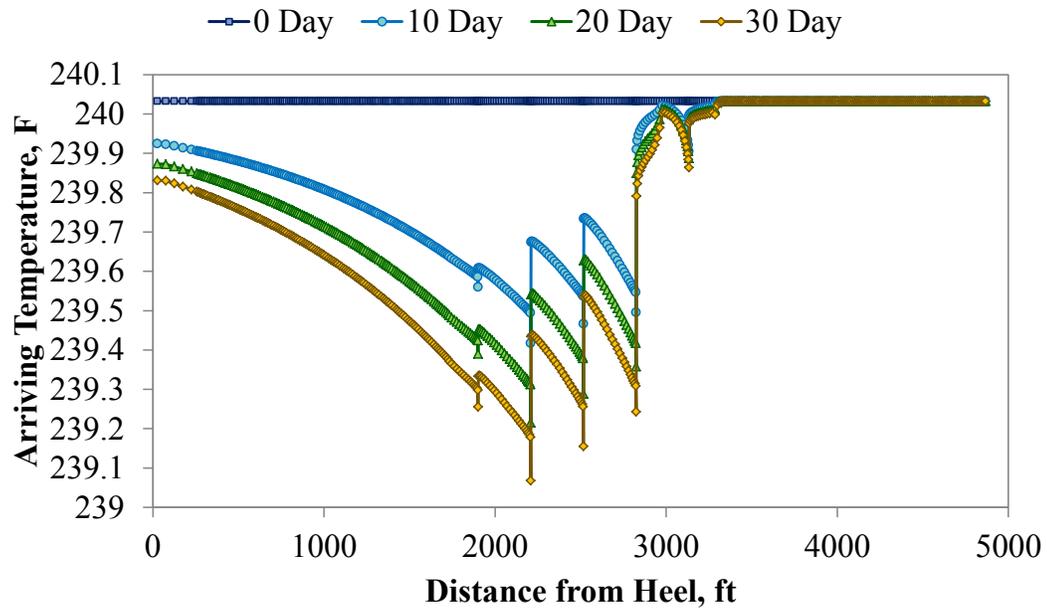
Inside wellbore

**Arriving temperture (just outside of wellbore)**

Fig. 3.13 Temperature distribution (heterogeneous fractures with network)
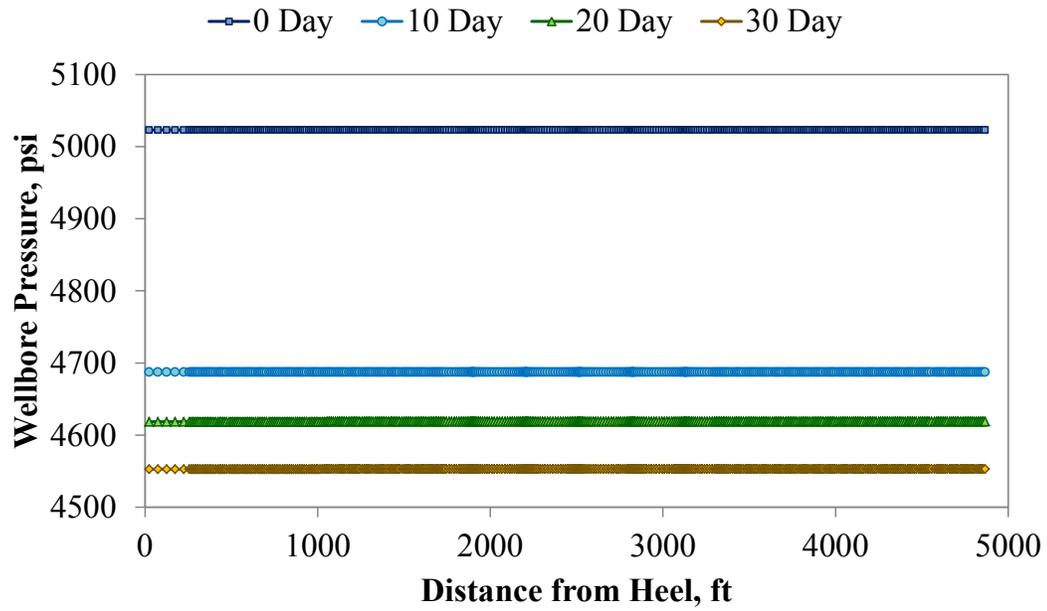
Inside wellbore
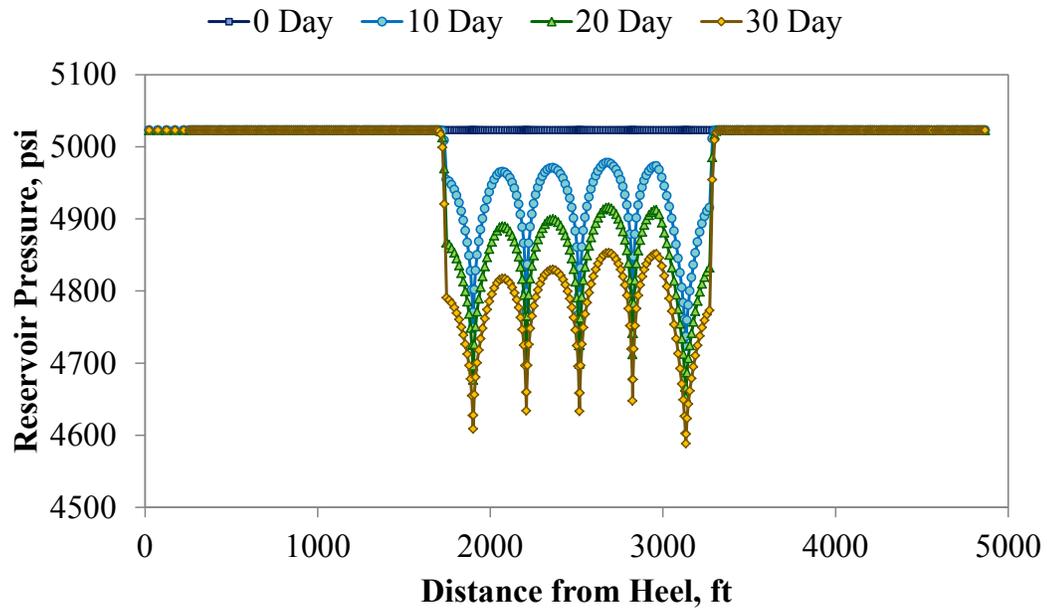
Reservoir grid which containts wellbore

Fig. 3.14 Pressure distribution (heterogeneous fractures with network)
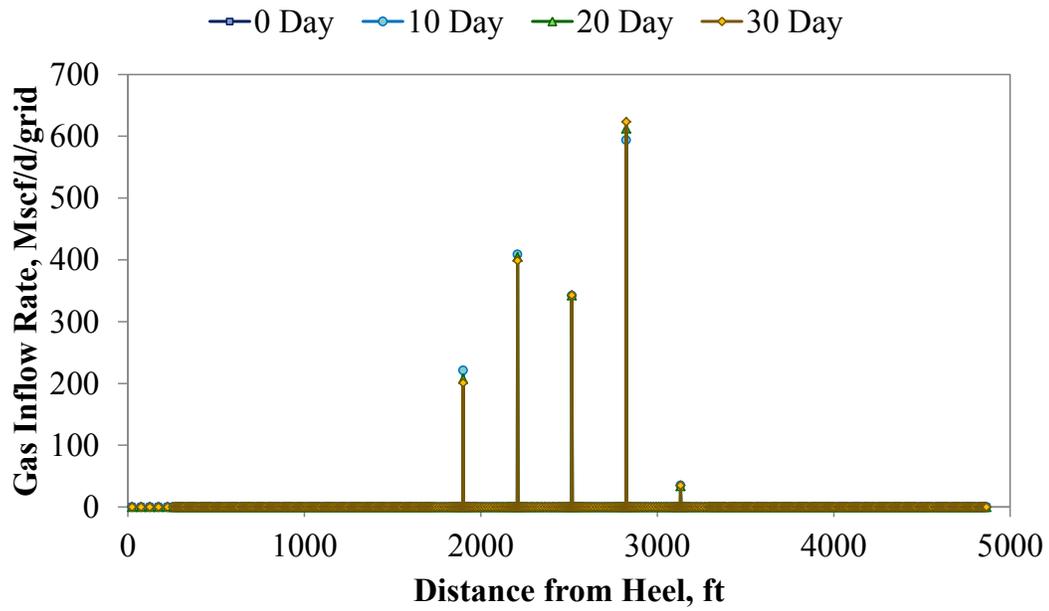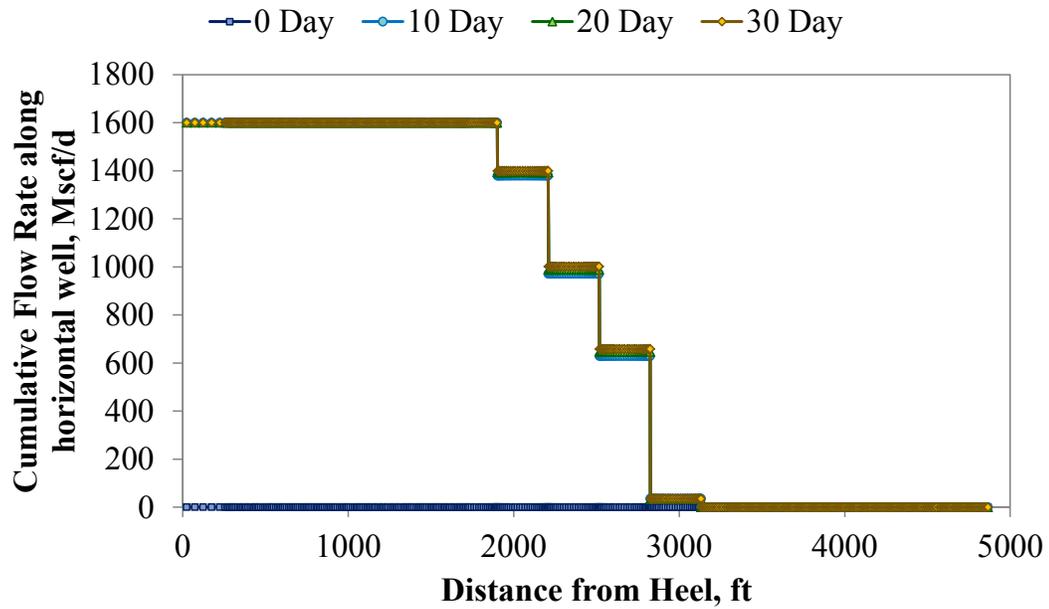
Inflow rate

Cumulative flow rate

Fig. 3.15 Inflow/cumulative flow rate distribution

(heterogeneous fractures with network)
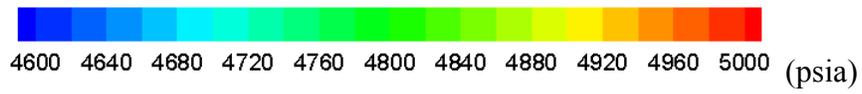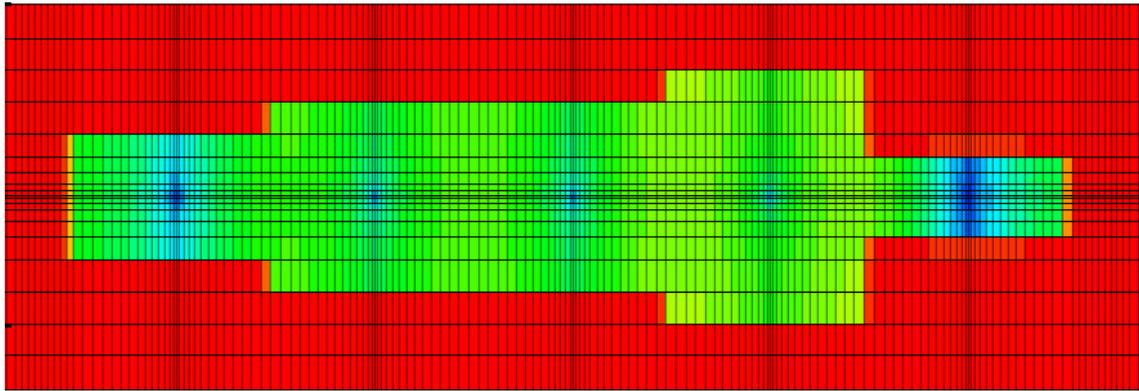
Reservoir pressure field (Cross-section along the horizontal well) – 30 days
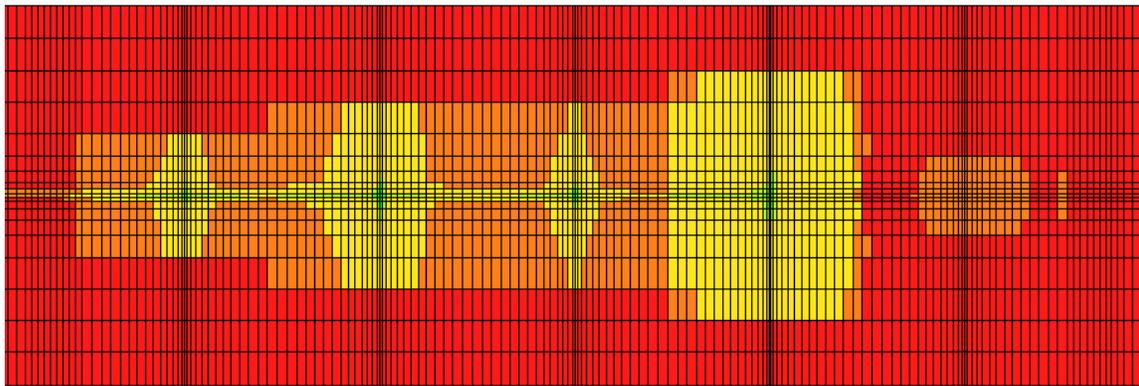
Reservoir temperature field (Cross-section along the horizontal well) – 30 days

Fig. 3.16 Pressure and temperature distirubiton in the enhanced permeability area

3.3.3 EFFECT OF NETWORK FRACTURES

In this subsection, the effect of the existence of network fractures is examined through the comparison study between the cases with and without network fractures. **Fig. 3.17** shows the conceptual schematics of the reservoir/wellbore geometry of the case without network fractures. In this case, there is no enhanced permeability area, and only the primary hydraulic fractures are created along the horizontal well. At first, we examine the effect of fracture network for homogeneous case and heterogeneous case incorporating the fracture heterogeneity effects under constant rate boundary condition. Next, the boundary condition effect is examined under constant BHP production only for the homogeneous fractures case.

Homogeneous fractures
(without network)

Heterogeneous fractures
(without network)
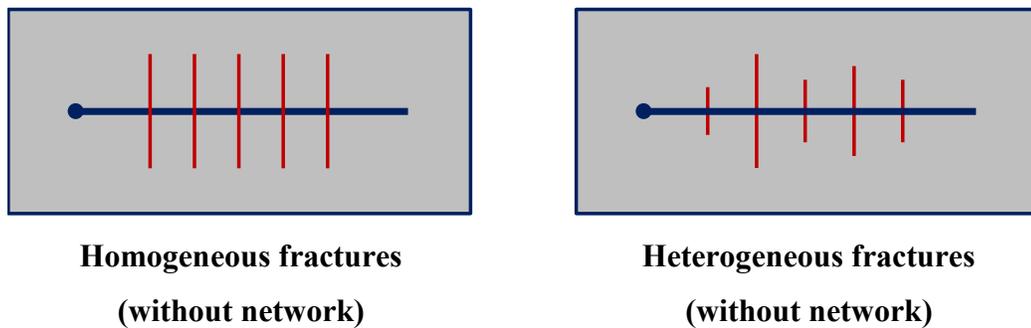
Fig. 3.17 Schematics of reservoir and fracture geometries for synthetic examples

Network fracture effect under constant rate production

Fig. 3.18 through Fig. 3.20 show the comparison results of the homogeneous fractures case for wellbore temperature, reservoir pressure along the horizontal well and the reservoir inflow distribution, respectively. In order to see the difference of the magnitude, the scale of the comparison plot is set to the same. According to Fig. 3.19, the reservoir inflow distribution for each case is the same, but there is no high permeable region in the vicinity of the fractures. This leads to the larger pressure drop when the fluid comes into the fractures for this case as it is shown in Fig. 3.18 (this pressure drop becomes smaller

if the fracture conductivity is higher value than that in this case). Finally, the magnitude of the wellbore temperature change without network fracture is larger than that with network fracture.

Fig. 3.21 gives the pressure and temperature distribution for the case without network fractures. The pressure and temperature front from one fracture does not reach the front by the next fracture, because the production time is only 30 days and it is short. For this case, the temperature distribution corresponds to the pressure distribution, and also we can see the reservoir temperature is cooled by the wellbore.

According to Fig. 3.12 and Fig. 3.21, we can see the effect of network structure region under constant rate boundary condition. Fig. 3.12 shows the temperature decrease in the enhanced permeability region, and it means the formation temperature at the reservoir and wellbore contact decreases too. However, Fig. 3.21 indicates only the temperature change happens at the fracture location and in the vicinity of the fractures only. In this work, we use the enhanced permeability zone and it is based on the upscaling of the network fracture region (Appendix D), but the detail structure of networks has potential to make the temperature distribution different from that is presented here. In addition, the network region changes the pressure distribution in the vicinity of the fractures. This leads to the temperature variation of the inflow to the wellbore.

For the calibration of the above discussion, we also run the simulation for heterogeneous case without network fractures. **Fig. 3.22 through Fig. 3.24** show the comparison plots, and they are wellbore temperature comparison, reservoir pressure comparison along the horizontal well and the inflow distribution comparison, respectively. In addition, **Fig. 3.25** shows the distribution of pressure and temperature in the reservoir. Fig. 3.22 shows the similar cooling-heating cycle can be seen, but the magnitude is much bigger than the case with network region as in the homogeneous fractures case. According to Fig. 3.23, the inflow distribution is almost same between the cases with and without network fracture. Therefore, the difference of the magnitude is caused by the pressure change at the reservoir and fracture contact.
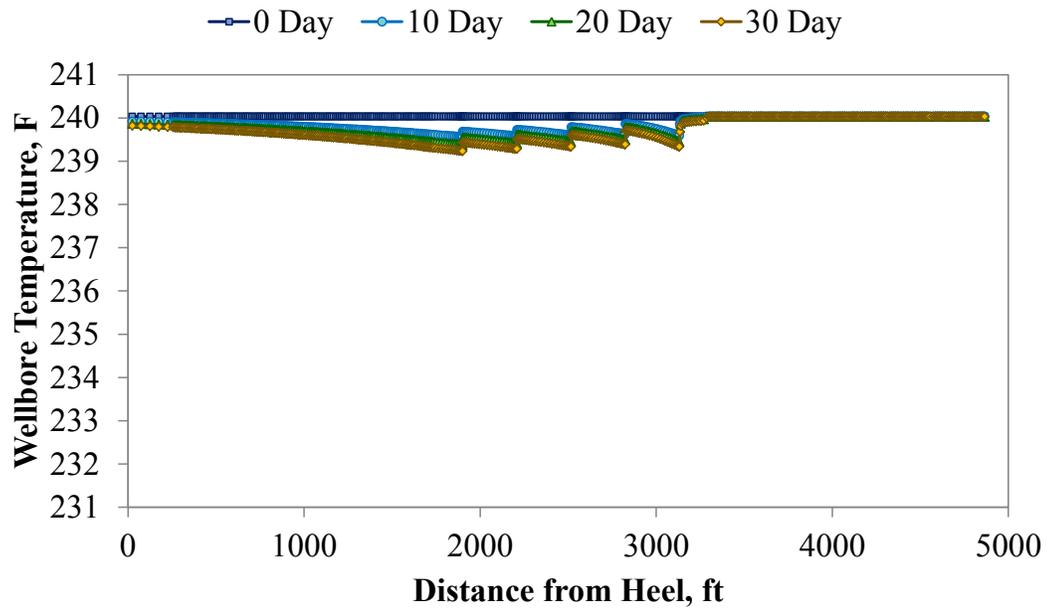
With network fractures
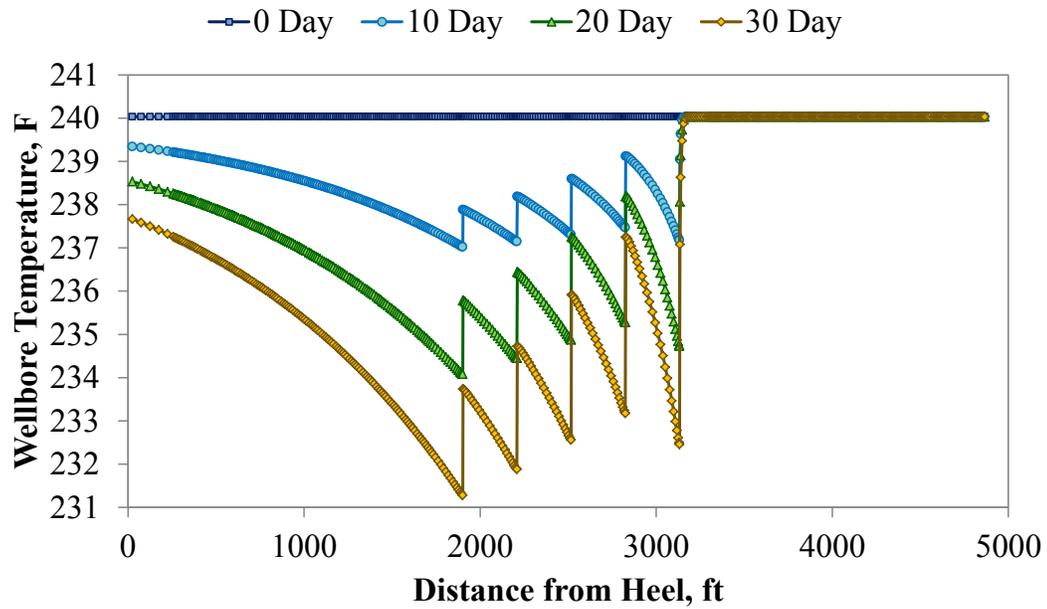
Without network fractures

Fig. 3.18 Comparison of wellbore temperture behavior with and without network fractures (homogeneous fractures case, constant rate)
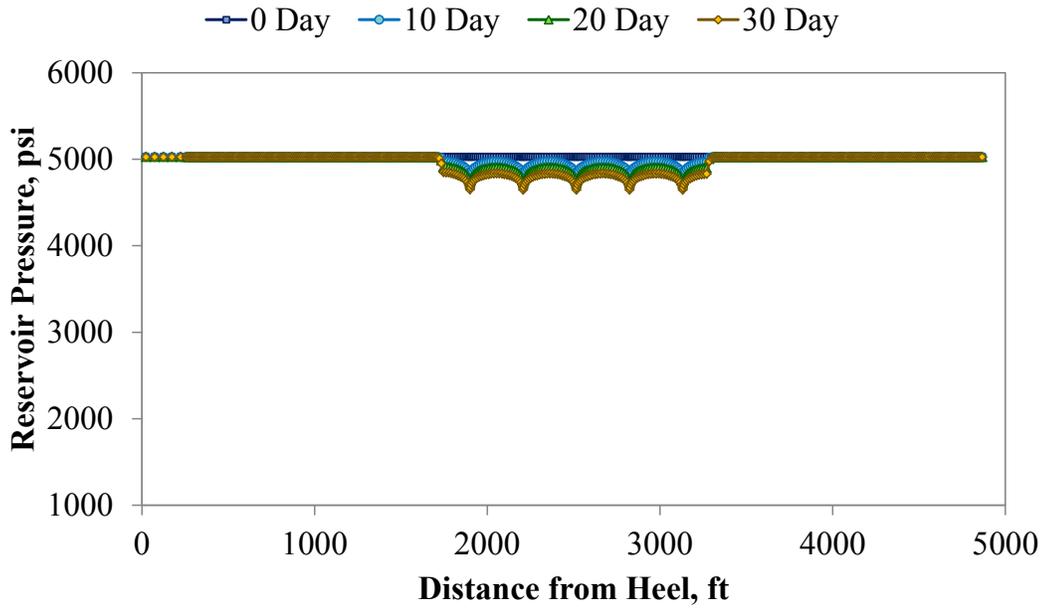
With network fractures
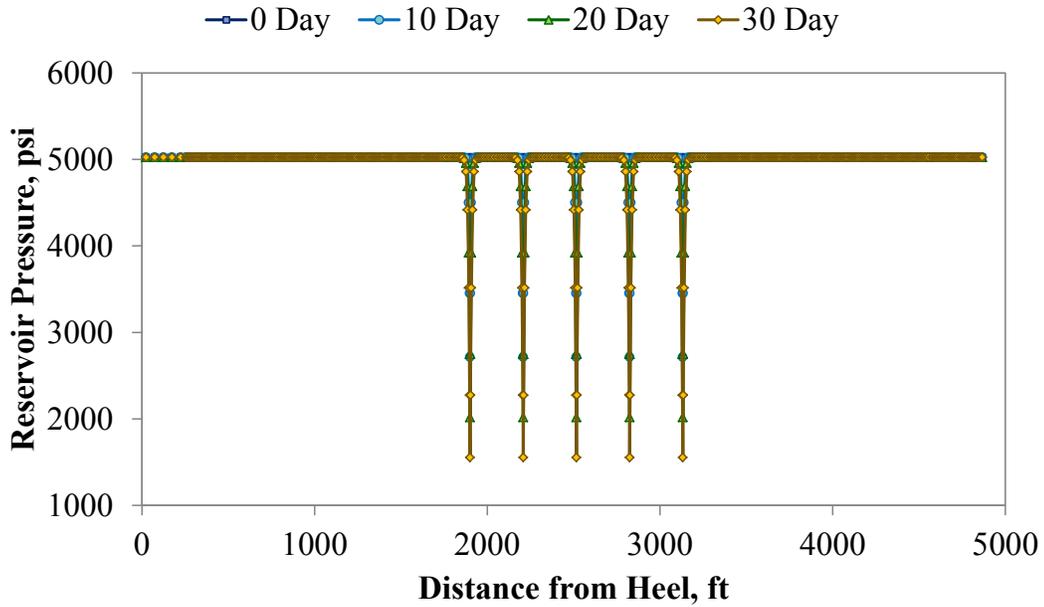
Without network fractures

Fig. 3.19 Comparison of reservoir pressure behavior with and without network fractures (homogeneous fractures case, constant rate)
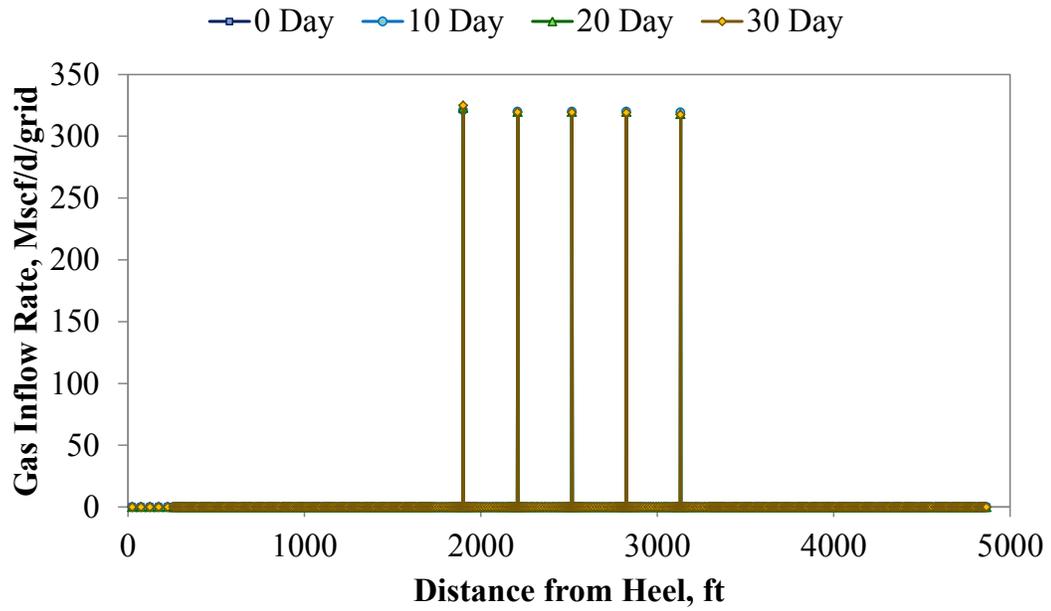
With network fractures
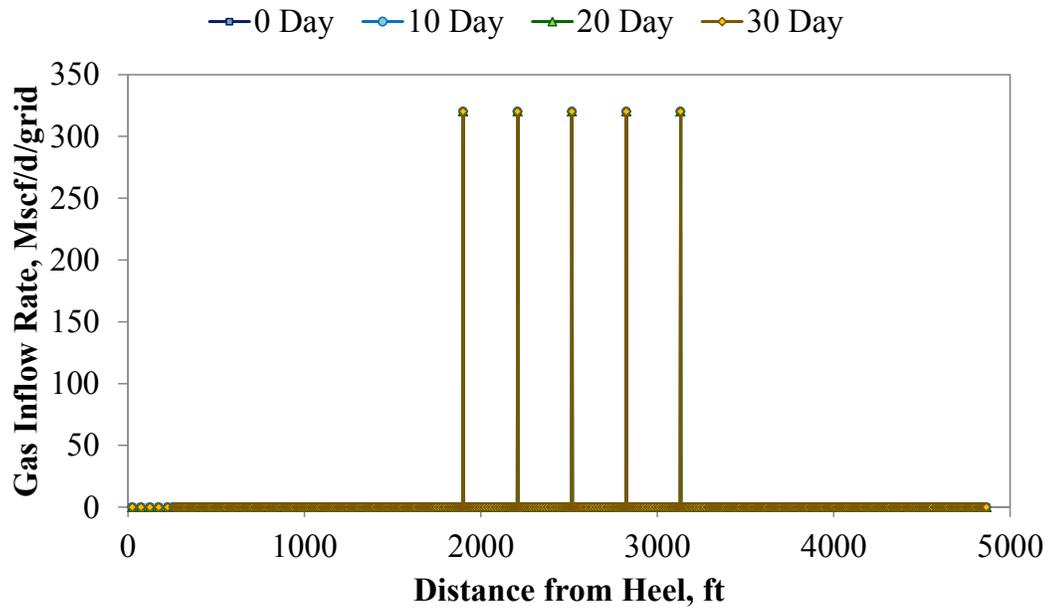
Without network fractures

Fig. 3.20 Comparison of reservoir inflow distribution with and without network fractures (homogeneous fractures case, constant rate)
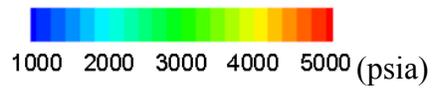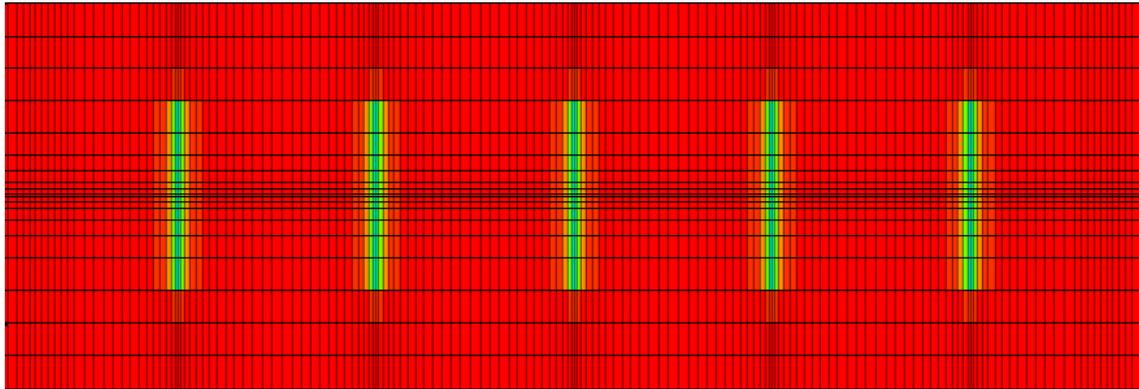
Reservoir pressure field (near wellbore) – 30 days
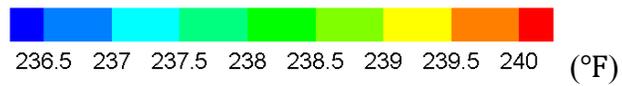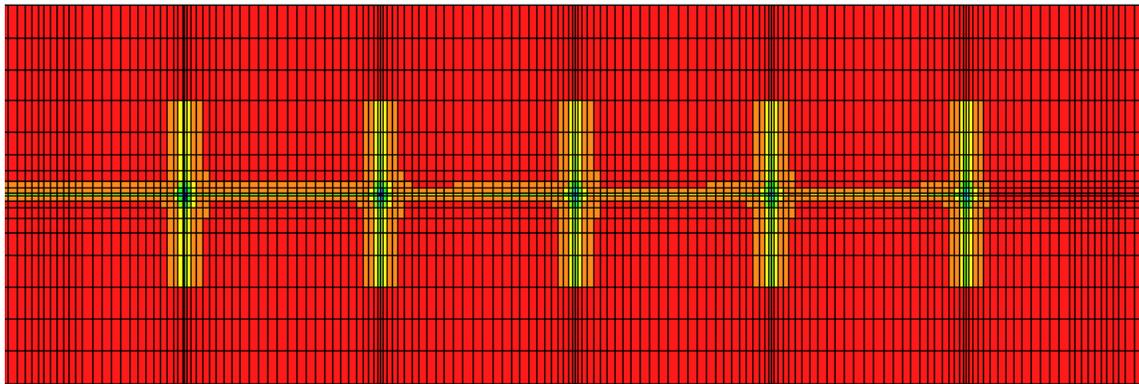
Reservoir temperature field (near wellbore) – 30 days

Fig. 3.21 Pressure and temperature distirubiton in the enhanced permeability area

(homogeneous case – without fracture network, constant rate)

In Fig. 3.22, we can see the temperature increase happens at the fracture nearest to heel. This is because the fluid temperature inside wellbore is cooler than the inflow temperature. In this case, three large fractures exist before the fracture, and they have a dominant role on the temperature behavior in the wellbore. The wellbore temperature is not enough to be heated by formation between the fractures, and finally the temperature increase happen.

Network fracture effect under constant BHP production

In this subsection, effects by a different boundary condition, constant BHP production is examined for the homogeneous fracture case. The simulations for the cases with fracture networks and without fracture networks are performed under the condition of $p_{wf} = 4000$ psia. **Fig. 3.26** shows the comparison results of temperature distributions, and we can see much larger temperature change for the case with network fractures comparing to the case without network fractures. This is opposite result given by the constant rate condition. **Fig. 3.27** is the comparison of the flow rate distribution along the horizontal well, and it shows the amount of wellbore flow of the case with network regions is much larger than that of the case without network region. This differences of the wellbore flow and corresponding reservoir inflow differences lead to the variation of temperature behavior as it is shown in Fig. 3.26.
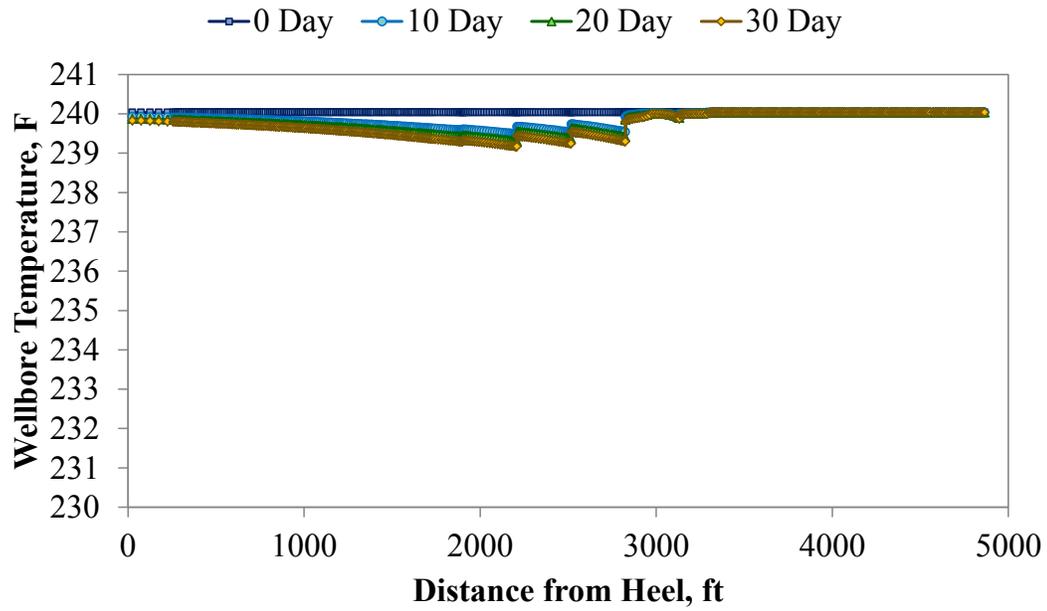
With network fractures
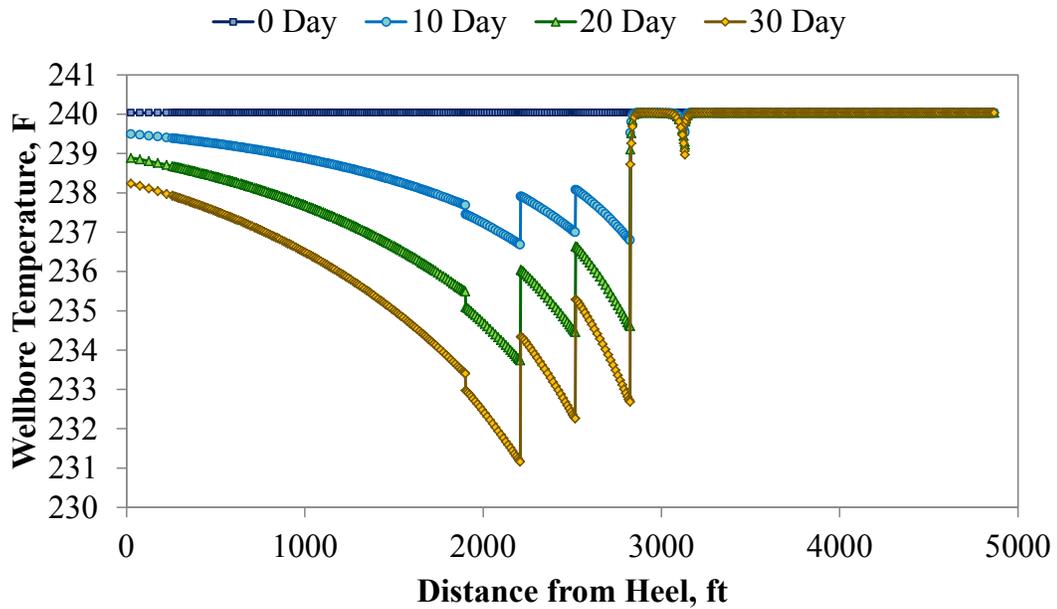
Without network fractures

Fig. 3.22 Comparison of wellbore temperture behavior with and without network fractures (heterogeneous fractures case, constant rate)

72
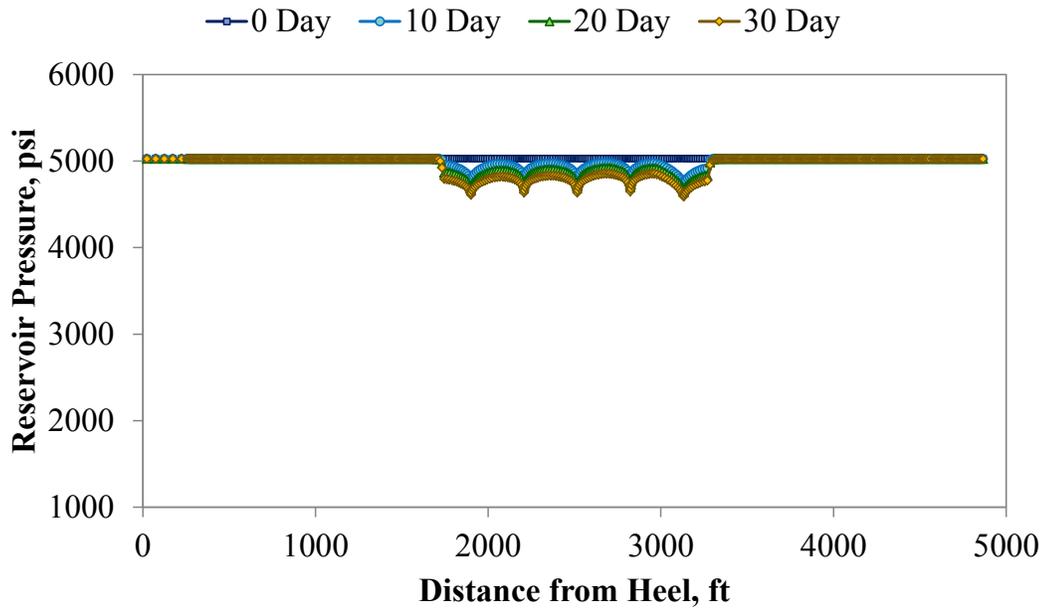
With network fractures
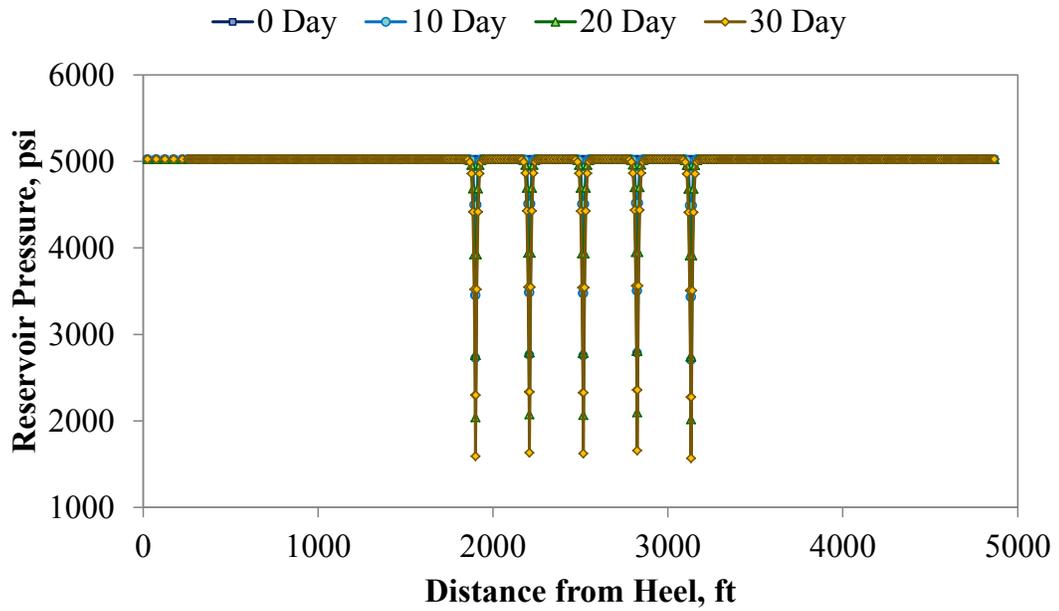
Without network fractures

Fig. 3.23 Comparison of reservoir pressure behavior with and without network fractures (heterogeneous fractures case, constant rate)
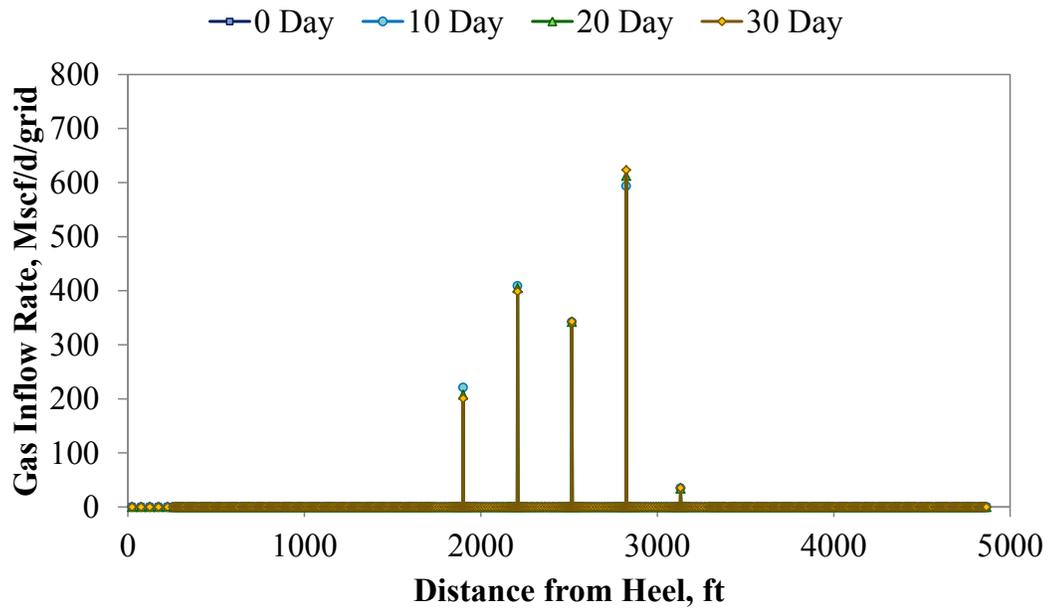
With network fractures
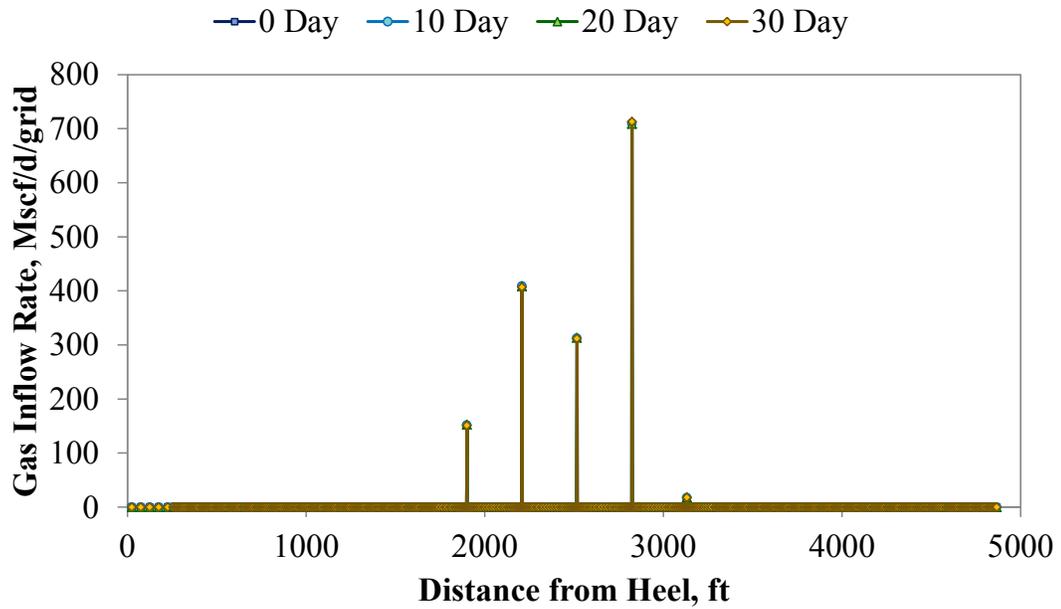
Without network fractures

Fig. 3.24 Comparison of reservoir inflow distribution with and without network fractures (heterogeneous fractures case, constant rate)
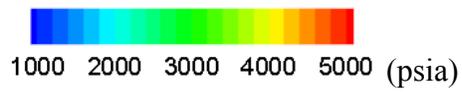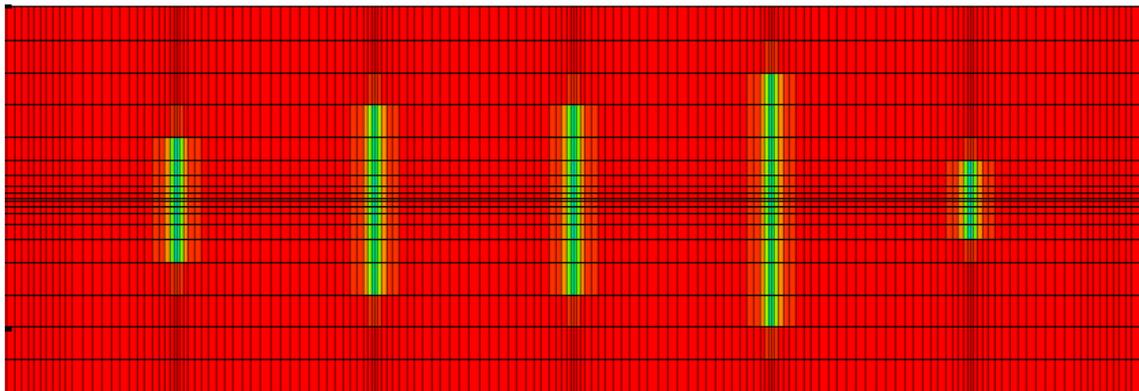
Reservoir pressure field (Cross-section along the horizontal well) – 30 days
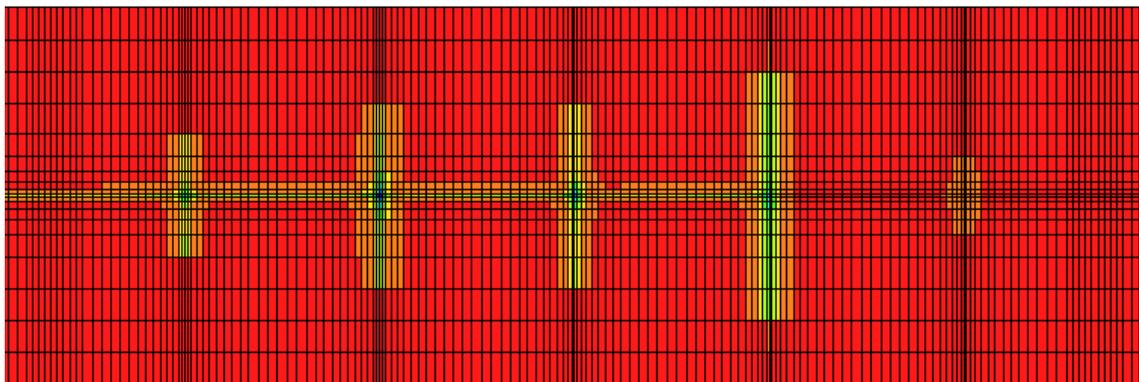
Reservoir temperature field (Cross-section along the horizontal well) – 30 days

Fig. 3.25 Pressure and temperature distirubiton in the enhanced permeability area

(heterogeneous case – without fracture network, constant rate)
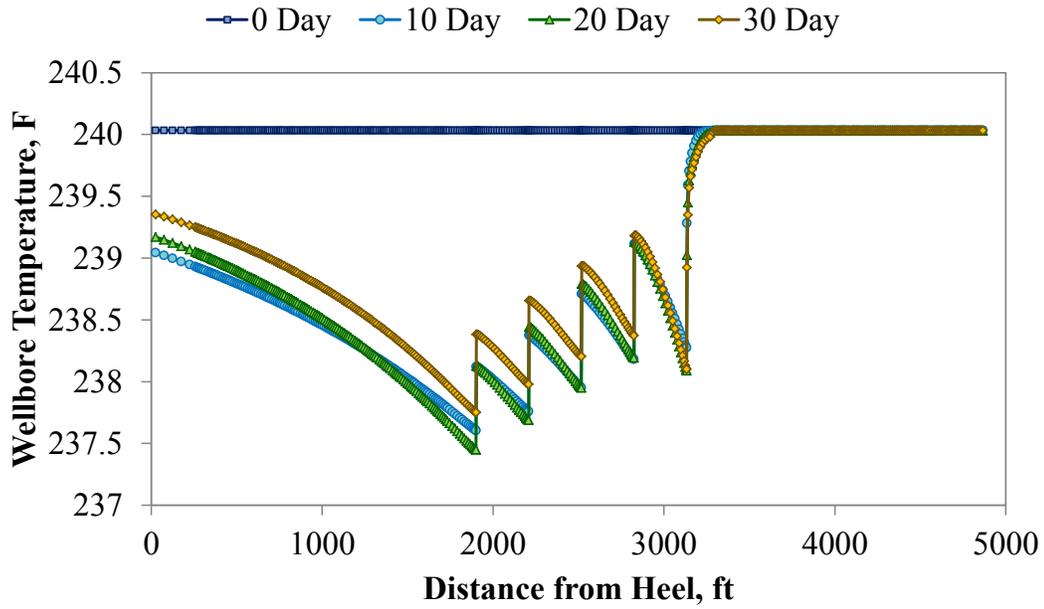
With network fractures
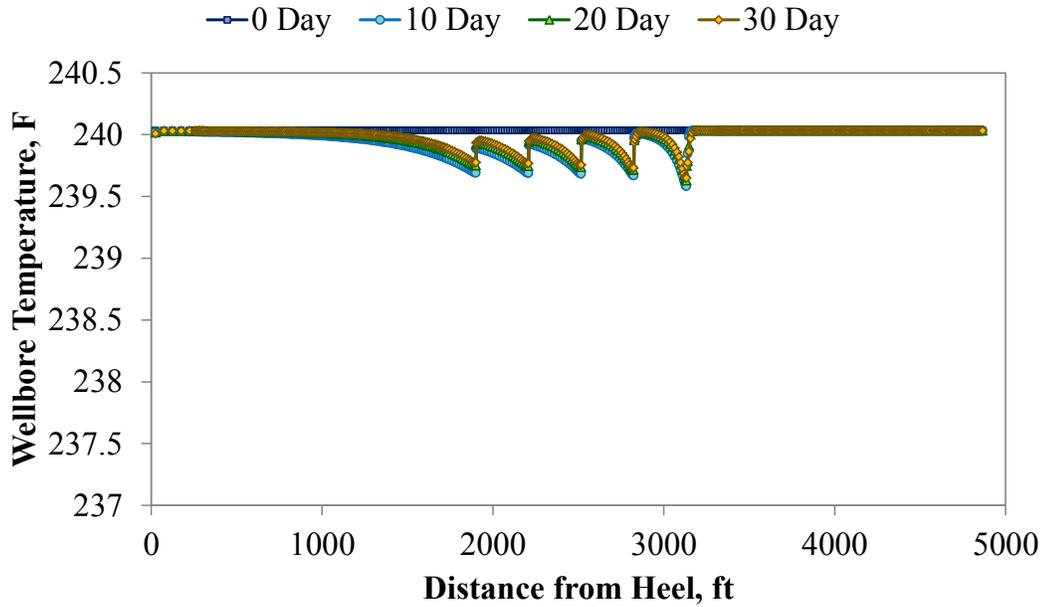
Without network fractures

Fig. 3.26 Comparison of wellbore temperture behavior with and without network fractures (homogeneous fractures case, constant BHP)
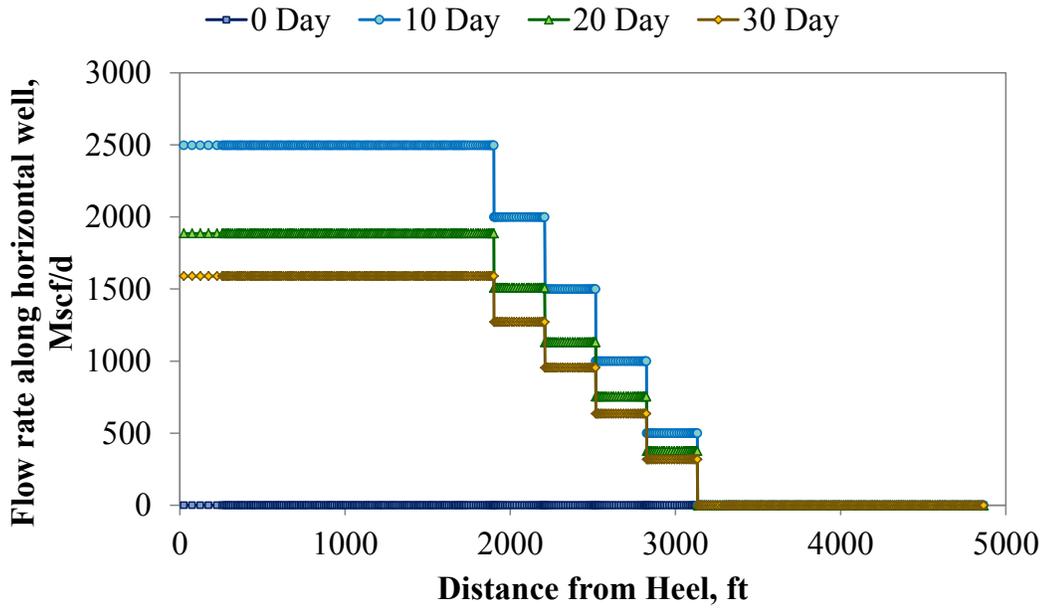
With network fractures
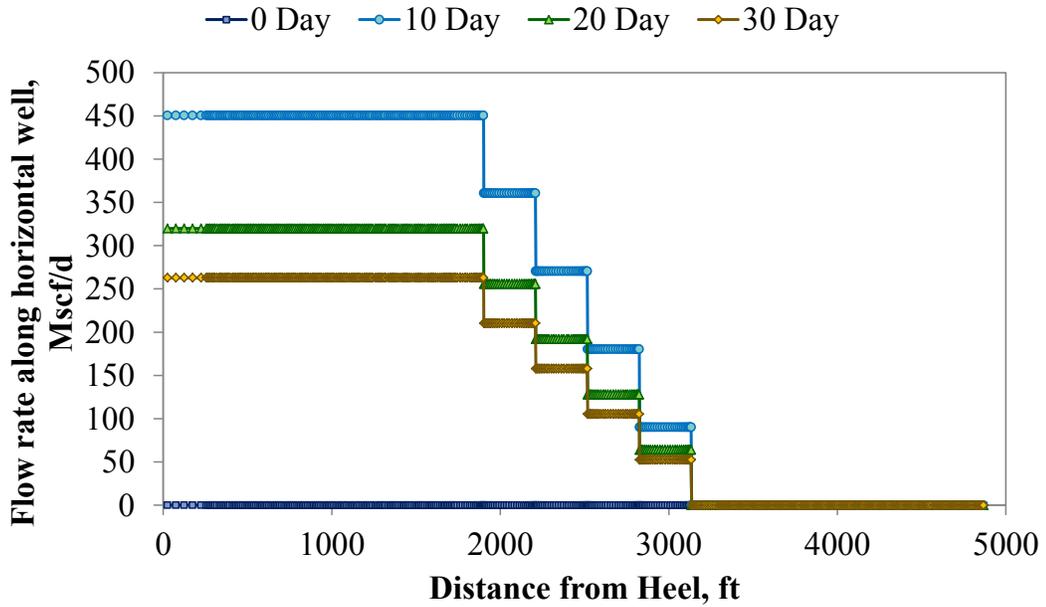
**Without network fractures**

**Fig. 3.27 Comparison of flow rate distribution with and without network fractures
(homogeneous fractures case, constant BHP)**

3.3.4   CONCLUSION AND DISCUSSION OF SYNTHETIC EXAMPLES

Through the above synthetic examples using the developed model, we can see the following specifications of the temperature behavior of a horizontal well with multiple transverse fractures:

1) cooling-heating cycle along the horizontal well is seen because of the gas cooling effect given by the Joule-Thomson effect at perforated zones and heat transfer between the wellbore and formation at the non-perforated zones;

2) fracture location affects the temperature change at the fracture location caused by the fluid mixing effect between wellbore and inflow temperature;

3) inflow variation because of fracture heterogeneity affects wellbore temperatures due to the fluid mixing effect;

and

4) under constant rate condition, network fracture masks large temperature change due to small pressure change at the fracture-formation contact, and under constant BHP condition, network fracture region augments temperature change with increase of flow rate.

As it was examined in the comparison study, it requires so much time for the pressure and temperature front given by one fracture reaches that given by the fractures next to it. In the reality, near the wellbore the high permeable network fractures are created by the multistage treatment, which means there are three regions of primary hydraulic fractures, high permeable network fractures and matrix. Therefore, the geometry of the complex fracture network should be examined for the calibration of the method of the enhanced permeability region.

In addition, we need to work on the sensitivity study for the wellbore temperature using different set of parameters, because it affects the magnitude of the temperature change. Because of the limited accuracy of the measurement tools, the magnitude of the temperature change is very important for the interpretation. In addition, when the fracture parameter is changed, the wellbore temperature is changed because the mechanism of the heat transfer should be different.

4 SENSITIVITY STUDY

4.1 INTRODUCTION

In this section, sensitivity studies are performed to identify influential parameters on temperature behavior in the wellbore. The parameters to be examined include porosity and permeability of the reservoir, fracture half-length, fracture conductivity (fracture width and permeability), fracture porosity (proppant packing pattern), flow rate. The sensitivities are quantified, and primary sensitive parameters are found through this study. Interference between fractures is also examined considering a horizontal well with multiple transverse fractures. According to this study, our final goal is to investigate possibility of property estimation of each parameter in terms of temperature sensitivity.

4.2 OVERVIEW OF SENSITIVITY STUDY

In order to clarify the temperature sensitivity on each parameters and the interference effect between fractures, we use two cases: a horizontal well with one transverse fracture and with multiple transverse fractures. At first, we perform the sensitivity study on the single fracture case. After we quantify their temperature sensitivity, the primary parameters are selected based on the quantified sensitivity. Then, we move to the multiple fracture case in order to consider the change of the sensitivity because of the existence of other fractures.

Fig 4.1 shows the detail procedure of this sensitivity study. At first, we set up models using base case parameters, and perform simulation in order to obtain base case temperature distribution. With a certain range, one parameter value is changed and other parameters are same with that of base case, and we perform the simulation again. This procedure is repeated for all target parameters. We use the temperature data at 30 days production for the sensitivity study.
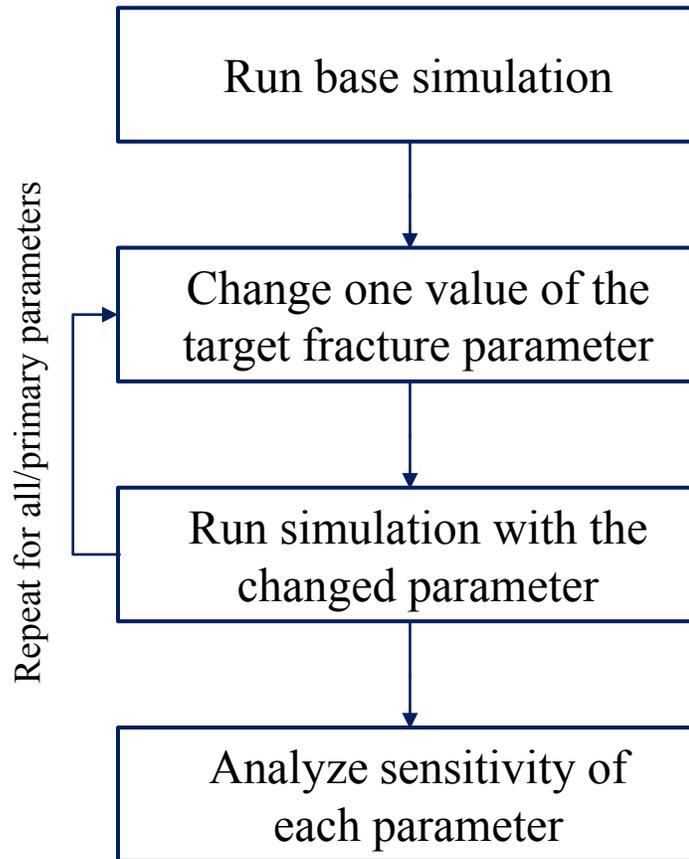
Fig. 4.1 Detail procedure of sensitivity study

Because the sensitivities are affected by the magnitude of the vase values of each parameter besides the parameter value change from base case, we used three different base parameter sets: no network fracture (base 1), high primary fracture with low permeable network fracture zone (base 2) and low primary fracture with high permeable network fracture zone (base 3). **Table 4-1** and **Table 4-2** show base parameters of those situations for single fracture case and multiple fractures case, respectively (estimation of the enhanced permeability and porosity is discussed in Appendix D). **Fig. 4.2** and **Fig. 4.3** show the schematic of the reservoir-wellbore system for single fracture case and multiple fractures case (five transverse fractures), respectively. In the multiple fractures case, all fractures are identical (homogeneous fractures), and the target fracture whose

parameter to be changed is the central fracture. When the no network fracture condition is used in the study, the enhanced permeability zone has the same properties with the matrix zone.

In addition, we also study the effects of the boundary condition of the reservoir simulation. Both conditions of the constant surface rate production and the constant bottom-hole pressure (BHP) production are used in order to consider the influence on the temperature sensitivity.

TABLE 4-1 BASE PARAMETER VALUES FOR SINGLE FRACTURE CASE			
	Base values		
Parameter	Base 1	Base 2	Base 3
Matrix permeability (k_M), md	1.50×10^{-4}	1.50×10^{-4}	1.50×10^{-4}
Enhanced permeability (k_{EPA}), md	1.50×10^{-4}	0.006	0.06
Fracture permeability (k_f), md	4000	400	40
Matrix porosity (ϕ_M), -	8.0%	8.0%	8.0%
Enhanced porosity (ϕ_{EPA}), -	8.0%	8.1%	8.1%
Fracture Porosity (ϕ_F), -	26.00%	26.00%	26.00%
Propped Fracture half length (x_f), ft	150	150	150
Propped Fracture Height (h_f), ft	180	180	180

TABLE 4-2 BASE PARAMETER VALUES FOR MULTIPLE FRACTURES CASE			
	Base Parameters		
Parameter	Base 1	Base 2	Base 3
Matrix permeability (k_M), md	1.50×10^{-4}	1.50×10^{-4}	1.50×10^{-4}
Enhanced permeability (k_{EPA}), md	1.50×10^{-4}	0.006	0.06
Fracture permeability (k_f), md	4000	400	40
Matrix porosity (ϕ_M), -	8.0%	8.00%	8.00%
Enhanced porosity (ϕ_{EPA}), -	8.0%	8.08%	8.10%
Fracture Porosity (ϕ_F), -	26.00%	26.00%	26.00%
Propped Fracture half length (x_f), ft	150	150	150
Propped Fracture Height (h_f), ft	180	180	180
Fracture spacing ($L_{spacing}$), ft	300	300	300
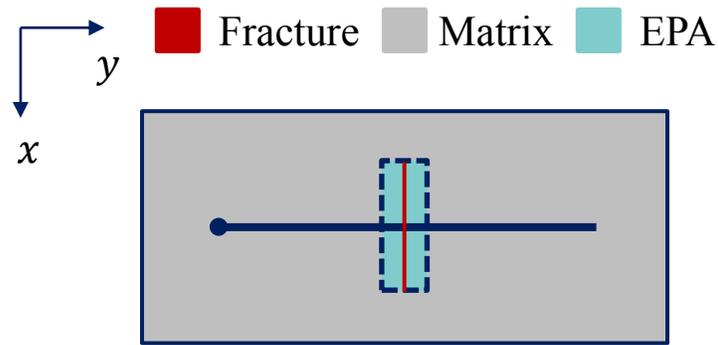
Fig. 4.2 Schematic of the reservoir-wellbore system for single fracture case
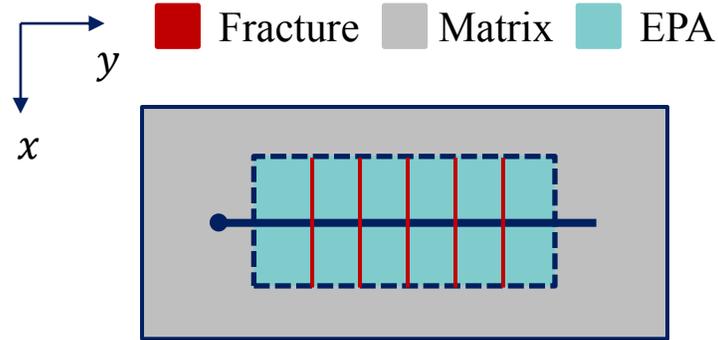
Fig. 4.3 Schematic of the reservoir-wellbore system for multiple fractures case

4.2.1   INTERFERENCE EFFECT

In multiple fractures case, the interference effects among the multiple fractures are examined. **Fig. 4.4** shows the preliminary results of temperature distribution under constant rate boundary condition with different fracture half-length on target fracture. It shows the temperature distribution change occurs with the change of half-length of target fracture. For multiple fractures system, the wellbore temperature at the location is not appropriate indicator of the sensitivity, but the temperature change at the target fracture can express the contribution to the temperature change (Fig. 4.4). Hence, in the following sensitivity studies for both of single fracture case and multiple fracture case, we use the temperature change sensitivities for the analysis.
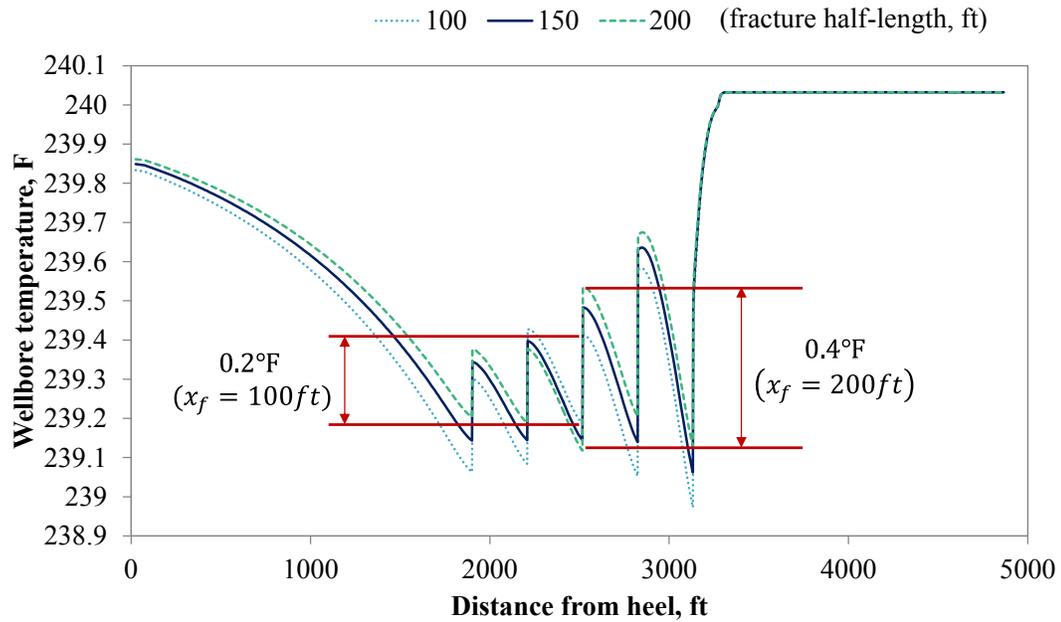
Fig. 4.4 Interference effect by property change of target fracture

4.3 SENSITIVITY STUDY OF SINGLE FRACTURE CASE

Our objective of the sensitivity study of single fracture case is to quantify temperature sensitivities on each parameter, and find the primary parameters which have higher impact on temperature distribution without interference effect of multiple fractures. In order to find the relative importance of parameters, we compare difference of temperature change at the fracture location from given by the changed parameter set from the temperature given by the base parameter set.

In this case, the parameters are changed by $\pm 45\%$ and $\pm 70\%$ from the base values presented in Table 4-1. For constant rate production condition, the surface rate is assumed to be 320 Mscf/d (single phase gas production), and for constant bottom-hole pressure condition, the pressure is assumed to be 2,800 psi.

4.3.1 CONSTANT BOTTOM-HOLE PRESSURE

Fig. 4.5 through Fig. 4.7 show the temperature change with the change of each parameter and the inflow change corresponding to the temperature change. According to these results, higher sensitive parameters are fracture half-length, fracture height, fracture permeability, enhanced permeability and enhanced porosity. The ranking of the sensitivity depends on conditions of the system between primary fracture and secondary fracture network.

Temperature drop change from base   Inflow rate change from base
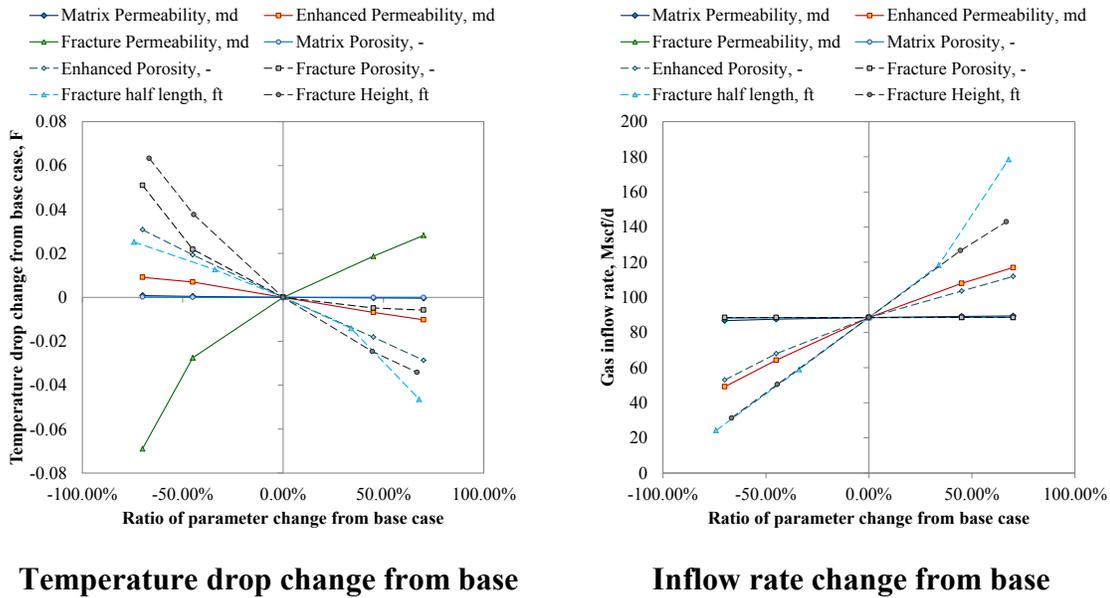
Fig. 4.5 Temperature drop sensitivity of single fracture case

(Constant BHP, no network)
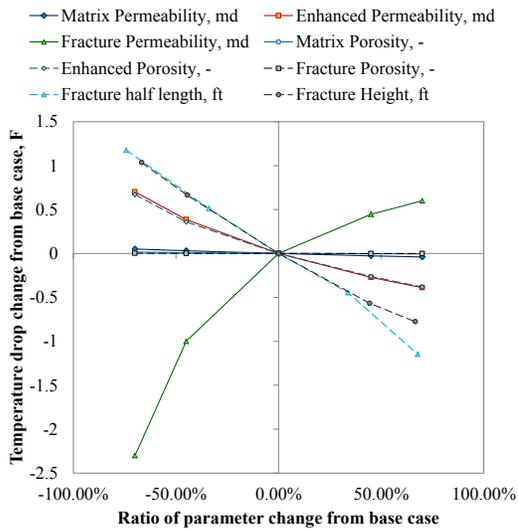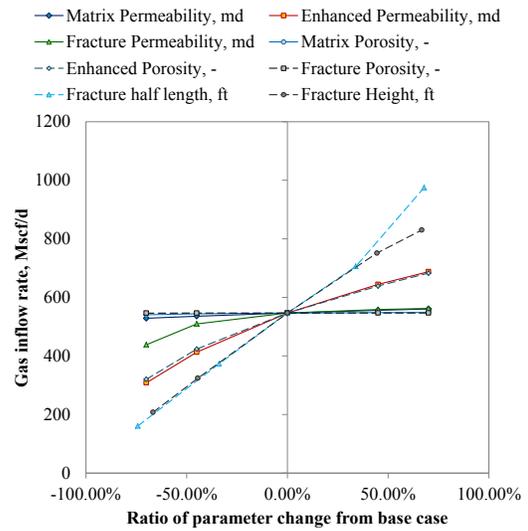
Temperature drop change from base   Inflow rate change from base

Fig. 4.6 Temperature drop sensitivity of single fracture case

(Constant BHP, low permeable network)
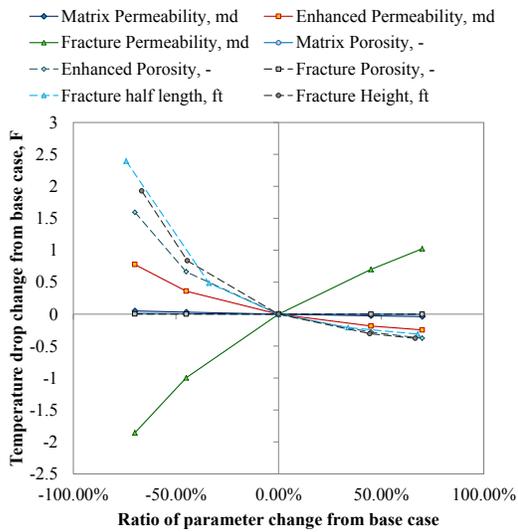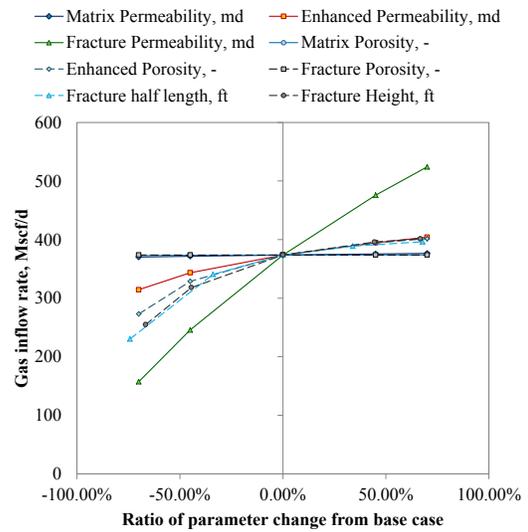
Temperature drop change from base   Inflow rate change from base

Fig. 4.7 Temperature drop sensitivity of single fracture case

(Constant BHP, high permeable network)

85

4.3.2 CONSTANT SURFACE PRODUCTION RATE

Fig. 4.8 through Fig. 4.10 show the temperature drop and the inflow rate change with the change of each parameter. As we can see in Fig. 4.8, when we decrease the parameter values in the no network fracture case, the bottom-hole pressure of the well becomes smaller than the minimum bottom-hole pressure in the reservoir simulation, and it is treated as the same with the constant BHP production case. As we saw in the situation of constant BHP, higher sensitive parameters are fracture half-length, fracture height, fracture permeability, enhanced permeability and enhanced porosity. However, the signs of the temperature sensitivities of these parameters except fracture permeability become opposite. Because this is constant rate case, the inflow rate does not change when we change the parameters as shown in Fig. 4.9 and Fig. 4.10 (Fig. 4.8 is treated as constant BHP case).
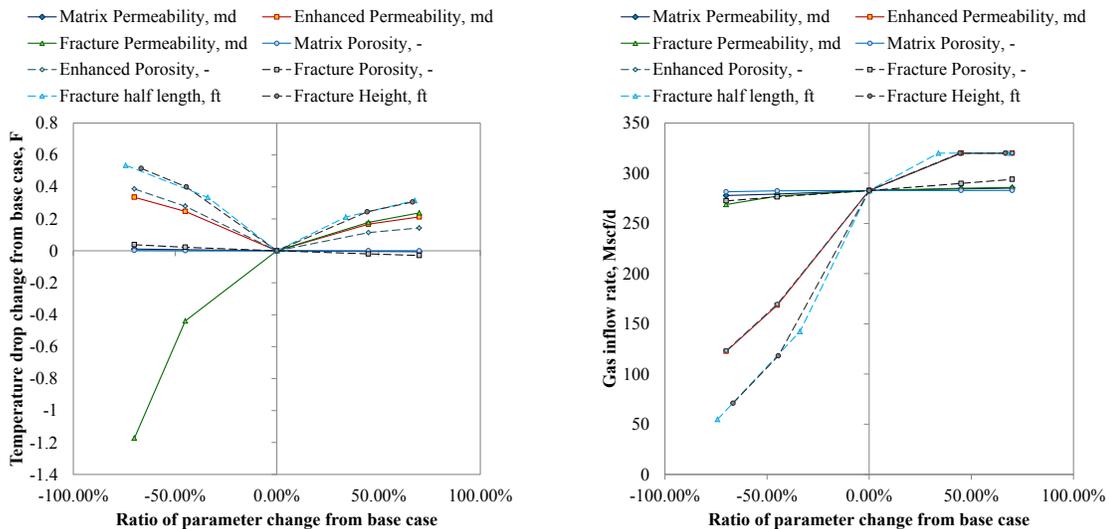
Temperature drop change from base　　**Inflow rate change from base**

Fig. 4.8 Temperature drop sensitivity of single fracture case

(Constant rate, no network)
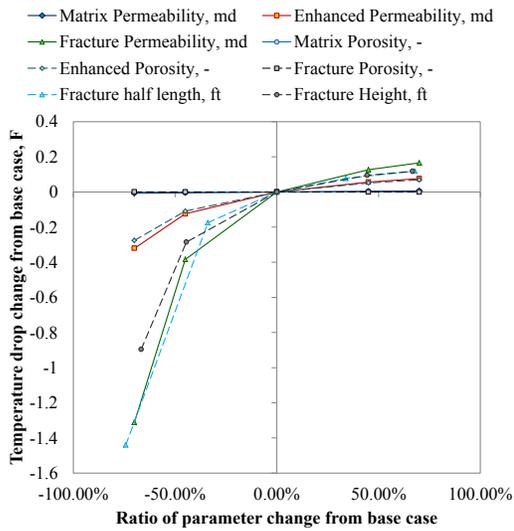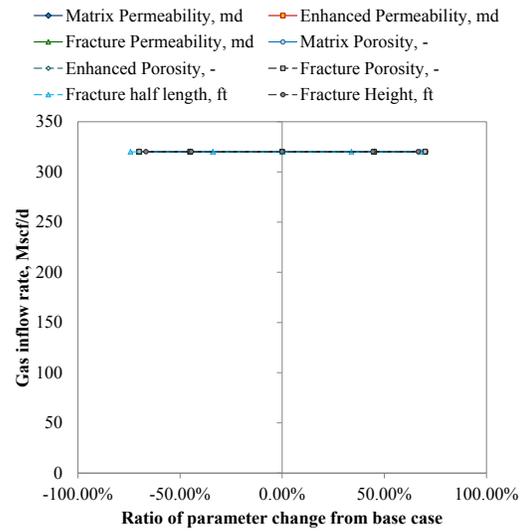
Temperature drop change from base   Inflow rate change from base

Fig. 4.9 Temperature drop sensitivity of single fracture case

(Constant rate, low permeable network)
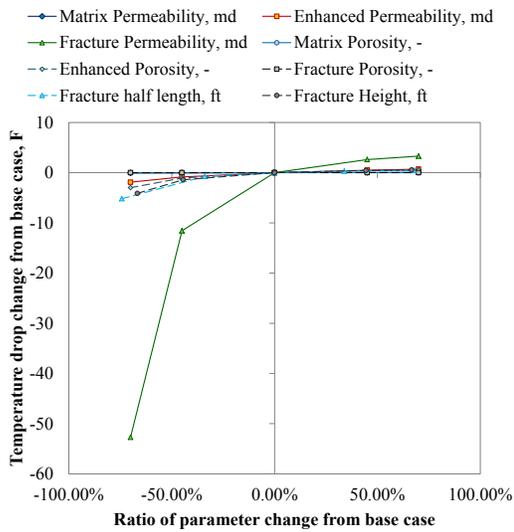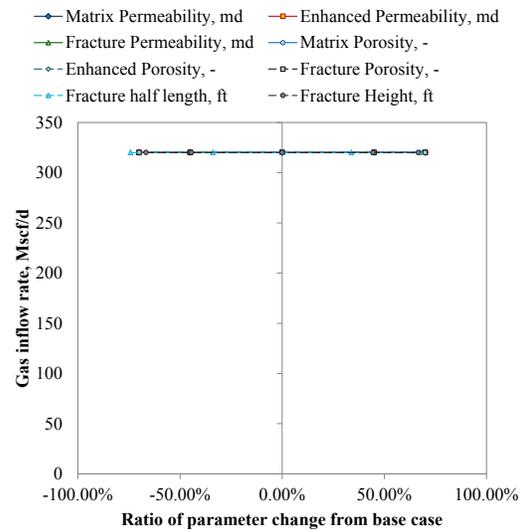
Temperature drop change from base   Inflow rate change from base

Fig. 4.10 Temperature drop sensitivity of single fracture case

(Constant rate, high permeable network)

4.3.3   DISCUSSION OF SINGLE FRACTURE CASE

According to these results, the primary parameters on the temperature drop sensitivity are fracture half-length, fracture height, fracture permeability, enhanced permeability and enhanced porosity. However, the magnitude of the sensitivities is affected by the production condition and fracture and reservoir base properties. And also, the sign of the sensitivity changes with different boundary condition.

For physical interpretations of the sensitivities, the influential parameters in the model are examined, but it is complicated system. For example, under the condition of constant flow rate, with the increase of fracture permeability, the drawdown at the contact of reservoir and fracture is decreased. According to Eq. 2.23 in reservoir model, the change of drawdown affects the term of viscous dissipation heating and thermal expansion in space. In addition, in Eq. 2.101, the pressure change in fracture affects the heat convection term of the wellbore model based on the density change although the change of pressure along fracture is very small. On the other hand, under the condition of constant BHP, with the increase of fracture permeability, the inflow rate at the fracture increases. This leads the velocity change in the fracture, and it affects the term of heat convection, viscous dissipation heating and thermal expansion in reservoir model, and the heat convection term in wellbore model is also affected. So, the estimation of sensitivity is complicated in analytical sense.

According to Fig. 4.5, Fig.4.6 and Fig. 4.7, under the constant BHP condition, the inflow rate increase with the increase of all the above sensitive parameter values. Corresponding to the increase of inflow, the temperature drop decreases for all these parameters except for fracture permeability. This is caused by the increase of the effect by heat convection and viscous dissipation heating in the reservoir because the drawdown pressure change is not large (fluid expansion effect is limited). For fracture permeability case, the change of fracture permeability affects both of the drawdown pressure and inflow rate. This results show the temperature drop increase, which means the effect of gas cooling effect has a major role in the temperature distribution. In addition, Fig. 4.7 shows the when the fracture permeability is not high enough, the

sensitivity of these properties are relatively small. When the fracture half-length and height decrease, Fig. 4.6 and Fig. 4.7 show the dramatic increase of the temperature because of the decrease of the pore volume and inflow rate with the decrease of the enhanced permeability zone. This is confirmed because Fig. 4.5 (this has no enhanced permeability zone) does not show such trend.

On the other hand, according to Fig. 4.8, Fig.4.9 and Fig. 4.10, under the constant rate condition, the wellbore temperature increase with the increase of all parameter values. When the flow rate is fixed, the increase of the permeability or the fracture contact area leads to the drawdown pressure to produce the same amount of production since the velocity is fixed. This gives the lower amount of fluid expansion effect, and the temperature increase at the location.

As we can see in this study, enhanced porosity and enhanced permeability are the influential parameters on the temperature behavior. Enhanced porosity affects the pore volume in the stimulated reservoir region. Enhanced permeability makes the pressure drop smaller from matrix to the contact area of fracture surface. With the change of these values, the inflow rate change (under BHP constant) or bottom-hole pressure change (under constant rate) leads to the change wellbore temperature.

In this study, we considered just 30 days from the beginning of production. Within the short term production, the matrix parameters do not have large impact on the temperature distribution. However, for the long term production (e.g. several years), the matrix permeability and porosity may have some more relative importance on the wellbore temperature.

4. 4   SENSITIVITY STUDY OF MULTIPLE FRACTURES CASE

Comparing to single fracture case, the objective of multiple fractures case is to investigate the interference effect given by other fractures on the target fracture. In this case, the parameters are changed by $\pm45\%$ and $\pm90\%$ from the base values presented in Table 4-2. For constant rate production condition, the surface rate is assumed to be 1600 Mscf/d (single phase gas production), and for constant bottom-hole pressure condition, the pressure is assumed to be 2,800 psi.

Fig. 4.11 through Fig. 4.13 show the temperature drop change from base value and the inflow rate change under the condition of constant BHP production, and **Fig. 4.14 through Fig. 4.16** show them under the condition of constant total production rate. In these cases, we can see the same trend with that given by the constant BHP production in single fracture case.

4.5   SUMMARY OF SENSITIVITY STUDY

Through the sensitivity study, we can select the following parameters as the primary parameters in terms of the wellbore temperature sensitivity: fracture half-length, fracture height, fracture permeability, enhanced permeability and enhanced porosity. The sensitivities of these parameters are affected by a certain production condition, constant rate or constant bottom-hole pressure. In addition, for the multiple fracture cases, the wellbore temperature at one fracture location is affected by other fractures, but when we use the temperature difference between the fracture location and the next toe-side grid, we can see the sensitivity at the fracture location as it is in the similar way with the single fracture case. According to results, temperature drop was augmented with the increase of fracture geometry and fracture network parameters and decreased with the increase of fracture permeability. Also, the downhole situation in the vicinity of the wellbore (e.g. existence of network fracture and structure of fracture network) affects the magnitude of the sensitivity, and the fracturing treatment design such as waterfracs and hybrid treatment should be taken into account for the reservoir grid and parameter design.
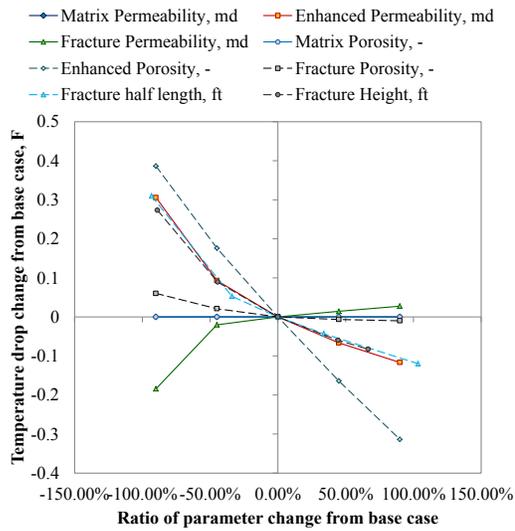
Temperature drop change
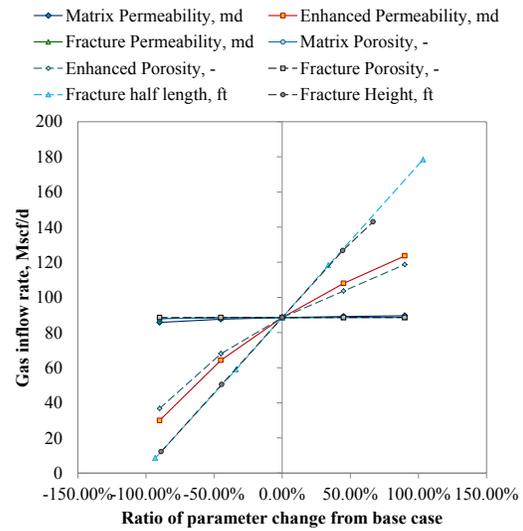
Inflow rate change from base

Fig. 4.11 Temperature drop sensitivity of multiple fractures case

(Constant BHP, no network)
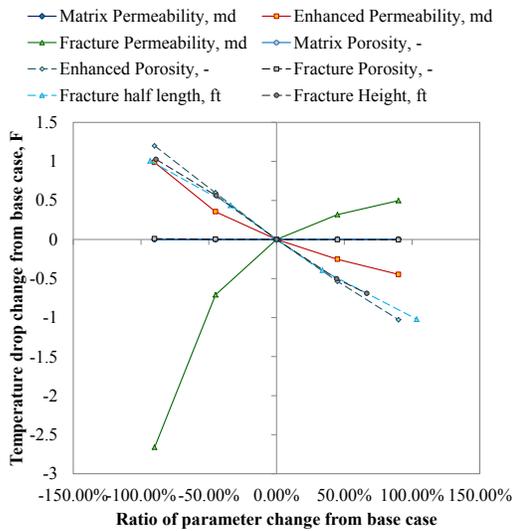
Temperature drop change
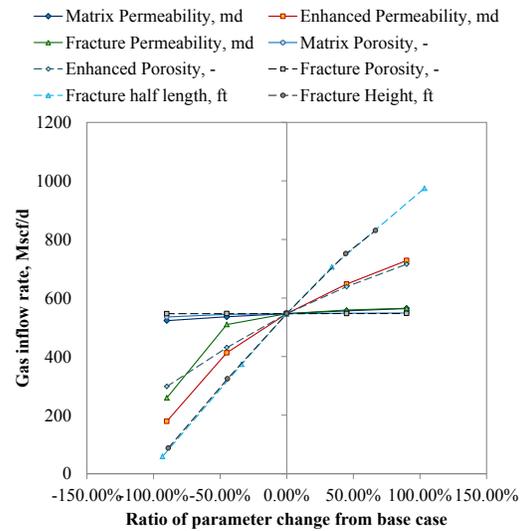
Inflow rate change from base

Fig. 4.12 Temperature drop sensitivity of multiple fractures case

(Constant BHP, low permeable network)

91
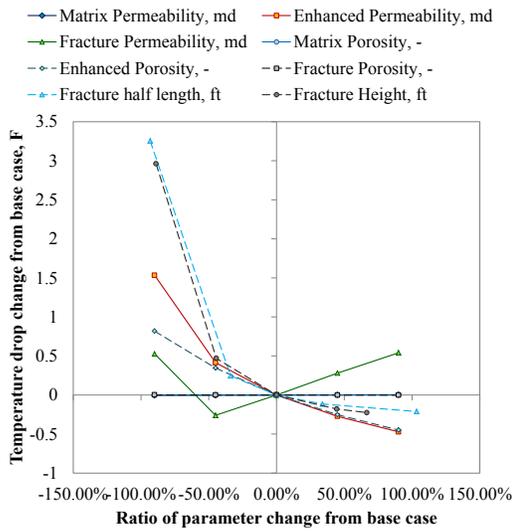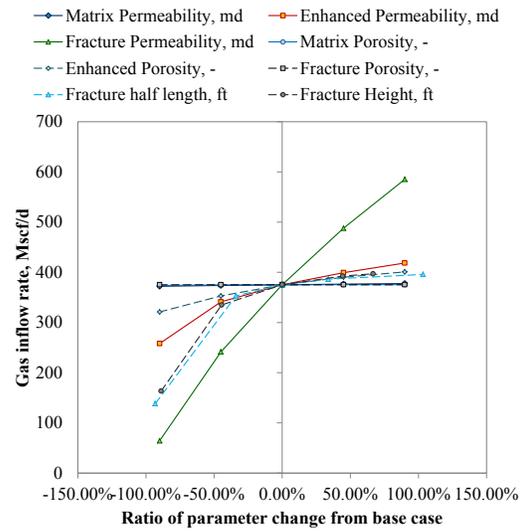
Temperature drop change   Inflow rate change from base

Fig. 4.13 Temperature drop sensitivity of multiple fractures case

(Constant BHP, high permeable network)
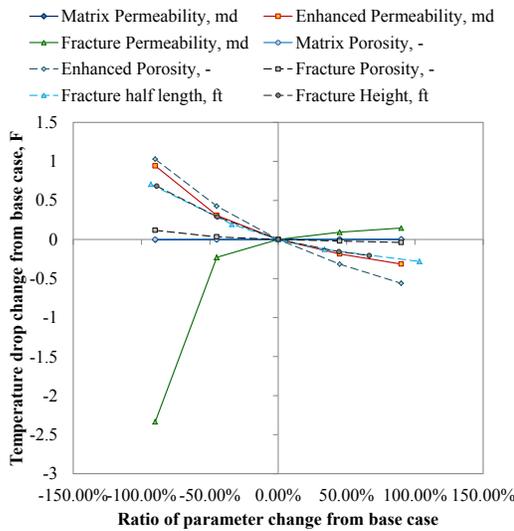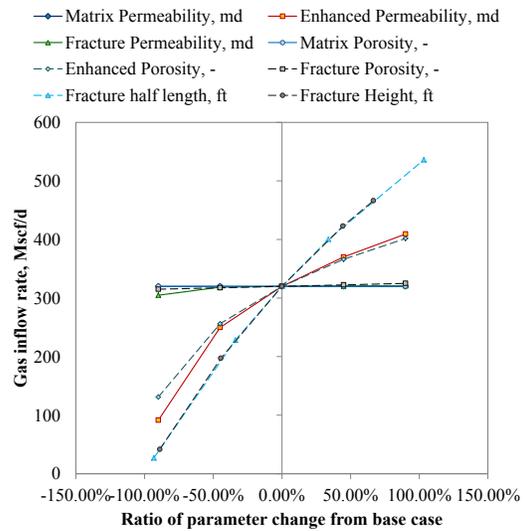
Temperature drop change   Inflow rate change from base

Fig. 4.14 Temperature drop sensitivity of multiple fractures case

(Constant total rate, no network)

92
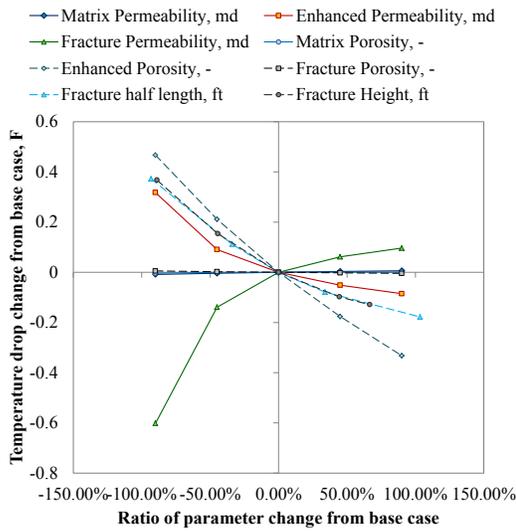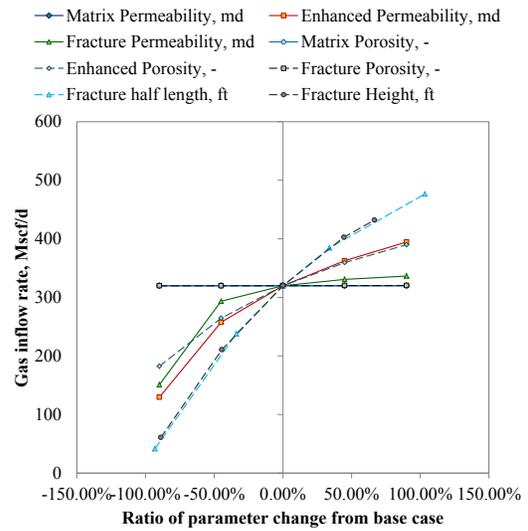
Temperature drop change   Inflow rate change from base

Fig. 4.15 Temperature drop sensitivity of multiple fractures case

(Constant total rate, low permeable network)
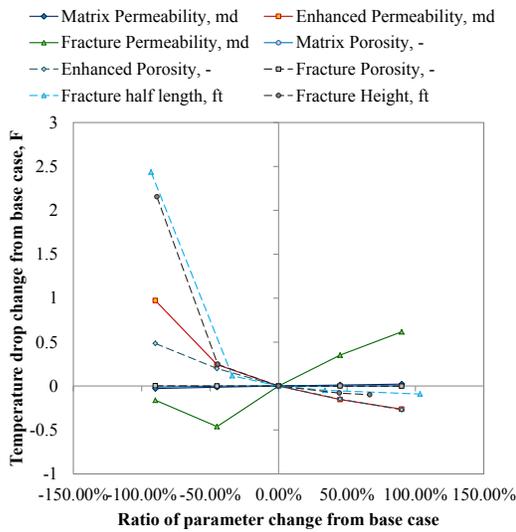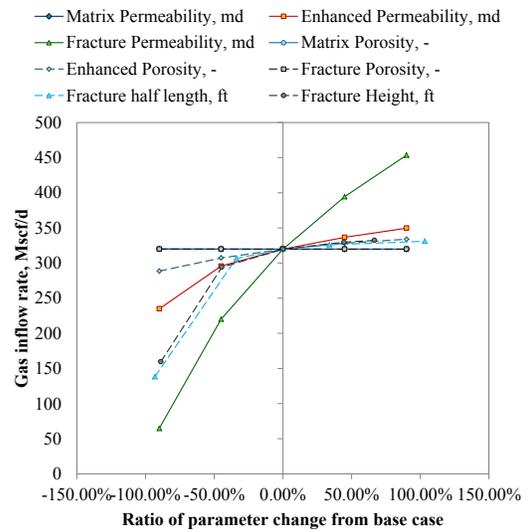
Temperature drop change   Inflow rate change from base

Fig. 4.16 Temperature drop sensitivity of multiple fractures case

(Constant total rate, high permeable network)

93

5 SUMMARY AND CONCLUSION

We extended the temperature prediction model to the horizontal well with multiple fractures in shale reservoir. In the reservoir system, primary hydraulic fractures perpendicular to the horizontal well were modeled with thin grid cells explicitly, and the hydraulically-induced fracture network around the horizontal well was modeled as higher permeable zone to unstimulated matrix zone for the simplicity of the problem and utilization of the computational effectiveness. The reservoir grids between two fractures were logarithmically spaced to capture transient flow behavior. We applied the model to synthetic examples: horizontal well with identical five fractures and with different five fractures. The results of simulation show two fundamental mechanisms which affects wellbore temperature distribution: heat conduction between formation and wellbore fluid at non-perforated zone and wellbore fluid mixing effect at fractures (fluid entry points). In addition, we confirmed that the network structure, fracture heterogeneity and boundary conditions affect temperature distribution also. The network fracture region affects the temperature distribution in the wellbore both in the reservoir and at the contact of reservoir and wellbore. Because there are several modeling methods are presented for the network structure, the accuracy of our method and the detail influence of the network structure need to be examined in the future work.

Sensitivity studies were performed to identify influential parameters out of the reservoir and hydraulic fracture parameters including porosity and permeability of reservoir, half-length and height of fracture, fracture permeability, fracture porosity (proppant packing pattern), fracture network parameters. The results indicate that fracture half-length, fracture height, fracture permeability, enhanced permeability and enhanced porosity are primarily sensitivity parameters on the temperature distribution along the horizontal well. Though there are interference effects between multiple fractures, by using the temperature difference or drop at the fracture location, it is possible to see the temperature sensitivity of each parameter on the target fracture. Also, according to results, it is indicated that temperature drop is augmented with the increase

94

of fracture geometry and fracture network parameters and decreased with the increase of fracture permeability.

These results imply the possibility of using temperature to determine these sensitive parameters, and the quantified parameter sensitivities provide better understandings of the temperature behavior in horizontal well with multiple fractures.

REFERENCES

Anand, J., Somerton, W.H. and Gomaa, E., 1973. Predicting Thermal Conductivities of Formations From Other Known Properties. Society of Petroleum Engineers Journal, 13(5): 267-273.

Bazan, L.W., Larkin, S.D., Lattibeaudiere, M.G. and Palisch, T.T., 2010. Improving Production in the Eagle Ford Shale with Fracture Modeling, Increased Conductivity and Optimized Stage and Cluster Spacing Along the Horizontal Wellbore, Tight Gas Completions Conference. Society of Petroleum Engineers, San Antonio, Texas, USA.

Beggs, H.D. and Robinson, J.R., 1975. Estimating the Viscosity of Crude Oil Systems. SPE Journal of Petroleum Technology, 27(9): 1140-1141.

Bird, R.B., Stewart, W.E. and Lightfoot, E.N., 2002. Transport Phenomena. John Wiley & Sons, Inc., New York.

Brady, J.L. et al., 1998. Improved Production Log Interpretation in Horizontal Wells Using a Combination of Pulsed Neutron Logs, Quantitative Temperature Log Analysis, Time Lapse LWD Resistivity Logs and Borehole Gravity, SPE International Oil and Gas Conference and Exhibition in China, Beijing, China.

Brown, G.A., Kennedy, B. and Meling, T., 2000. Using Fibre-Optic Distributed Temperature Measurements to Provide Real-Time Reservoir Surveillance Data on Wytch Farm Field Horizontal Extended-Reach Wells, SPE Annual Technical Conference and Exhibition, Dallas, Texas, USA.

Cardott, B.J., 2006. Data Relevant to Oklahoma Gas Shales, SWS/EDM Shale Gas Workshop, Midland, Texas, USA.

Carnahan, B.D., Clanton, R.W., Koehler, K.D., Harkins, G.O. and Williams, G.R., 1999. Fiber Optic Temperature Monitoring Technology, SPE Western Regional Meeting. Society of Petroleum Engineers, Inc., Anchorage, Alaska, USA.

Carnegie, A., Roberts, N. and Clyne, I., 1998. Application of New Generation Technology to Horizontal Well Production Logging - Examples from the North

West Shelf of Australia, SPE Asia Pacific Oil and Gas Conference and Exhibition, Perth, Australia.

Cassis, R. et al., 1985. Specific Heat Capacities of Bitumens and Heavy Oils, Reservoir Minerals, Clays, Dehydrated Clays, Asphaltenes, and Cokes. Alberta Oil Sands Technology and Research Authority Journal of Research, 1(3): 163-173.

Chace, D., Wang, J., Mirzwinski, R., Maxit, J. and Trcka, D., 2000. Applications of a New Multiple Sensor Production Logging System for Horizontal and Highly-Deviated Multiphase Producers, SPE Annual Technical Conference and Exhibition, Dallas, Texas, USA.

Chen, N.H., 1979. An Explicit Equation for Friction Factor in Pipe. Industrial & Engineering Chemistry Fundamentals, 18(3): 296-297.

Cheng, Y., 2012. Impacts of the Number of Perforation Clusters and Cluster Spacing on Production Performance of Horizontal Shale-Gas Wells. SPE Reservoir Evaluation & Engineering, 15(1): 31-40.

Cipolla, C.L., Lolon, E. and Mayerhofer, M.J., 2009. Resolving Created, Propped, and Effective Hydraulic-Fracture Length. SPE Production & Operations, 24(4): 619-628.

Cipolla, C.L., Lolon, E.P., Erdle, J.C. and Rubin, B., 2010a. Reservoir Modeling in Shale-Gas Reservoirs. SPE Reservoir Evaluation & Engineering, 13(4): 638-653.

Cipolla, C.L., Warpinski, N.R., Mayerhofer, M., Lolon, E.P. and Vincent, M., 2010b. The Relationship Between Fracture Complexity, Reservoir Properties, and Fracture-Treatment Design. SPE Production & Operations, 25(4): 438-452.

Cipolla, C.L. and Wright, C.A., 2002. Diagnostic Techniques to Understand Hydraulic Fracturing: What? Why? and How? SPE Production & Operations, 17(1): 23-35.

Coats, K.H., 1989. Implicit Compositional Simulation of Single-Porosity and Dual-Porosity Reservoirs, SPE Symposium on Reservoir Simulation, Houston, Texas, USA.

Collins, A.G., 1987. Properties of Produced Waters. In: H.B. Bradley (Editor), Petroleum Engineering Handbook. Society of Petroleum Engineers, Dallas, Texas, pp. 24-17.

Dawkrajai, P., 2006. Temperature Prediction Model for a Producing Horizontal Well. PhD Dissertation, The University of Texas at Austin, Austin, Texas.

Dawkrajai, P., Lake, L.W., Yoshioka, K., Zhu, D. and Hill, A.D., 2006. Detection of Water or Gas Entries in Horizontal Wells from Temperature Profiles, SPE/DOE Symposium on Improved Oil Recovery. Society of Petroleum Engineers, Tulsa, Oklahoma, USA.

Dranchuk, P.M. and Kassem, H.A.-. 1975. Calculation of Z Factors for Natural Gases Using Equations of State. Journal of Canadian Petroleum Technology, 14(3): 34-36.

Duru, O.O. and Horne, R.N., 2010. Modeling Reservoir Temperature Transients and Reservoir-Parameter Estimation Constrained to the Model. SPE Reservoir Evaluation & Engineering, 13(6): 873-883.

East, J.L., Soliman, M.Y. and Augustine, J.R., 2011. Methods for Enhancing Far-Field Complexity in Fracturing Operations. SPE Production & Operations, 26(3): 291-303.

Economides, M.J., Hill, A.D. and Ehlig-Economides, C., 1994. Petroleum Production Systems. Prentice-Hall PTR, Upper Saddle River, New Jersey.

Ertekin, T., Abou-Kassem, J.H. and King, G.R., 2001. Basic Applied Reservoir Simulation. Society of Petroleum Engineers, Richardson, Texas.

Fisher, M.K. et al., 2004. Optimizing Horizontal Completion Techniques in the Barnett Shale Using Microseismic Fracture Mapping, SPE Annual Technical Conference and Exhibition. Society of Petroleum Engineers, Houston, Texas, USA.

Fisher, M.K. et al., 2005. Integrating Fracture-Mapping Technologies to Improve Stimulations in the Barnett Shale. SPE Production & Operations, 20(2): 85-93.

Fitz, D.E., Billingham, M.E., Guzman-Garcia, A.G. and Sunder, R., 2006. Pushing the Envelope for Production Logging in Extended Reach Horizontal Wells in

Chayvo Field, Sakhalin, Russia – New Conveyance and Flow Profiling Approach, SPE Russian Oil and Gas Technical Conference and Exhibition. Society of Petroleum Engineers, Moscow, Russia.

Foucault, H. et al., 2004. A Successful Experience for Fiber Optic and Water Shut Off on Horizontal Wells with Slotted Liner Completion in an Extra Heavy Oil Field, SPE/DOE Symposium on Improved Oil Recovery. Society of Petroleum Engineers, Tulsa, Oklahoma, USA.

Fryer, V.I., Dong, S., Otsubo, Y., Brown, G.A. and Guilfoyle, P., 2005. Monitoring of Real-Time Temperature Profiles Across Multizone Reservoirs during Production and Shut in Periods Using Permanent Fiber-Optic Distributed Temperature Systems, SPE Asia Pacific Oil and Gas Conference and Exhibition. Society of Petroleum Engineers, Jakarta, Indonesia.

Gambill, W.R., 1957. You Can Predict Heat Capacities. Chemical Engineering, 64: 243-248.

Glasbergen, G., Gualtieri, D., Domelen, M.S.V. and Sierra, J., 2009. Real-Time Fluid Distribution Determination in Matrix Treatments Using DTS. SPE Production & Operations, 24(1): 135-146.

Gonzalez, L.E. and Chokshi, R.N., 2012. Wellbore Real-Time Monitoring and Analysis for Shale Reservoirs, SPE Americas Unconventional Resources Conference. Society of Petroleum Engineers, Pittsburgh, Pennsylvania USA.

Gonzalez, M.H., Eakin, B.E. and Lee, A.L., 1970. Viscosity of Natural Gases. Monograph on API Research Project 65. American Petroleum Institute, New York.

Guo, Q. et al., 2012. Shale Gas Drilling Experience and Lessons Learned from Eagle Ford, SPE Americas Unconventional Resources Conference. Society of Petroleum Engineers, Pittsburgh, Pennsylvania USA.

Hasan, A.R. and Kabir, C.S., 1991. Heat Transfer During Two-Phase Flow in Wellbores; Part I--Formation Temperature, SPE Annual Technical Conference and Exhibition, Dallas, Texas, USA.

Hasan, A.R. and Kabir, C.S., 1994. Aspects of Wellbore Heat Transfer During Two-Phase Flow (includes associated papers 30226 and 30970). SPE Production & Operations, 9(3): 211-216.

Hasan, A.R., Kabir, C.S. and Wang, X., 1997. Development and Application of a Wellbore/Reservoir Simulator for Testing Oil Wells. SPE Formation Evaluation, 12(3): 182-188.

Hasan, A.R., Kabir, C.S. and Wang, X., 1998. Wellbore Two-Phase Flow and Heat Transfer During Transient Testing. SPE Journal, 3(2): 174-180.

Heddleston, D.C., 2009. Horizontal Well Production Logging Deployment and Measurement Techniques for US Land Shale Hydrocarbon Plays, SPE Production and Operations Symposium. Society of Petroleum Engineers, Oklahoma City, Oklahoma, USA.

Heel, A.P.v., Boerrigter, P.M. and Dorp, J.J.v., 2008. Thermal and Hydraulic Matrix-Fracture Interaction in Dual-Permeability Simulation. SPE Reservoir Evaluation & Engineering, 11(4): 735-749.

Hill, A.D., 1990. Production Logging: Theoretical and Interpretive Elements. Henry L. Doherty Memorial Fund of AIME, Society of Petroleum Engineers, Richardson, Texas.

Hoang, H.N., Mahadevan, J. and Lopez, H., 2012. Injection Profiling During Limited-Entry Fracturing Using Distributed-Temperature-Sensor Data. SPE Journal, 17(3): 752-767.

Huckabee, P.T., 2009. Optic Fiber Distributed Temperature for Fracture Stimulation Diagnostics and Well Performance Evaluation, SPE Hydraulic Fracturing Technology Conference. Society of Petroleum Engineers, The Woodlands, Texas, USA.

Huebsch, H.T. et al., 2008. Monitoring Inflow Distribution in Multi-zone, Velocity String Gas Wells Using Slickline Deployed Fiber Optic Distributed Temperature Measurements, SPE Annual Technical Conference and Exhibition. Society of Petroleum Engineers, Denver, Colorado, USA.

Izgec, B., Kabir, C.S., Zhu, D. and Hasan, A.R., 2007. Transient Fluid and Heat Flow Modeling in Coupled Wellbore/Reservoir Systems. SPE Reservoir Evaluation & Engineering, 10(3): 294-301.

Johnson, D.O., Sierra, J.R., Kaura, J.D. and Gualtieri, D., 2006. Successful Flow Profiling of Gas Wells Using Distributed Temperature Sensing Data, SPE Annual Technical Conference and Exhibition. Society of Petroleum Engineers, San Antonio, Texas, USA.

Julian, J.Y., 2007. Downhole Leak Determination Using Fiber-Optic Distributed-Temperature Surveys at Prudhoe Bay, Alaska, SPE Annual Technical Conference and Exhibition. Society of Petroleum Engineers, Anaheim, California, USA.

Kabir, C.S., Hasan, A.R., Jordan, D.L. and Wang, X., 1996. A Wellbore/Reservoir Simulator for Testing Gas Wells in High-Temperature Reservoirs. SPE Formation Evaluation, 11(2): 128-134.

Kazemi, H., Merrill Jr., L.S., Porterfield, K.L. and Zeman, P.R., 1976. Numerical Simulation of Water-Oil Flow in Naturally Fractured Reservoirs. Society of Petroleum Engineers Journal, 16(6): 317-326.

Kelder, O. et al., 2005. Expanding Advanced Production Logging Operations to Short Radius Horizontal Wells, SPE Middle East Oil and Gas Show and Conference. Society of Petroleum Engineers, Kingdom of Bahrain.

Ketter, A.A., Daniels, J.L., Heinze, J.R. and Waters, G., 2008. A Field Study in Optimizing Completion Strategies for Fracture Initiation in Barnett Shale Horizontal Wells. SPE Production & Operations, 23(3): 373-378.

Knauss, M.E., Field, B.J. and Bartel, J.E., 1985. Completion Interval Selection in the Lost Hills Field, Southeast Flank, Kern County, California. Journal of Petroleum Technology, 37(6): 1058-1064.

Kragas, T.K., Williams, B.A. and Myers, G.A., 2001. The Optic Oil Field: Deployment and Application of Permanent In-Well Fiber Optic Sensing Systems for

Production and Reservoir Monitoring, SPE Annual Technical Conference and Exhibition. Society of Petroleum Engineers, New Orleans, Louisiana, USA.

Lake, L.W., 2010. Enhanced Oil Recovery. Society of Petroleum Engineers, Richardson, Texas.

Li, Z., 2010. Interpreting Horizontal Well Flow Profiles and Optimizing Well Performatnce by Downhole Temperature and Pressure Data. PhD Dissertation, Texas A&M University, College Staition, College Staition, Texas.

Li, Z., Yin, J., Zhu, D. and Datta-Gupta, A., 2011. Using Downhole Temperature Measurement to Assist Reservoir Characterization and Optimization. Journal of Petroleum Science and Engineering, 78(2): 454-463.

Li, Z. and Zhu, D., 2010. Predicting Flow Profile of Horizontal Well by Downhole Pressure and Distributed-Temperature Data for Waterdrive Reservoir. SPE Production & Operations, 25(3): 296-304.

Maubeuge, F., Arquis, E. and Bertrand, O., 1994. MOTHER: A Model for Interpreting Thermometrics, SPE Annual Technical Conference and Exhibition, New Orleans, Louisiana, USA.

Maxwell, S.C., Waltman, C., Warpinski, N.R., Mayerhofer, M.J. and Boroumand, N., 2009. Imaging Seismic Deformation Induced by Hydraulic Fracture Complexity. SPE Reservoir Evaluation & Engineering, 12(1): 48-52.

Mayerhofer, M.J. et al., 2010. What Is Stimulated Reservoir Volume? SPE Production & Operations, 25(1): 89-98.

Mayerhofer, M.J., Lolon, E.P., Youngblood, J.E. and Heinze, J.R., 2006. Integration of Microseismic Fracture Mapping Results with Numerical Fracture Network Production Modeling in the Barnett Shale, SPE Annual Technical Conference and Exhibition. Society of Petroleum Engineers, San Antonio, Texas, USA.

McCain, W.D., 1990. The Properties of Petroleum Fluids, 2nd Edition. PennWell Publishing Company, Tulsa, Oklahoma.

Mccluskey, A.E., 2012. Production Logging on Coil Tubing in a Marcellus Shale Horizontal Completion, SPE/ICoTA Coiled Tubing & Well Intervention

Conference and Exhibition. Society of Petroleum Engineers, The Woodlands, Texas, USA.

Medeiros, F., Kurtoglu, B., Ozkan, E. and Kazemi, H., 2010a. Analysis of Production Data From Hydraulically Fractured Horizontal Wells in Shale Reservoirs. SPE Reservoir Evaluation & Engineering, 13(3): 559-568.

Medeiros, F., Ozkan, E. and Kazemi, H., 2008. Productivity and Drainage Area of Fractured Horizontal Wells in Tight Gas Reservoirs. SPE Reservoir Evaluation & Engineering, 11(5): 902-911.

Medeiros, F., Ozkan, E. and Kazemi, H., 2010b. A Semianalytical Approach To Model Pressure Transients in Heterogeneous Reservoirs. SPE Reservoir Evaluation & Engineering, 13(2): 341-358.

Meyer, B.R., Bazan, L.W., Jacot, R.H. and Lattibeaudiere, M.G., 2010. Optimization of Multiple Transverse Hydraulic Fractures in Horizontal Wellbores, SPE Unconventional Gas Conference. Society of Petroleum Engineers, Pittsburgh, Pennsylvania, USA.

Miller, C.W., 1980. Wellbore Storage Effects in Geothermal Wells. Society of Petroleum Engineers Journal, 20(6): 555-566.

Molenaar, M.M., Fidan, E. and Hill, D., 2012. Real-Time Downhole Monitoring Of Hydraulic Fracturing Treatments Using Fibre Optic Distributed Temperature and Acoustic Sensing, SPE/EAGE European Unconventional Resources Conference and Exhibition. Society of Petroleum Engineers, Vienna, Austria.

Moridis, G.J., Blasingame, T.A. and Freeman, C.M., 2010. Analysis of Mechanisms of Flow in Fractured Tight-Gas and Shale-Gas Reservoirs, SPE Latin American and Caribbean Petroleum Engineering Conference. Society of Petroleum Engineers, Lima, Peru.

Mukerji, P., Zaouali, Z. and Rees, H., 2006. The Role of Enhanced Production Logging Measurements in Challenging Openhole Horizontal Completions, SPE Annual Technical Conference and Exhibition. Society of Petroleum Engineers, San Antonio, Texas, USA.

Muradov, K.M. and Davies, D.R., 2011. Novel Analytical Methods of Temperature Interpretation in Horizontal Wells. SPE Journal, 16(3): 637-647.

Mustafa, H.D., Abdouche, G., Khedr, O.H., Elkadi, A. and Al-Mutairi, A.M., 2005. A New Production Logging Tool Allows a Superior Mapping of the Fluid Velocities and Holdups inside the Wellbore, SPE Middle East Oil and Gas Show and Conference. Society of Petroleum Engineers, Kingdom of Bahrain.

Ouyang, L.-B., Arbabi, S. and Aziz, K., 1998. General Wellbore Flow Model for Horizontal, Vertical, and Slanted Well Completions. SPE Journal, 3(2): 124-133.

Ouyang, L.-B. and Belanger, D.L., 2006. Flow Profiling by Distributed Temperature Sensor (DTS) System—Expectation and Reality. SPE Production & Operations, 21(2): 269-281.

Ozkan, E., Brown, M.L., Raghavan, R. and Kazemi, H., 2011. Comparison of Fractured-Horizontal-Well Performance in Tight Sand and Shale Reservoirs. SPE Reservoir Evaluation & Engineering, 14(2): 248-259.

Peaceman, D.W., 1983. Interpretation of Well-Block Pressures in Numerical Reservoir Simulation With Nonsquare Grid Blocks and Anisotropic Permeability. Society of Petroleum Engineers Journal, 23(3): 531-543.

Perry, R.H., Green, D.W. and Maloney, J.O., 1984. Chemical Engineers' Handbook. McGraw-Hill Book Company.

Pinzon, I.D., Brown, G.A., Davies, J.E. and Mammadkhan, F., 2007. Monitoring Production from Gravel-Packed Sand-Screen Completions on BP's Azeri Field Wells Using Permanently Installed Distributed Temperature Sensors, SPE Annual Technical Conference and Exhibition. Society of Petroleum Engineers, Anaheim, California, USA.

Pope, C.D., Palisch, T. and Saldungaray, P., 2012. Improving Completion and Stimulation Effectiveness in Unconventional Reservoirs- Field Results in the Eagle Ford Shale of North America, SPE/EAGE European Unconventional Resources Conference and Exhibition. Society of Petroleum Engineers, Vienna, Austria.

Ramey, H.J., 1962. Wellbore Heat Transmission. Journal of Petroleum Technology, 14(4): 427-435.

Ramurthy, M., Barree, R.D., Kundert, D.P., Petre, J.E. and Mullen, M.J., 2011. Surface-Area vs. Conductivity-Type Fracture Treatments in Shale Reservoirs. SPE Production & Operations, 26(4): 357-367.

Sagar, R., Doty, D.R. and Schmidt, Z., 1991. Predicting Temperature Profiles in a Flowing Well. SPE Production Engineering, 6(4): 441-448.

Sask, D., Hundt, C.D., Slade, J.M. and Daly, P., 2007. Production and Video Logging in Horizontal Low Permeability Gas Wells, Rocky Mountain Oil & Gas Technology Symposium. Society of Petroleum Engineers, Denver, Colorado, USA.

Satter, A., 1965. Heat Losses During Flow of Steam Down a Wellbore. Journal of Petroleum Technology, 17(7): 845-851.

Sierra, J.R. et al., 2008. DTS Monitoring Data of Hydraulic Fracturing: Experiences and Lessons Learned, SPE Annual Technical Conference and Exhibition. Society of Petroleum Engineers, Denver, Colorado, USA.

Standing, M.B., 1977. Volumetric and Phase Behavior of Oil Field Hydrocarbon Systems. California Research Corp., Dallas, Texas.

Stegent, N.A., Wagner, A.L., Mullen, J. and Borstmayer, R.E., 2010. Engineering a Successful Fracture-Stimulation Treatment in the Eagle Ford Shale, Tight Gas Completions Conference. Society of Petroleum Engineers, San Antonio, Texas, USA.

Sui, W., 2009. Determining Multilayer Formation Properties from Transient Temperature and Pressure Measurements. PhD Dissertation, Texas A&M University, College Station, Texas.

Sui, W., Ehlig-Economides, C.A., Zhu, D. and Hill, A.D., 2010. Determining Multilayer Formation Properties from Transient Temperature and Pressure Measurements in Commingled Gas Wells, International Oil and Gas Conference and Exhibition in China. Society of Petroleum Engineers, Beijing, China.

Sui, W., Zhu, D., Hill, A.D. and Economides, C., 2008a. Model for Transient Temperature and Pressure Behavior in Commingled Vertical Wells, SPE Russian Oil and Gas Technical Conference and Exhibition. Society of Petroleum Engineers, Moscow, Russia.

Sui, W., Zhu, D., Hill, A.D. and Ehlig-Economides, C.A., 2008b. Determining Multilayer Formation Properties From Transient Temperature and Pressure Measurements, SPE Annual Technical Conference and Exhibition. Society of Petroleum Engineers, Denver, Colorado, USA.

Sutton, R.P., 1985. Compressibility Factors for High-Molecular-Weight Reservoir Gases, SPE Annual Technical Conference and Exhibition, Las Vegas, Nevada, USA.

Tabatabaei, M. and Zhu, D., 2012. Fracture-Stimulation Diagnostics in Horizontal Wells through Use of Distributed-Temperature-Sensing Technology. SPE Production & Operations, 27(4): 356-362.

Tan, X., Tabatabaei, M., Zhu, D. and Hill, A.D., 2012. Diagnosis of Acid Placement from Temperature Profiles. SPE Production & Operations, 27(3): 284-293.

Tanaka, S., 2010. A Streamline-Based Dual-Porosity Model. Master, Waseda University, Tokyo, Japan.

Thompson, J. et al., 2011. An Overview of Horizontal-Well Completions in the Haynesville Shale. Journal of Canadian Petroleum Technology, 50(6): 22-35.

Warpinski, N.R., Mayerhofer, M.J., Vincent, M.C., Cipolla, C.L. and Lolon, E.P., 2009. Stimulating Unconventional Reservoirs: Maximizing Network Growth While Optimizing Fracture Conductivity. Journal of Canadian Petroleum Technology, 48(10): 39-51.

Warren, J.E. and Root, P.J., 1963. The Behavior of Naturally Fractured Reservoirs.

Xie, J., Yang, C., Gupta, N., King, M.J. and Datta-gupta, A., 2012. Integration of Shale Gas Production Data and Microseismic for Fracture and Reservoir Properties Using Fast Marching Method, SPE Eastern Regional Meeting. Society of Petroleum Engineers, Lexington, Kentucky, USA.

Yin, J., Xie, J., Datta-gupta, A. and Hill, A.D., 2011. Improved Characterization and Performance Assessment of Shale Gas Wells by Integrating Stimulated Reservoir Volume and Production Data, SPE Eastern Regional Meeting. Society of Petroleum Engineers, Columbus, Ohio, USA.

Yoshioka, K., 2007. Detection of Water or Gas Entry into Horizontal Wells by Using Permanent Downhole Monitoring Systems. PhD Dissertation, Texas A&M University, College Station, Texas.

Yoshioka, K., Zhu, D., Hill, A.D., Dawkrajai, P. and Lake, L.W., 2005a. A Comprehensive Model of Temperature Behavior in a Horizontal Well, SPE Annual Technical Conference and Exhibition. Society of Petroleum Engineers, Dallas, Texas, USA.

Yoshioka, K., Zhu, D., Hill, A.D., Dawkrajai, P. and Lake, L.W., 2007. Prediction of Temperature Changes Caused by Water or Gas Entry into a Horizontal Well. SPE Production & Operations, 22(4): 425-433.

Yoshioka, K., Zhu, D., Hill, A.D. and Lake, L.W., 2005b. Interpretation of Temperature and Pressure Profiles Measured in Multilateral Wells Equipped with Intelligent Completions, SPE Europec/EAGE Annual Conference. Society of Petroleum Engineers, Madrid, Spain.

Yoshioka, K., Zhu, D., Hill, A.D. and Lake, L.W., 2009. A New Inversion Method to Interpret Flow Profiles From Distributed Temperature and Pressure Measurements in Horizontal Wells. SPE Production & Operations, 24(4): 510-521.

Zeybek, M., Al-Muthana, A.S., Kelder, O. and Al-Ismail, M., 2005. Advances in Integrated Horizontal Production Logging in Openhole Completions, SPE Annual Technical Conference and Exhibition. Society of Petroleum Engineers, Dallas, Texas, USA.

Zhang, X., Du, C., Deimbacher, F., Crick, M. and Harikesavanallur, A., 2009. Sensitivity Studies of Horizontal Wells with Hydraulic Fractures in Shale Gas

Reservoirs, International Petroleum Technology Conference. 2009, International Petroleum Technology Conference, Doha, Qatar.

APPENDIX A

DERIVATION OF INFLOW TEMPERATURE MODEL

In this section, a detail derivation of the inflow temperature model is presented.

Open hole or pipe with open area

At the place where pipe has open zone, the pressure gradient is computed by $\frac{dp}{dr} = \frac{a}{r}$. The second order ordinary differential equation for the inflow temperature is given by

$$\sum_{j=1}^{N_p}\left(\rho_j C_{p,j}\frac{k_e k_{rj}}{\mu_j}a\right)\frac{1}{r}\frac{dT}{dr} - \sum_{j=1}^{N_p}\left(\beta_j\frac{k_e k_{rj}}{\mu_j}a^2\right)\frac{T}{r^2}$$

$$+K_{Tt}\frac{1}{r}\frac{d}{dr}\left(r\frac{dT}{dr}\right) + \sum_{j=1}^{N_p}\left(\frac{k_e k_{rj}}{\mu_j}a^2\right)\frac{1}{r^2} = 0, \quad \text{............}(A.1)$$

and the associated boundary conditions are

$$T = T_{grid}, \qquad\qquad\qquad \text{at } r = r_{eff} \quad \text{.......................................}(A.2)$$

$$K_{Tt}\frac{dT}{dr}\bigg|_{r=r_w} = U_T\big(T|_{r=r_w} - T_w\big), \text{ at } r = r_w \quad \text{...}(A.3)$$

Since we assume that the fluid properties and saturations are constant in one time step, Eq. A.1 is simplified into

$$K_{Tt}r^2\frac{d^2T}{dr^2} + C_1 r\frac{dT}{dr} - C_2 T + C_3 = 0, \quad \text{...}(A.4)$$

where

$$C_1 = \sum_{j=1}^{N_p}\left(\rho_j C_{p,j}\frac{k_e k_{rj}}{\mu_j}a\right) + K_{Tt}, \quad \text{...}(A.5)$$

$$C_2 = \sum_{j=1}^{N_p}\left(\beta_j\frac{k_e k_{rj}}{\mu_j}a^2\right), \quad \text{..}(A.6)$$

and

$$C_3 = \sum_{j=1}^{N_p}\left(\frac{k_e k_{rj}}{\mu_j}a^2\right). \quad \text{...}(A.7)$$

At first, consider the following complementary equation:

$$K_{Tt}r^2\frac{d^2T}{dr^2} + C_1r\frac{dT}{dr} - C_2T = 0. \quad\text{...(A.8)}$$

Assume that a solution to this Euler-Cauchy equation is proportional to r^λ where λ is a constant. Substitute $T(r) = r^\lambda$ into Eq. A.8 and we can get

$$r^\lambda(K_{Tt}\lambda(\lambda - 1) + C_1\lambda - C_2) = 0. \quad\text{...(A.9)}$$

Since the range of the radius is $r_w \le r \le r_{eff}$, Eq. A.9 is divided by $r^\lambda \ne 0$. Then we can get

$$K_{Tt}\lambda^2 + (C_1 - K_{Tt})\lambda - C_2 = 0. \quad\text{..(A.10)}$$

Solve this with respect to λ, we can get

$$\lambda = \frac{1}{2} - \frac{C_1}{2K_{Tt}} \pm \frac{1}{2K_{Tt}}\sqrt{(C_1 - K_{Tt})^2 + 4K_{Tt}C_2}. \quad\text{..(A.11)}$$

Let n_1 and n_2 be

$$n_1 = \frac{1}{2}\left(1 - \frac{C_1}{K_{Tt}}\right) + \frac{1}{2}\sqrt{\left(1 - \frac{C_1}{K_{Tt}}\right)^2 + \frac{4C_2}{K_{Tt}}}, \quad\text{................................(A.12)}$$

and

$$n_2 = \frac{1}{2}\left(1 - \frac{C_1}{K_{Tt}}\right) - \frac{1}{2}\sqrt{\left(1 - \frac{C_1}{K_{Tt}}\right)^2 + \frac{4C_2}{K_{Tt}}}. \quad\text{...............................(A.13)}$$

These are rearranged into

$$n_1 = -\frac{1}{2}\omega + \frac{1}{2}\sqrt{\omega^2 + \frac{4k_e a^2}{K_{Tt}}\sum_{j=1}^{N_p}\left(\beta_j\frac{k_{rj}}{\mu_j}\right)}, \quad\text{...(A.14)}$$

$$n_2 = -\frac{1}{2}\omega - \frac{1}{2}\sqrt{\omega^2 + \frac{4k_e a^2}{K_{Tt}}\sum_{j=1}^{N_p}\left(\beta_j\frac{k_{rj}}{\mu_j}\right)}, \quad\text{...(A.15)}$$

where

$$\omega = \left(\sum_{j=1}^{N_p}\rho_j C_{p,j}\frac{k_{rj}}{\mu_j}\right)\frac{k_e a}{K_{Tt}}. \quad\text{...(A.16)}$$

The general solution of Eq. A.8 is expressed using arbitrary constants (c_1 and c_2) as

$$T(r) = c_1 r^{n_1} + c_2 r^{n_2}. \quad\text{..(A.17)}$$

Next, the particular solution is determined to Eq. A.4. Consider the Wronskian $\mathcal{W}$:

$$\mathcal{W}(r) = \begin{vmatrix} r^{n_1} & r^{n_2} \\ \frac{d}{dr}r^{n_1} & \frac{d}{dr}r^{n_2} \end{vmatrix} = \begin{vmatrix} r^{n_1} & r^{n_2} \\ n_1 r^{n_1-1} & n_2 r^{n_2-1} \end{vmatrix} = (n_2 - n_1)r^{n_1+n_2-1}.$$

$$\text{...(A.18)}$$

Eq. A.4 is divided by $K_{Tt}r^2$ and it is rearranged into

$$\frac{d^2T}{dr^2} + \frac{C_1}{K_{Tt}r}\frac{dT}{dr} - \frac{C_2}{K_{Tt}r^2}T = -\frac{C_3}{K_{Tt}r^2}. \quad\text{..} \text{(A.19)}$$

Therefore the particular solution is given by

$$b = -r^{n_1}\int \frac{\left(-\frac{C_3}{K_{Tt}r^2}\right)\cdot r^{n_2}}{\mathcal{W}(r)}dr + r^{n_2}\int \frac{\left(-\frac{C_3}{K_{Tt}r^2}\right)\cdot r^{n_1}}{\mathcal{W}(r)}dr$$

$$= -\frac{C_3}{K_{Tt}n_1(n_2-n_1)} + \frac{C_3}{K_{Tt}n_1(n_2-n_1)} = -\frac{C_3}{n_1 n_2 K_{Tt}} = \frac{C_3}{C_2}. \quad\text{.............................} \text{(A.20)}$$

Finally, the general solution is given by

$$T(r) = c_1 r^{n_1} + c_2 r^{n_2} + b, \quad\text{...} \text{(A.21)}$$

where

$$b = \frac{\sum_{j=1}^{N_p} \frac{k_{rj}}{\mu_j}}{\sum_{j=1}^{N_p} \frac{k_{rj}}{\mu_j}\beta_j}. \quad\text{...} \text{(A.22)}$$

According to the boundary conditions, we can compute the arbitrary constants of the general solution. Using Eq. (A.2), we can get

$$c_1 r_{eff}^{n_1} + c_1 r_{eff}^{n_2} = T_{grid} - b. \quad\text{..} \text{(A.23)}$$

And, using Eq. A.3, we can get

$$K_{Tt}(c_1 n_1 r_w^{n_1-1} + c_2 n_2 r_w^{n_2-1}) = U_T(c_1 r_w^{n_1} + c_1 r_w^{n_2} + b - T_w). \quad\text{.....} \text{(A.24)}$$

Eq. (A.24) is rearranged into

$$c_1\left(\frac{K_{Tt}}{U_T}\frac{n_1}{r_w} - 1\right)r_w^{n_1} + c_2\left(\frac{K_{Tt}}{U_T}\frac{n_2}{r_w} - 1\right)r_w^{n_2} = b - T_w. \quad\text{..........................} \text{(A.25)}$$

Then we have to solve the system

$$\begin{bmatrix} r_{eff}^{n_1} & r_{eff}^{n_2} \\ \left(\frac{K_{Tt}}{U_T}\frac{n_1}{r_w} - 1\right)r_w^{n_1} & \left(\frac{K_{Tt}}{U_T}\frac{n_2}{r_w} - 1\right)r_w^{n_2} \end{bmatrix}\begin{bmatrix} c_1 \\ c_2 \end{bmatrix} = \begin{bmatrix} T_{grid} - b \\ b - T_w \end{bmatrix}. \quad\text{.................} \text{(A.26)}$$

Finally, we can get the arbitrary constants as follows:

$$c_1 = \frac{\left(\frac{n_2}{r_w} - \frac{U_T}{K_{Tt}}\right)r_w^{n_2}(T_{grid}-b) - \frac{U_T}{K_{Tt}}r_{eff}^{n_2}(b-T_w)}{r_{eff}^{n_1}\left(\frac{n_2}{r_w} - \frac{U_T}{K_{Tt}}\right)r_w^{n_2} - r_{eff}^{n_2}\left(\frac{n_1}{r_w} - \frac{U_T}{K_{Tt}}\right)r_w^{n_1}}, \quad\text{.......................................} \text{(A.27)}$$

and

$$c_2 = \frac{\left(\frac{n_1}{r_w} - \frac{U_T}{K_{Tt}}\right)r_w^{n_1}(b-T_{grid}) + \frac{U_T}{K_{Tt}}r_{eff}^{n_1}(b-T_w)}{r_{eff}^{n_1}\left(\frac{n_2}{r_w} - \frac{U_T}{K_{Tt}}\right)r_w^{n_2} - r_{eff}^{n_2}\left(\frac{n_1}{r_w} - \frac{U_T}{K_{Tt}}\right)r_w^{n_1}}. \quad\text{.......................................} \text{(A.27)}$$

Pipe with no open area

For the pipe with no open area, it is assumed that the pressure change in the reservoir grid which contains the wellbore is negligible, and it means the velocity is zero also. Under this condition, the second order ordinary differential equation becomes

$$\frac{1}{r}\frac{d}{dr}\left(r\frac{dT}{dr}\right) = 0,$$ .... (A.28)

and the associated boundary conditions are same with Eq. A.2 and A.3. Solve this equation and we can get the following general solution:

$$T(r) = d_1 \ln r + d_2,$$ .... (A.29)

where d_1 and d_2 are arbitrary constants. Using the boundary conditions, we can compute these constants. Using Eq. A.2, we can get

$$d_1 \ln r_{eff} + d_2 = T_{grid}.$$ .... (A.30)

And, also using Eq. A.3, we can get

$$\left(\ln r_w - \frac{K_{Tt}}{U_T}\frac{1}{r_w}\right)d_1 + d_2 = T_w.$$ .... (A.31)

Then, we have to solve the system

$$\begin{bmatrix} \ln r_{eff} & 1 \\ \ln r_w - \frac{K_{Tt}}{U_T}\frac{1}{r_w} & 1 \end{bmatrix}\begin{bmatrix} c_1 \\ c_2 \end{bmatrix} = \begin{bmatrix} T_{grid} \\ T_w \end{bmatrix}.$$ .... (A.32)

Finally, arbitrary constants are given as

$$d_1 = \frac{T_{grid}-T_w}{\ln\frac{r_{eff}}{r_w}+\frac{K_{Tt}}{U_T}\frac{1}{r_w}},$$ .... (A.33)

and

$$d_2 = \frac{T_{grid}\left(\frac{K_{Tt}}{U_T}\frac{1}{r_w}-\ln r_w\right)+T_w \ln r_{eff}}{\ln\frac{r_{eff}}{r_w}+\frac{K_{Tt}}{U_T}\frac{1}{r_w}}.$$ .... (A.34)

Hence, the reservoir temperature just outside the casing is computed as

$$T_I = T|_{r=r_w} = T_{grid} - \frac{(T_{grid}-T_w)\ln\frac{r_{eff}}{r_w}}{\ln\frac{r_{eff}}{r_w}+\frac{K_{Tt}}{U_T}\frac{1}{r_w}}.$$ .... (A.35)

DISCRETIZATION OF THE WELLBORE TEMPERATURE MODEL

In this section, a discretization of the wellbore temperature model is presented. The wellbore temperature model is given by

$$\frac{dT}{dx} = \frac{(\rho v c_p K_{JT})_T}{(\rho v c_p)_T}\frac{dp}{dx} + \frac{2}{R}\frac{\gamma(\rho v c_p)_{T,I}+(1-\gamma)U_T}{(\rho v c_p)_T}(T_I - T) - \frac{(\rho v)_T}{(\rho v c_p)_T}g(\sin\theta). \quad ..(B.1)$$

Recall that the equation is formulated under the assumption that the kinetic energy term and the shear stress term are negligible and the enthalpy difference is determined by the constant heat capacity and the temperature difference.

Fig. B.1 shows a 1D grid system for the discretization of the wellbore model. Then, we take the forward difference on Eq. B.1 and we can get the following equation:

$$\frac{T_{i+1}-T_i}{\Delta x_i} = \frac{(\rho v c_p K_{JT})_{T,i}}{(\rho v c_p)_{T,i}}\frac{p_{i+1}-p_i}{\Delta x_i} + \frac{2}{R_{i+1}}\frac{\gamma_{i+1}(\rho v c_p)_{T,I,i+1}+(1-\gamma_{i+1})U_{T,i+1}}{(\rho v c_p)_{T,i+1}}\left(T_{I,i+1} - T_{w,i+1}\right)$$

$$-\frac{(\rho v)_{T,i+1}}{(\rho v c_p)_{T,i+1}}g(\sin\theta_{i+1}). \quad .....(B.2)$$

And this is rearranged into

$$T_{i+1} = \left[1 + \frac{2}{R_{i+1}}\frac{\gamma_{i+1}(\rho v c_p)_{T,I,i+1}+(1-\gamma_{i+1})U_{T,i+1}}{(\rho v c_p)_{T,i+1}}\right]^{-1} \times \left[T_i + \frac{(\rho v c_p K_{JT})_{T,i}}{(\rho v c_p)_{T,i}}(p_{i+1} - p_i) + \right.$$

$$\left. \frac{2}{R_{i+1}}\frac{\gamma_{i+1}(\rho v c_p)_{T,I,i+1}+(1-\gamma_{i+1})U_{T,i+1}}{(\rho v c_p)_{T,i+1}}T_{I,i+1}\Delta x_i - \frac{(\rho v)_{T,i+1}}{(\rho v c_p)_{T,i+1}}g\sin\theta_{i+1}\Delta x_i\right]$$

$$..(B.3)$$

Since the wellbore pressure distribution is already solved by the wellbore pressure equation and the wellbore inflow temperature is computed by analytical solution, the boundary condition is only needed to solve this. For the steady state condition, since the effect of the accumulation term is ignored, the wellbore temperature at the toe is assumed to be same with the inflow temperature at the reservoir grid which contains the wellbore grid.
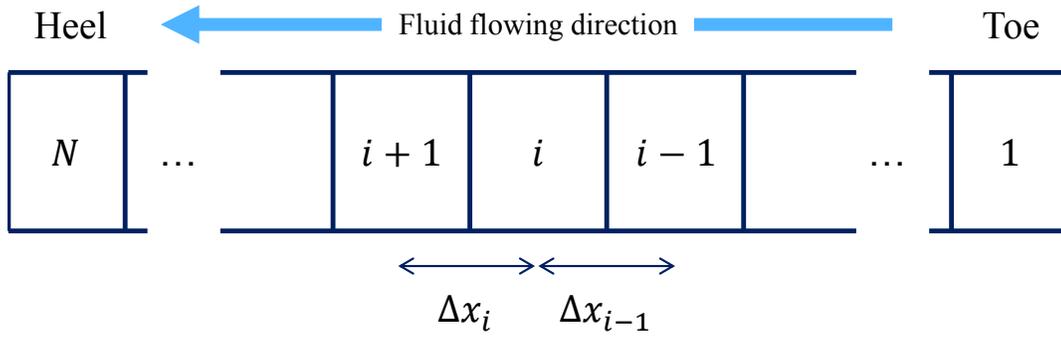
Fig. B.1 Grid system for discretization of the wellbore model

APPENDIX C

NON-ISOTHERMAL FLUID PROPERTY CORRELATIONS

In this section, we provide the correlations for the estimation of fluid properties used in this work. These are taken after the work by Dawkrajai (2006).

C.1 GAS PROPERTIES

Natural gas properties are estimated using the specific gravity of gas, γ_g, pressure and temperature.

C.1.1 GAS COMPRESSIBILITY FACTOR

Pseudo-critical pressure and temperature of natural gas using Sutton's equations (Sutton, 1985)

$$p_{pc} = 756.8 - 131.0\gamma_g - 3.6\gamma_g{}^2, \quad \text{...(C.1)}$$

$$T_{pc} = 169.2 + 349.5\gamma_g - 74.0\gamma_g{}^2, \quad \text{...(C.2)}$$

where γ_g is specific gravity of gas, and the units of p_{pc} and T_{pc} are psia and °R, respectively. Using these pseudo-critical pressure and temperature, pseudo-reduced pressure and temperature is given by (McCain, 1990)

$$p_{pr} = \frac{p}{p_{pc}}, \quad \text{...(C.3)}$$

$$T_{pr} = \frac{T}{T_{pc}}, \quad \text{...(C.4)}$$

where the units of pressure and temperature are psia and °R, respectively. Then, gas compressibility factor is computed by the work done by Dranchuk and Kassem (1975)

$$z = 1 + \left(A_1 + \frac{A_2}{T_{pr}} + \frac{A_3}{T_{pr}{}^3} + \frac{A_4}{T_{pr}{}^4} + \frac{A_5}{T_{pr}{}^5}\right)\rho_{pr} + \left(A_6 + \frac{A_7}{T_{pr}} + \frac{A_8}{T_{pr}{}^2}\right)\rho_{pr}{}^2$$

$$- A_9\left(\frac{A_7}{T_{pr}} + \frac{A_8}{T_{pr}{}^2}\right)\rho_{pr}{}^5 + A_{10}\left(1 + A_{11}\rho_{pr}{}^2\right)\left(\frac{\rho_{pr}{}^2}{T_{pr}{}^3}\right)\exp\left(-A_{11}\rho_{pr}{}^2\right),$$

$$\text{...(C.5)}$$

where

$$\rho_{pr} = 0.27 \left[\frac{p_{pr}}{zT_{pr}} \right], \quad \text{...} \quad \text{(C.6)}$$

and the constants are $A_1 = 0.3265$, $A_2 = -1.0700$, $A_3 = -0.5339$, $A_4 = 0.05169$, $A_5 = -0.05165$, $A_6 = 0.5475$, $A_7 = -0.7361$, $A_8 = 0.1844$, $A_9 = 0.1056$, $A_{10} = 0.6134$, and $A_{11} = 0.7210$. This correlation is applicable under the following conditions,

$$0.2 \leq p_{pr} < 30 \qquad \text{for } 1.0 < T_{pr} \leq 3.0, \quad \text{......................................} \quad \text{(C.7)}$$

$$p_{pr} < 1.0 \qquad \text{for } 0.7 < T_{pr} < 1.0. \quad \text{......................................} \quad \text{(C.8)}$$

C.1.2 DENSITY OF GAS

Gas density is computed by equation of state as (McCain, 1990)

$$\rho = \frac{Mp}{zRT}, \quad \text{...} \quad \text{(C.9)}$$

where

$$M = 28.97\gamma_g, \quad \text{...} \quad \text{(C.10)}$$

$$R = 10.732 \left[\frac{\text{psia·ft}^3}{\text{lbmol·°R}} \right], \quad \text{...} \quad \text{(C.11)}$$

and the unit of gas density, pressure and temperature is $\frac{\text{lb}}{\text{ft}^3}$, psia and °R, respectively.

C.1.3 VISCOSITY OF GAS

Gonzalez et al. (1970) presented a correlation of the gas viscosity as follows:

$$\mu_g = A(10^{-4}) \exp(B\rho^C), \quad \text{...} \quad \text{(C.12)}$$

where

$$A = \frac{(9.379 + 0.01607M)T^{1.5}}{209.2 + 19.26M + T}, \quad \text{...} \quad \text{(C.13)}$$

$$B = 3.448 + \frac{986.4}{T} + 0.01009M_a, \quad \text{...} \quad \text{(C.14)}$$

$$C = 2.447 - 0.2224B, \quad \text{...} \quad \text{(C.15)}$$

the unit of gas viscosity is in centipoises, and M is given by Eq. (C.10).

C.1.4 HEAT CAPACITY OF GAS

Perry et al. (1984) presented the following equation of the heat capacity for methane:

$$C_p = a + bT + \frac{c'}{T^2},$$ .... (C.16)

where the units of heat capacity and temperature are $\frac{kJ}{kg \cdot K}$ and K, respectively. And the coefficients are $a = 1.39$, $b = 0.003001$, and $c' = 0$.

C.1.5   THERMAL EXPANSION COEFFICIENT OF GAS

According to definition of the isobaric thermal coefficient of volume expansion for gas is given by

$$\beta = -\frac{1}{\rho}\left(\frac{\partial \rho}{\partial T}\right)_p,$$ .... (C.17)

or

$$\beta = \frac{1}{T} + \frac{1}{z}\left(\frac{\partial z}{\partial T}\right)_p,$$ .... (C.18)

where the units of β and temperature are $\frac{1}{°R}$ and °R.

C.1.6   TOTAL THERMAL CONDUCTIVITY OF GAS IN RESERVOIR

The thermal conductivity of sandstone saturated with gas at reservoir temperature are from Anand et al. (1973) In the ranges of temperature between 150 °F and 250 °F, the value of $K_{Tt,g}$ is almost constant.

$$K_{Tt,g} = 1.3 \left[\frac{Btu}{lb \cdot ft \cdot °F}\right],$$ .... (C.19)

C.2   OIL PROPERTIES

Crude oil properties are calculated using the gas specific gravity, °API and solution gas ratio R_s with temperature and pressure.

C.2.1   BUBBLE POINT PRESSIRE OF OIL

Standing (1977) presented the following equations to estimate bubble point pressure of oil:

$$p_b = 18.2\big[(CN)_{pb} - 1.4\big], \quad \text{... (C.20)}$$

where

$$(CN)_{pb} = \left(\frac{R_s}{\gamma_g}\right)^{0.83} 10^{(0.00091T - 0.0125°API)}, \quad \text{.. (C.21)}$$

T is the reservoir temperature in °F, R_s is solution gas-oil ratio in $\frac{scf}{STB}$, and p_b is bubble point pressure in psia.

C.2.2 DENSITY OF OIL

The density of the crude oil at reservoir condition are given by

$$\rho = \rho_{po} + \Delta\rho_p - \Delta\rho_T, \quad \text{.. (C.22)}$$

where

$$\Delta\rho_p = \left(0.167 + 16.181(10^{-0.0425v_{po}})\right)\left(\frac{p}{1000}\right)$$

$$-0.01\left(0.299 + 262(10^{-0.0603\rho_{po}})\right)\left(\frac{p}{1000}\right)^2, \quad \text{.............. (C.23)}$$

$$\Delta\rho_T = (0.00302 + 1.505\rho_{bs}^{-0.951})(T - 60)^{0.938}$$

$$-\left(0.0216 - 0.0233(10^{-0.0161\rho_{bs}})\right)(T - 60)^{0.475}, \quad \text{..... (C.24)}$$

p is pressure in psia, ρ_{po} is the pseudo-liquid density, and $\Delta\rho_p$ is the adjustment for pressure in $\frac{lb}{ft^3}$, T is temperature in °F, ρ_{bs} is the liquid density at surface pressure and 60 °F, $\Delta\rho_T$ is the adjustment for temperature in $\frac{lb}{ft^3}$. ρ_{po} is given by

$$\rho_{po} = \frac{\frac{R_s M}{380.7} + 350.207\gamma_o}{5.615 + \frac{R_s M}{380.7\rho_a}}, \quad \text{.. (C.25)}$$

$$\gamma_o = \frac{141.5}{131.5 + °API}, \quad \text{.. (C.26)}$$

$$\rho_a = 38.52(10^{-0.00326API}) + (94.75 - 33.93\log API)\log\gamma_g, \quad \text{........... (C.27)}$$

where API is the gravity of oil and ρ_a is the apparent liquid density of the gas in $\frac{lb}{ft^3}$ at 60 °F and surface pressure.

C.2.3   VISCOSITY OF OIL

Beggs and Robinson (1975) presented the equations for oil viscosities. At first the dead oil viscosity is given by

$$\mu_{oD} = 10^C - 1, \quad\text{..(C.28)}$$

where

$$C = (10^{3.0324 - 0.02023 API})(T^{-1.163}) \quad\text{.....................................(C.29)}$$

and T is temperature in °F. Then, the viscosity of live oil is computed by

$$\mu_{oR} = A\mu_{oD}{}^B, \quad\text{..(C.30)}$$

where

$$A = 10.715(R_s + 100)^{-0.515}, \quad\text{..(C.31)}$$

$$B = 5.44(R_s + 150)^{-0.338}, \quad\text{...(C.32)}$$

and R_s is dissolved GOR in $\frac{scf}{STB}$.

C.2.4   HEAT CAPACITY OF OIL

Gambill (1957) developed a relation for heat capacity of oil at reservoir temperature for t is less than about 300 °F by

$$C_p = \frac{0.388 + 0.00045T}{\sqrt{\gamma_o}}. \quad\text{..(C.33)}$$

where C_p is the heat capacity of oil in $\frac{Btu}{lb°F}$, T is reservoir temperature in °F and γ_o is given by Eq. C.26.

C.2.5   THERMAL EXPANSION COEFFICIENT OF OIL

The isobaric thermal expansion of undersaturated oil is defined as

$$\beta = -\frac{1}{\rho}\left(\frac{\partial\rho}{\partial T}\right)_p = \frac{1}{B_o}\left(\frac{\partial B_o}{\partial T}\right)_p, \quad\text{..(C.34)}$$

where β is the thermal expansion coefficient in $\frac{1}{°R}$, B_o is the oil formation volume factor, and ρ is oil density. Because the density of an undersaturated liquid decreases as the temperature increase, β is positive.

C.2.6 TOTAL THERMAL CONDUCTIVITY OF OIL IN RESERVOIR

The thermal conductivity of sandstone saturated with oil at reservoir temperature is given by Anand et al. (1973). In the ranges of temperature between 150 °F and 250 °F, the value of $K_{Tl,o}$ is almost constant.

$$K_{Tl,o} = 2.0 \frac{Btu}{lb \cdot ft \cdot °F}. \quad \text{...} \text{(C.35)}$$

C.3 WATER PROPERTIES

Water properties are calculated by assuming that pressure, temperature and salinity are known.

C.3.1 DENSITY OF WATER

The density of water at reservoir condition is estimated using correlation presented by McCain (1990). At first, the water density at standard condition is calculated by

$$\rho_{w,STD} = 62.368 + 0.438603S + 1.60074S^2 \times 10^{-3}. \quad \text{........................} \text{(C.36)}$$

where S is the salinity in weight percent solids, $\rho_{w,STD}$ is the water density at standard condition in $\frac{lb}{ft^3}$. Then, the water formation volume factor is computed as

$$B_w = (1 + \Delta V_{wp})(1 + \Delta V_{wT}), \quad \text{...} \text{(C.37)}$$

where

$$\Delta V_{wT} = -1.0001 \times 10^{-2} + 1.33391T \times 10^{-4} + 5.50654T^2 \times 10^{-7},$$
$$\text{...} \text{(C.38)}$$

$$\Delta V_{wp} = -1.95301 \times 10^{-9} - 1.72834p^2T \times 10^{-13}$$
$$-3.58922p \times 10^{-7} - 2.25341p^2 10^{-10}, \quad \text{............} \text{(C.39)}$$

where T is in °F, p is in psia and B_w is in $\frac{res\ bbl}{STB}$. Finally, water density at reservoir condition is computed by

$$\rho_w = \frac{\rho_{w,STD}}{B_w}, \quad \text{...} \text{(C.40)}$$

where ρ_w is water density in $\frac{lb}{ft^3}$.

C.3.2 VISCOSITY OF WATER

Water viscosity correlation was developed from data that have a temperature range of 86.5 to 167 °F and pressure up to 14,000 psi (Collins, 1987). At first water viscosity at atmospheric pressure by

$$\mu_{w,STD} = AT^B, \quad \text{...(C.41)}$$

where

$$A = A_0 + A_1 S + A_2 S^2 + A_3 S^3, \quad \text{...(C.42)}$$

$$B = B_o + B_1 S + B_2 S^2 + B_3 S^3 + B_4 S^4, \quad \text{..............................(C.43)}$$

where $A_0 = 109.574$, $A_1 = -8.40564$, $A_2 = 0.313314$, $A_3 = 8.72213 \times 10^{-3}$, $B_0 = -1.12166$, $B_1 = 2.63951 \times 10^{-2}$, $B_2 = -6.79461 \times 10^{-4}$, $B_3 = -5.47119 \times 10^{-5}$, $B_4 = 1.55586 \times 10^{-6}$ and S is salinity in weight percent solids. And then the viscosity at reservoir condition is computed as

$$\mu_w = \mu_{w,STD}(0.9994 + 4.0295p \times 10^{-5} + 3.1062p^2 \times 10^{-9}). \quad \text{..........(C.44)}$$

C.3.3 HEAT CAPACITY OF WATER

The heat capacity of liquid water at saturation condition is represented by the following equation (Cassis et al., 1985)

$$C_p = 4.182 - 1.5T \times 10^{-4} + 3.44T^2 \times 10^{-7} + 4.26T^3 \times 10^8, \quad \text{..........(C.45)}$$

where C_p is in $\frac{kJ}{kg \cdot °C}$ and T is in °C.

C.3.4 THERMAL EXPANSION COEFFICIENT OF WATER

The isobaric thermal expansion of water is defined as

$$\beta = -\frac{1}{\rho_w}\left(\frac{\partial \rho_w}{\partial T}\right)_p = \frac{1}{B_w}\left(\frac{\partial B_w}{\partial T}\right)_p, \quad \text{..(C.46)}$$

where β is the thermal expansion coefficient in $\frac{1}{°R}$, B_w is the water formation volume factor, and ρ_w is water density. Because the density of water decreases as the temperature increase, β is positive.

C.3.5 TOTAL THERMAL CONDUCTIVITY OF WATER IN RESERVOIR

The thermal conductivity of sandstone saturated with water at reservoir temperature is given by Anand et al. (1973). In the ranges of temperature between 150 °F and 250 °F, the value of $K_{Tl,w}$ is almost constant.

$$K_{Tl,w} = 2.5 \frac{Btu}{lb \cdot ft \cdot {}^\circ F}. \quad \text{...(C.47)}$$

APPENDIX D

APPROXIMATION OF PARAMETER VALUES OF NETWORK FRACTURE

REGION

In this section, a simple approximation method of parameter values of network fracture region is presented. When the single porosity approach is taken for the expression of the network fracture region, the discrete fracture network model is used. In the discrete fracture network models, usually, the network fractures are expressed as thin high permeable grids (Cipolla et al., 2010a), and when the microseismic data is integrated, the network structure can be expressed as thin crossing lines using the fine girds (Mayerhofer et al., 2006; Xie et al., 2012). Because the discrete fracture network models rigorously express the transient behavior but it requires a lot of computational time, dual porosity model or an appropriate model in multiple-porosity models is used in order to reduce the computational efforts keeping the accuracy to a certain extent. However, these models require consideration of additional parameters such as matrix-fracture shape facture. In this work, in order to reduce the computational efforts for simulation and reduce the number of parameters to be considered, we take the approach of enhanced permeability area used by Yin et al. (2011) in which the enhancement effect by the network fracture is considered as the change of parameter values in the vicinity of planar primary fractures. The network fractures are expressed as higher permeable matrix region comparing to the unstimulated matrix region. The permeability of the network fracture region is approximated by harmonic-arithmetic upscaling, and the porosity is estimated by considering volumetric ratio of void space in the region.

Fig. D.1 shows geometry of the system with multiple transverse fractures (primary fractures) and associated network fractures (secondary fractures), and one part of the stimulated reservoir volume is selected on the right side of the figure. In this figure, the number of secondary fractures is assumed to be two. The secondary fractures and the matrix zone are to be approximated as enhanced permeability zone (Fig. D.2). Because

123

the primary fracture is expressed as thin grid cells, only the secondary fractures and matrix zone are the considered for the calculation of the parameters in network fracture region. **Fig. D.3** shows the region to be expressed as enhanced permeability zone for this case where k_M is matrix permeability and $w_{f,n}$ is the total fracture network width given under the assumption that the secondary fractures have the same fracture width $w_{f,s}$ by

$$w_{f,n} = n_{f,s} \times w_{f,s}, \quad\text{...(D.1)}$$

where $n_{f,s}$ is the number of secondary fractures in the region. $L_{EPA,x}$, $L_{EPA,y}$ and $L_{EPA,z}$ are the lengths of the region in x-, y- and z-direction, respectively, which are given by

$$L_{EPA,x} = L_{spacng} - w_{f,p}, \quad\text{...(D.2)}$$

$$L_{EPA,y} = x_f, \quad\text{...(D.3)}$$

and

$$L_{EPA,z} = h_f \quad\text{...(D.4)}$$

where $w_{f,p}$ is the width of primary fracture. Here we assume that the secondary fractures exist in each direction and these fractures have the same values of $w_{f,s}$ and $k_{f,s}$.

When we consider the x-y plane, the permeability can be estimated by harmonic average of matrix permeability and secondary fractures permeability in the x-direction and arithmetic average of the harmonic averaged x-direction permeability and secondary fractures permeability in y-direction. The harmonic average permeability is calculated by

$$k_{harm,x} = \frac{L_{EPA,x}}{\frac{w_{f,n}}{k_{f,s}} + \frac{L_{EPA,x} - w_{f,n}}{k_M}} = \frac{L_{EPA,x}}{\frac{n_{f,s}w_{f,s}}{k_{f,s}} + \frac{L_{EPA,x} - w_{f,n}}{k_M}}, \quad\text{...................................(D.5)}$$

and the arithmetic average permeability is calculated by

$$k_{EPA,x} = \frac{w_{f,n}k_f + (L_{EPA,x} - w_{f,n})k_{harm,x}}{L_{EPA,x}}$$

$$= \frac{n_{f,s}w_{f,s}k_f + (L_{EPA,x} - n_{f,s}w_{f,s})k_{harm,x}}{L_{EPA,x}}, \quad\text{...(D.6)}$$

where $k_{EPA,x}$ is the permeability of the enhanced permeability zone in the x-direction. In the similar manner, $k_{EPA,y}$ and $k_{EPA,z}$ can be calculated.
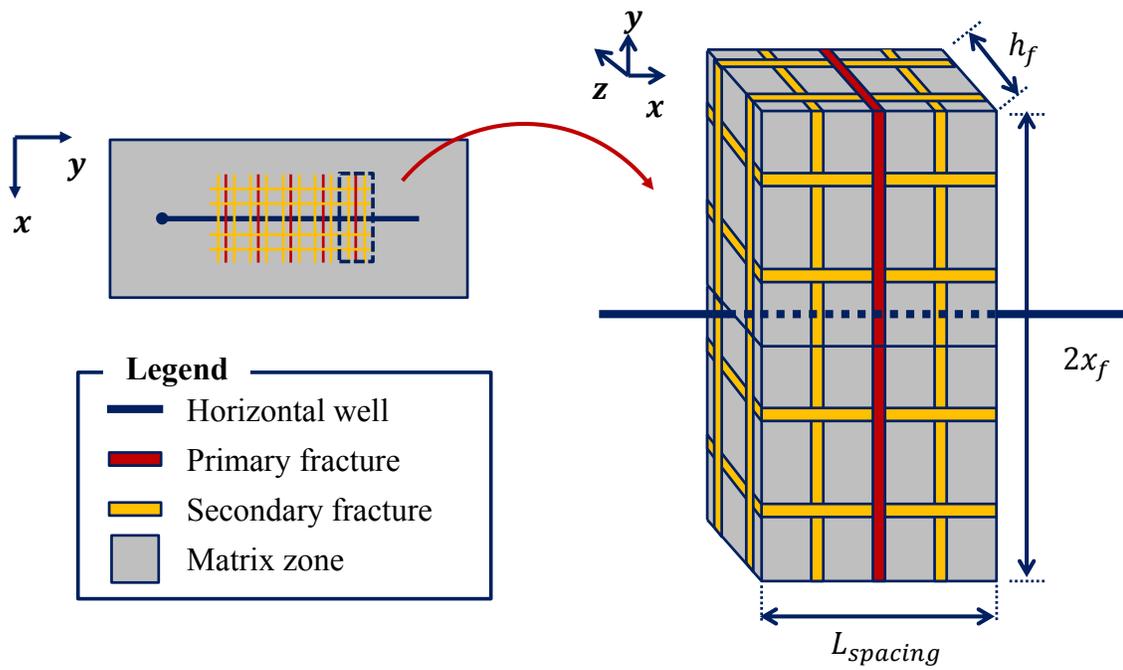
Fig. D.1 Geometry of the system with multiple transverse fractures and one part of the stimulated reservoir volume
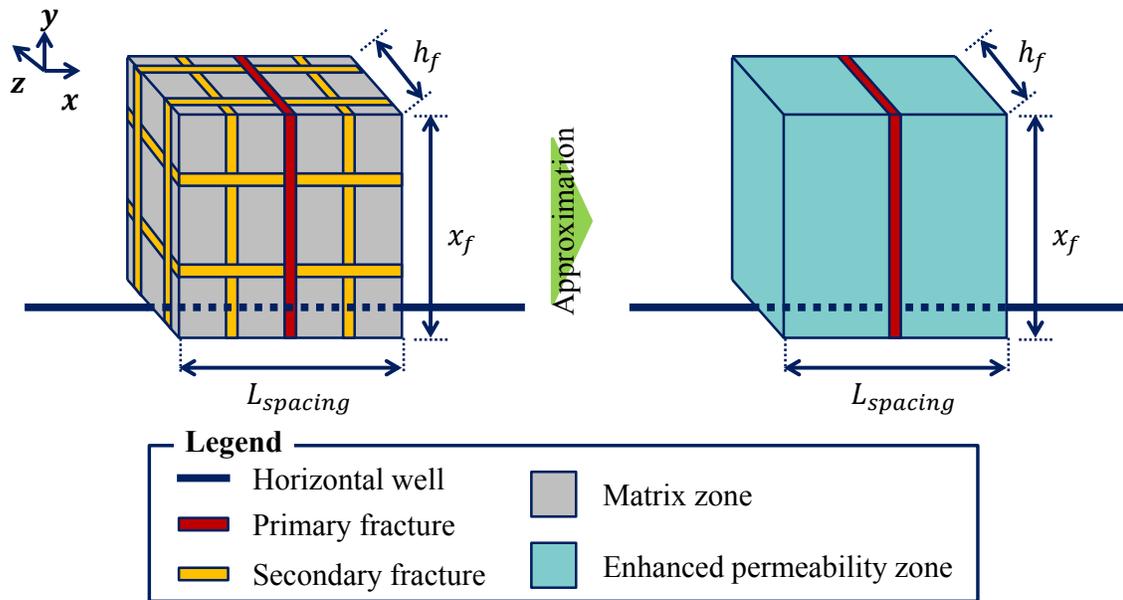

Fig. D.2 Approximation of the matrix zone as enhanced permeability zone
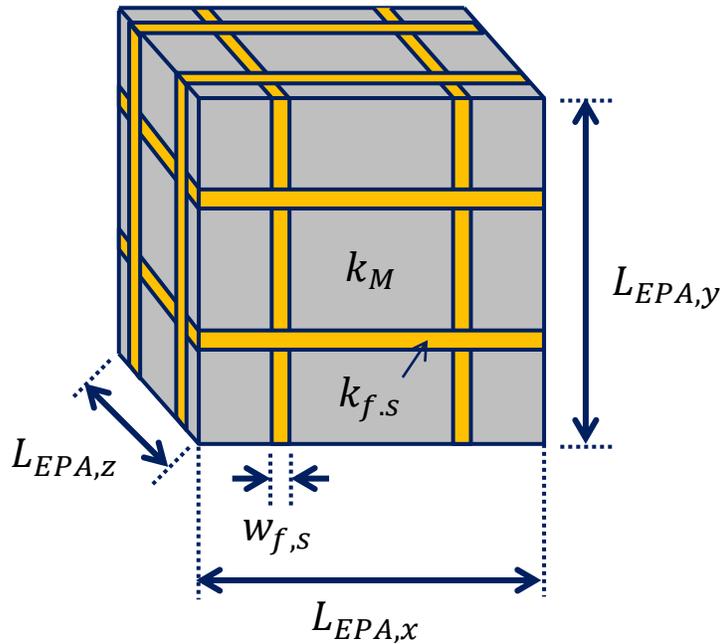
Fig. D.3 Network fracture region to be expressed as enhanced permeability zone

The porosity of the region (ϕ_{EPA}) is approximated by considering the volumetric ratio of the void space in the region, and it is approximated by

$$\phi_{EPA} = \frac{V_{F,n}\phi_{F,n}+V_M\phi_M}{V_{EPA,bulk}}, \quad \dots\dots\dots\dots\dots\dots\dots\dots\dots\dots\dots\dots\dots\dots\dots\dots\dots\text{(D.7)}$$

where $V_{F,n}$ is the volume of secondary fracture network, $\phi_{F,n}$ is the average of the porosity in the secondary fractures which is the same with the porosity in the secondary fracture $\phi_{F,s}$ under the assumption of the identical secondary fractures, V_M is the matrix volume, ϕ_M is the matrix porosity and $V_{EPA,bulk}$ is the bulk volume of the target region. The porosity of the secondary fracture is calculated by the proppant packing fraction in fracture:

$$\phi_{F,s} = 1 - \text{proppant packing fraction in fracture.} \quad \dots\dots\dots\dots\dots\dots\dots\text{(D.8)}$$

Example calculation

In this part, we present an example approximation of enhanced permeability and porosity. The parameters to be used are summarized in **Table D-1**, and we assume several parameters about secondary fractures presented in **Table D-2**. The schematic of the example geometry is presented in **Fig. D.4**.

TABLE D-1 PARAMETERS FOR EXAMPLE CALCULATION

Parameter	Description	Base Case1
k_M	Matrix Permeability, md	1.50E-04
k_f	Fracture Permeability, md	400
ϕ_M	Matrix Porosity, -	8.00%
ϕ_F	Fracture Porosity (given by PPF)	26.00%
x_f	Propped Fracture half length, ft	150
h_f	Propped Fracture Height, ft	180
$L_{spacing}$	Fracture spacing, ft	300
PPF	Proppant Packing Fraction of fracture	74.00%

TABLE D-2 ASSUMPTIONS ON SECONDARY FRACTURES

Parameter	Description	Value [unit]
$n_{f,s}$	Number of secondary fractures	3 [-]
$w_{f,s}$	Secondary fracture width	0.1 [ft]
$k_{f,s}$	Secondary fracture permeability	40 [md]

In the x-direction, harmonic average of the matrix permeability and secondary permeability is computed as

$$k_{harm,x} = \frac{300\text{ft}}{(3)\left(\frac{0.1\text{ft}}{40\text{md}}\right)+\frac{300\text{ft}-0.1\text{ft}}{150\times10^{-6}\text{md}}} = 150.15 \times 10^{-6} \text{ [md].} \quad \text{......................(D.9)}$$

And, then, the arithmetic average of permeability in the x-direction is calculated as

$$k_{EPA,x} = \frac{(3)(0.1\text{ft})(40\text{md})+(300\text{ft}-0.1\text{ft})\left(150.15\times10^{-6}\text{md}\right)}{300\text{ft}}$$

$$= 0.04015 \text{ [md].} \quad \text{..(D.10)}$$

Similarly, the permeability in the y-direction and x-direction are computed as

$$k_{EPA,y} = 0.08015 \text{ [md]}, \quad \text{..}(D.11)$$

and

$$k_{EPA,z} = 0.066816 \text{ [md]}. \quad \text{..}(D.12)$$

For the porosity estimation, the bulk volume of the network fracture region is estimated by

$$V_{EPA,bulk} = (300\text{ft})(150\text{ft})(180\text{ft}) = 8.100 \times 10^6 \text{ [ft}^3\text{].} \quad \text{...................}(D.13)$$

Then, the volume of matrix and network fractures are calculated as

$$V_M = (299.7\text{ft})(149.7\text{ft})(179.7\text{ft}) = 8.062 \times 10^6 \text{ [ft}^3\text{],} \quad \text{....................}(D.14)$$

and

$$V_{F,n} = (0.3)(150)(180) + (300)(0.3)(180) + (300)(150)(0.3) - (0.3)(0.3)(0.3)$$
$$= 3.780 \times 10^4 \text{ [ft}^3\text{].} \quad \text{..}(D.15)$$

Therefore, the porosity of enhanced permeability zone is approximated as

$$\phi_{EPA} = \frac{V_{F,n}\phi_{F,s} + V_M\phi_M}{V_{EPA,bulk}} = \frac{(3.780 \times 10^4)(0.26) + (8.062 \times 10^6)(0.08)}{8.100 \times 10^6}$$
$$= 0.0808 \text{ [}-\text{]} \quad \text{..}(D.16)$$
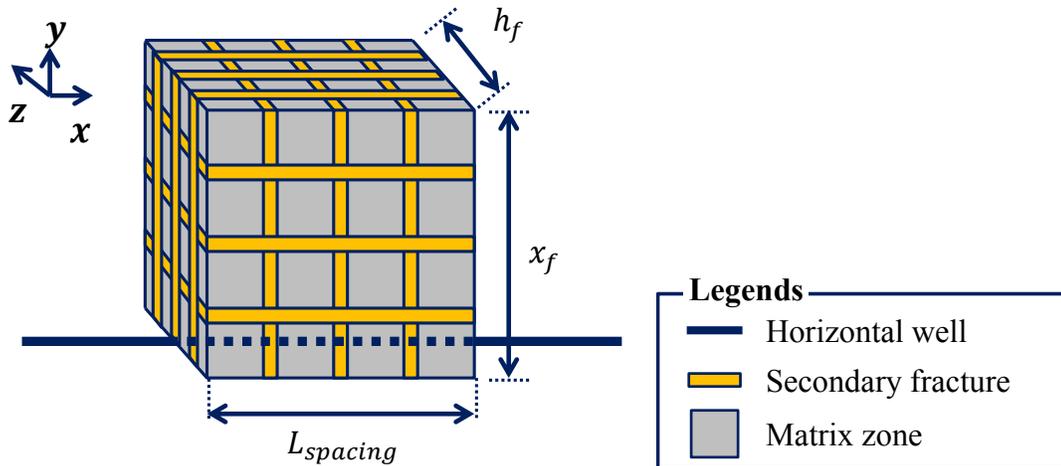

Fig. D.4 Geometry of a network geometry region for example calculation